# DIRECT WRITING FOR SILICON WAFER SOLAR CELLS

LICHENG LIU

NATIONAL UNIVERSITY OF SINGAPORE

2014

# DIRECT WRITING FOR SILICON WAFER SOLAR CELLS

**LICHENG LIU**

*B.Eng. (Hons.), NUS*

**A THESIS SUBMITTED**

**FOR THE DEGREE OF DOCTOR OF PHILOSOPHY**

**DEPARTMENT OF ELECTRICAL AND COMPUTER ENGINEERING**

**NATIONAL UNIVERSITY OF SINGAPORE**

**2014**

# Declaration

I hereby declare that the thesis is my original work and it has been written by me in its entirety. I have duly acknowledged all the sources of information which have been used in the thesis.

The thesis has also not been submitted for any degree in any university previously.

Name : Licheng LIU

Signature : 

Date : 1 Dec 2014

# Acknowledgements

First of all, I acknowledge that this PhD research was financially supported by Singapore's National Research Foundation (NRF), via a Clean Energy Programme Office PhD Scholarship provided by the Economic Development Board (EDB).

I would like to express my deepest gratitude to my main supervisor, Prof. Armin Gerhard ABERLE for providing me with this fantastic opportunity to work in the Solar Energy Research Institute of Singapore (SERIS). Not only has he given me the freedom required for this intellectual endeavour, Prof. Aberle has also been patient and encouraging in his guidance. His keenness to personally go through the textbooks and literatures with me when treading on unfamiliar academic territories has taught me that learning has no boundaries. I am also profoundly grateful to my co-supervisor, Dr Bram HOEX, for all academic discussions and his insightful contributions. In fact, his innovation and broad-based knowledge in solar cell characterization techniques have directly influenced some of the analysis presented in this work. Both my supervisors have been more than supportive of my work, and also of my one-year research stay at the School of Photovoltaic and Renewable Energy Engineering (SPREE) in the University of New South Wales (UNSW), Australia.

My heart-felt thanks go to Dr Alison LENNON, who was my supervisor in SPREE during the research stay. A considerable amount of work in this thesis was made possible through her expertise in chemistry and direct writing techniques. Also, I would like to extend my special appreciation to Dr Xi WANG for the long hours of scientific interactions in the planning stage and the collaborative efforts in the

experimental and characterization stages. His persistence in always digging deeper in order to get closer to the truth showed me the dedication required for things beyond research.

I am indebted to Dr Karl Erik BIRGERSSON for enlightening me about the importance of effective communication, which is a skill that I have benefitted considerably from and am still constantly honing even today. I also want to thank Sincheng for his words of encouragement at the beginning of my candidature, that had provided me with the motivation to constantly better myself.

I must also thank the great friends I have made throughout the candidature in both SERIS and SPREE. In particular, I would like to thank Dr Fen LIN, Jia CHEN, Zheren DU, Martin HEINRICH, Dr Hidayat, Ankit KHANNA, Jie CUI, Xi WANG, Dong LIN, Dr Yu YAO and Dr Zi OUYANG for all their contributions to this work, the intellectual exchanges and the unfathomable friendships.

Last but not least, I thank God for my family. To Mom and Dad: thank you so much for your unconditional love and the years of extremely hard work. Thank you for imparting to me the many virtues that have shaped me into a responsible individual. To Marilyn: thank you for having loved me. I dedicate this work to all of you and hope that I have done you proud.

# Table of contents

This page is intentionally left blank

# Abstract

This thesis investigates the application of drop-based direct writing techniques for the fabrication of advanced silicon wafer solar cells. In particular inkjet and aerosol jet printing are investigated for patterning the rear dielectric films of aluminium local back surface field (Al-LBSF) solar cells. A new method is presented to geometrically confine directly deposited features on hydrophilic rough surfaces. The direct patterning technique is applied to the fabrication of Al-LBSF solar cells, resulting in cell efficiencies of up to 18.5%. In addition, the etching of silicon in hydrofluoric acid (HF) is investigated in detail. HF etching is commonly used to remove masking layers in the Al-LBSF solar cell fabrication process, due to its excellent selectivity in etching dielectric films over silicon. This work shows that this selectivity does not necessarily hold for highly *n*-type doped silicon surfaces, which has major consequences for the solar cell fabrication process.

# List of tables

# List of figures

This page is intentionally left blank

# Chapter 1. Introduction

## §1.1 Motivation

In only 50 years since her independence in 1965, Singapore has rapidly transformed herself from a 'third-world' nation into a thriving, sky-scraping and vibrant global city, with one of the fastest growing economies and the highest percentage of millionaires in the world. Her phenomenal economic growth places her in the limelight as one of the world's leading commercial hubs. Singapore is one of the most densely populated countries (~7,000 persons/$km^2$) in the world, with a land area of approximately 710 $km^2$ and a population of more than 5 million people, and the greatest challenge she constantly faces is the lack of natural resources. One such key natural resource that is essential to the survival and the continuous growth of Singapore is energy. In order to power a "city that never sleeps", Singapore relies heavily on electricity generated from fossil fuels (with a share of 90% for natural gas in 2014) [1]. According to The World Factbook, Singapore is ranked number 52 worldwide in terms of country natural gas consumption and number 23 in terms of electricity consumption per capita [2]. For a small country like Singapore such high consumption is unsustainable, as fossil fuels will eventually be depleted. A study in 2013 estimated that the worldwide reserve-to-production ratio for natural gas, which forecasts its future availability, is about 64 years [3]. In addition, the relentless consumption of fossil fuels in many countries has also taken its toll on the environment and resulted in irrevocable damages such as pollution, global warming and changes in climate

extremes. Therefore, it is essential for Singapore to start investing in renewable energy.

A special report released by the Intergovernmental Panel on Climate Change (IPCC) in 2012 accessed the negative consequences of climate change and proposed several methods of mitigation and management strategies for policy makers, of which renewable energy was one key area of interest [4]. In fact, many renewable energy sources receive significant (even up to 100%) contributions from the Sun. For instance biomass is biological material that comes from the living beings, which almost exclusive rely on the Sun for their energy. The air current that drives wind turbines is formed from solar heated air and the resulting air pressure differences. Even hydropower is dependent on the rain that is supported by solar-evaporated water. Most renewable energy sources such as tidal, wind, geothermal and hydropower are also location limited. In other words, only a certain number of places in the world are geographically suitable to harness these energies, which does not include Singapore due to its equatorial location and relatively flat terrain. However, being situated next to the equator at the latitude of only ~1.4° north, Singapore is blessed with a plethora of sunlight throughout the entire year, with very small seasonal variations. Thus, directly harvesting solar energy and converting it into heat energy (solar thermal) or electrical energy (solar photovoltaic) is Singapore's best bet.

Today, solar photovoltaics (PV) is one of the most promising renewable energy technologies due to its potential prospects and reducing cost. The term "photovoltaics" originates from Greek, and it essentially means voltage creation from light. Many governments have embraced the solar PV technology by introducing feed-in tariffs (FIT), which is a policy mechanism designed to

accelerate investment in renewable energy technologies via creation of a market [5]. A recent press release by the European Photovoltaic Industry Association indicated that the global cumulative installed PV capacity had already reached 136.7 GW by the end of 2013 [6]. In the plenary talk for crystalline silicon solar cells at the 38$^{th}$ IEEE Photovoltaic Specialists Conference 2012, Eicke Weber of Fraunhofer ISE, Germany, projected a bright future for PV by predicting 30 TW of accumulated PV installations in 2050 that can provide 10% of the global annual electricity demand [7]. Considerable effort has also been made in the PV industry to bring down the cost of PV electricity. One important milestone in this regard is to achieve “grid parity” for PV, which means that the levelised cost of electricity (LCoE) generated from PV is equal to the price of electricity from the grid. A recent grid parity model was applied to more than 150 countries and a total of 305 market segments worldwide, and this study predicted that grid parity is in reach for about 75-90% of the total global electricity market by 2020 [8]. For large PV systems (> 100 kW), Singapore has already reached grid parity in 2012 [9]. Being one of the earlier countries in the region to have achieved this milestone, Singapore aims to become a leader in this technology and is investing a significant amount of resources into its research and development, which is also closely related to its cost reduction.

With increasing relevance of PV as a viable source of clean energy, material cost reduction has been identified as one of the key areas to bring down the overall cost of the technology. As a consequence, the wafer thickness for solar cell fabrication is constantly decreasing. This inevitably presents more challenges for the fabrication processes and creates more room for research and development in the relevant areas. Ultimately the conversion efficiency of the solar cells must

not be compromised at the cost of the material reduction. Today, the record conversion efficiency for large-area monocrystalline silicon solar cells is 25.6% for a back-contact Heterojunction with Intrinsic Thin layer (HIT) solar cell fabricated by Panasonic [10].

In order to further improve the conversion efficiency of solar cells in high volume production at a low cost, the current processing technologies are being pushed to their limits. The production of high-efficiency solar cells nowadays can involve a number of patterning processes, such as selective emitter formation, dielectric patterning, seed layer and full-height metallization, which can be achieved with patterning techniques such as screen printing and lithography. However, with reducing wafer thickness it becomes increasingly challenging to utilize screen printing for patterning because the pressure-based nature of screen printing results in a higher chance of wafer breakages, which leads to yield loss. On the other hand, lithography does not have the potential to be implemented cost-effectively in silicon wafer solar cell manufacturing, as it is a cumbersome and time-consuming process that entails multiple steps and consequently cannot be done at a sufficiently low cost. To tackle these issues, direct writing has been identified as a promising alternative to the current technologies. It is a non-contact patterning technique that can resolve the problem of increasing breakages with reducing wafer thickness faced by screen printing. In addition, depending on the experimental methodology adopted, direct writing is able to perform precise deposition of functional materials to create both positive and negative features. In other words, it is able to build 3D structures on the target surface, as well as remove existing materials from the surface. Moreover, the rapid digital prototyping feature allows the users to render new and innovative

patterns as and when desired. Therefore neither additional processing time nor steps are required to fabricate new screens or masks. Currently a wide range of applications for direct writing is available, which is discussed in detail in Chapter 2. Its applications in silicon wafer solar cells are investigated in detail in this PhD thesis.

## §1.2 Thesis outline

**Chapter 2** starts with an overview of the direct writing technology, where different direct writing techniques are briefly described. As inkjet and aerosol jet printing technologies are used to perform the work in this thesis, these techniques will be discussed in more detail. A comparison between the two technologies is also presented, followed by a list of current applications of the droplet based direct writing techniques in the PV industry. Direct patterning of rear dielectric films for aluminium local back surface field (Al-LBSF) solar cells is identified for investigation, which will be discussed in detail in the later chapters.

In the fabrication of Al-LBSF solar cells, the use of dielectric films as masking layers and its removal in hydrofluoric acid (HF) are necessary for some single-side processes. It is commonly accepted that HF has excellent selectivity in etching dielectric films over silicon. However, as shown in **Chapter 3** of this work, the selectivity does not apply to highly doped *n*-type silicon surfaces and can result in detrimental effects on the efficiency of the solar cells. We investigated this etching behaviour of highly doped *n*-type silicon in HF in detail. A proper understanding and exploitation of the etching mechanism are beneficial for the subsequent direct patterning process.

A practical problem encountered by the direct patterning of dielectric films in the fabrication of solar cells is the large spreading dimension of the directly deposited droplets, as the silicon surface is typically textured and the coated dielectric layers are usually highly hydrophilic. **Chapter 4** looks into this issue in detail, whereby a method to geometrically confine the directly deposited features is presented that results in high printing definition. A dielectric layer of 200 nm $SiN_x$

on a textured silicon wafer is selectively etched, resulting in a fine line width of ~15 µm.

**Chapter 5** discusses the application of the direct patterning techniques to the fabrication of Al-LBSF solar cells. The effects of varying the line width, the pitch distance and the firing profile on various solar cell parameters are discussed in detail. Al-LBSF solar cells with PV efficiencies of up to 18.5% are produced.

Finally, the most important results of this work are summarised in **Chapter 6**. An outlook of possible future work is also given in this chapter.

## §1.3 References Chapter 1

[1] "Smart energy sustainable future", Singapore: Energy Market Authority, 2013.

[2] "The world factbook 2013-14: Singapore", Washington DC: Central Intelligence Agency, 2013.

[3] "International energy outlook 2013", Washington DC: U.S. Energy Information Administration, 2013.

[4] IPCC, "*Special report on renewable energy sources and climate change mitigation"*. United Kingdom and New York, NY, USA: Cambridge University Press, 2011.

[5] T. Couture, K. Cory, C. Kreycik, and E. William, "A policymaker's guide to feed-in tariff policy design", U.S. Dept. of Energy and National Renewable Energy Laboratory, 2010.

[6] "*Record-year for photovoltaic markets in 2013, Asia taking over the leading role"*, European Photovoltaic Industry Association, 2014, Available: http://www.epia.org/fileadmin/user_upload/Press_Releases/MW_PR_2014.pdf

[7] E. Weber, "The future of crystalline silicon photovoltaic technology," in *Proc*. *38th IEEE Photovoltaic Specialists Conference (PVSC)*, pp. Austin, Texas, 2012.

[8] C. Breyer and A. Gerlach, "Global overview on grid-parity," *Progress in Photovoltaics: Research and Applications,* vol. 21, pp. 121, 2013.

[9] G. Chua, "Brighter days for solar panel sales", in *The Straits Times*, Singapore, 2012

[10] M. Osborne. "*Back contact HIT solar cell from Panasonic pushes efficiency record to 25.6%"*, PVTECH, 2014, Available: http://www.pv-tech.org/news/back_contact_hit_solar_cell_from_panasonic_pushes_efficiency_record_to_25.6

# Chapter 2. Background and literature review

## §2.1 Introduction

In recent years, the increasing demand in PV for cost reductions in raw materials, manufacturing processes and operations, and the global movement towards sustainable development and carbon footprint reduction stimulated the development of several new technologies. Direct writing, also known as direct printing or digital writing, is one such emerging technology, which is a diverse, versatile and multi length scale group of process technologies [1]. Although several different definitions were proposed in the past [2-4], a more precise and accurate definition was recently proposed by Hon *et alia*: “Direct printing denotes a group of processes which are used to precisely deposit functional and/or structural materials on to a substrate in digitally defined location” [1].

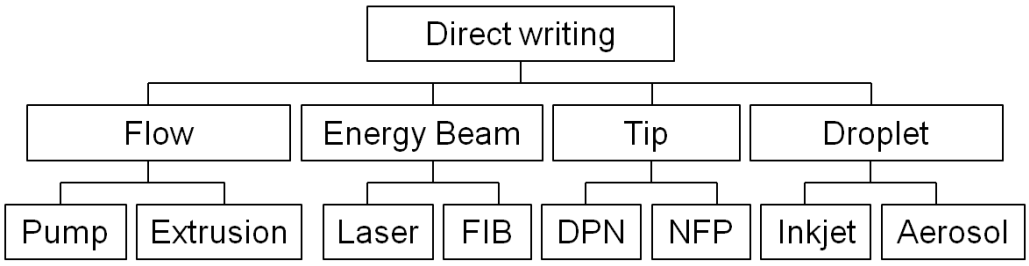


Fig. 2.1 Classification of direct writing techniques, adapted from [1].

Direct writing can be categorized into four main categories, as shown schematically in Fig. 2.1. The first category is “flow based direct writing”, which consists of micro-dispensing methods such as precision pump and extrusion methods, commonly represented by the nScrypt and the MicroPen technologies, respec-

tively. The flow based direct writing deposits features as small as 25 μm by continuously delivering flowable materials through a very small orifice or a needle. Flowable materials with a wide range of viscosity, from 1 to $10^6$ cP, can be dispensed with flow-based direct writing [5]. The second category is “energy beam based direct writing”, which typically employs high power laser or ion beams in the deposition or transfer of materials. This category of direct writing is mostly used in material subtractive applications. The laser-based direct writing is very versatile, and has been used for many processes. The focused ion beam direct writing on the other hand produces features with higher definition. However it usually requires a precursor gas and processes at a slower writing speed. The third category, “tip based direct writing”, includes dip pen nanolithography (DPN) and nano-fountain pen (NFP), whereby the molecules diffuse onto a substrate through the micro-capillary action between the tip and the surface. High resolutions of better than 100 nm can be achieved using this method, which is scalable with an array of with multiple tips. The last category is “droplet based direct writing”, which is typically represented by inkjet and aerosol printing. As the name suggests, material deposition is achieved by dispensing droplets through a nozzle. The rapid growth in the direct writing technology, particularly the inkjet printing technology, has attracted the attention of the PV industry as its unique features give it an edge over some existing technologies such as screen printing and photolithography, thus making it an excellent candidate for replacement. The rest of the chapter will be mainly focusing on the reviews of inkjet printing and aerosol printing, because these two technologies are used for the work performed in this thesis.

## §2.2 Inkjet printing

Inkjet printing is a subgroup of the droplet-based direct writing techniques. It is also the most matured form of direct writing. The first practical inkjet device, based on the continuous inkjet technology, was the Siphon recorder, which was used for the automatic recording of telegraph messages. It was invented by William Thomson in 1858 and patented in 1867 [6]. Although there was an increasing interest in inkjet-related theories thereafter [7-10], its rapid development did not take off until the release of the Mingograph in 1952, which was the first commercial inkjet device from the Siemens-Elema company [11]. In the late 1970s the technology was industrially utilized for in-line data coding and product marking. The inkjet printing technology is now widely used for product manufacturing, large-scale printing of designs and digital deposition of functional and structural materials.

Theoretically inkjet printing is nothing more than the deposition of small ink droplets onto a substrate with a print head. However, the practical implementation of the technology entails multi-disciplinary knowledge and skills. Its complexity offers a wide range of potential applications besides printing and marking, such as application of coatings, precise deposition of functional materials and even building of three dimensional fine structures and features. In some industries, inkjet printing is an excellent candidate to potentially replace some existing technologies due to the various advantages and benefits that it has to offer. Table 2.1 summarizes some of these applications and benefits.

Table 2.1 Benefit of inkjet printing for various applications [12]

| Application | Benefit of inkjet |
|---|---|
| Automotive coatings | Replaces spraying or dipping, thereby reducing waste and increasing coating uniformity. |
| Plastic part decoration | Non-contact nature accommodates curved surfaces. Improved print quality over pad or screen printing. Digital printing eliminates requirement for inventory of screens or pads, resulting in faster prototyping and a wider variety of designs. Process colour capability reduces the number of ink colours that must be stocked. |
| Conductive patterns | Minimizes waste of costly materials; very suitable for low volume manufacturing. |
| Rapid prototyping | Rapid formation of three-dimensional structures designed by using computer software. |
| Variable information | Allows fast changing of the printed information, unlike analogue printing methods which require formation of new hardware (e.g., screens in silk screen printing). |
| Ceramics | Minimizes setup time, eliminates requirement for inventory of screens. |

In general the inkjet printing technology is broadly classified as continuous inkjet printing (CIJ) and the drop on demand inkjet printing (DOD). As shown in Fig. 2.2, CIJ can be further subdivided into binary, multiple, hertz and μdot techniques; DOD on the other hand, can be primarily categorized into thermal, piezoelectric

and electrostatic techniques. Sometimes an additional category of acoustic technique is also discussed, but the print heads of acoustic DOD essentially are still based on piezoelectric or thermal inkjet printing technology.

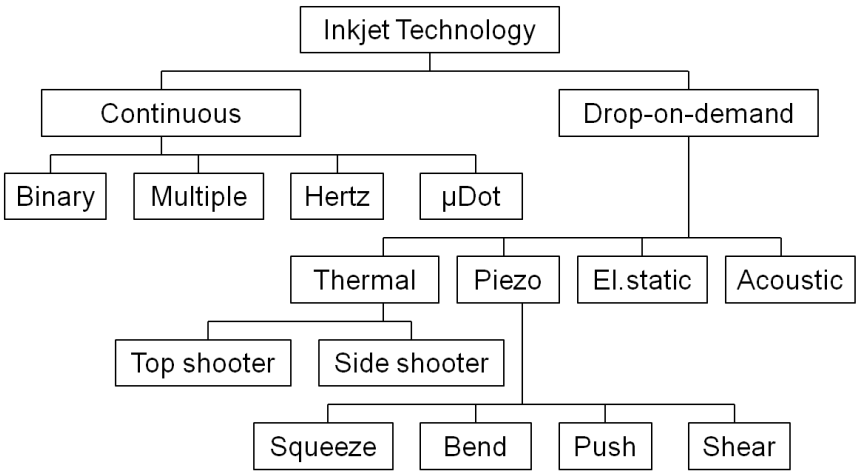


Fig. 2.2 Classification of inkjet printing technologies [13].

### §2.2.1 Continuous inkjet printing

CIJ is a printing technology commonly used for labelling and coding of products. It was also the technology employed in the first few inkjet devices, such as the Inkjet Oscillograph and the DIJIT printer. A typical CIJ print head employs the principle of the Plateau-Rayleigh instability [8], whereby a pressure wave pattern is applied to the printing nozzle, causing a continuous stream of ink to break up into droplets of uniform size and spacing at high frequency, typically in the range of 50 to 175 kHz. The droplets are then selectively charged as they pass through a charging electrode and subsequently deflected by an electric field generated underneath the charging electrodes to the desired position on the substrate. The charging system can either be binary or multiple. In a binary system, the droplets

are either charged or uncharged. The charged droplets are directed to the substrate and the uncharged captured by a gutter, and re-circulated into the system. In a multiple system, it is possible to control the amount of deflection for each droplet passing through the electrode by varying the potential of the charging electrode. The different charge magnitude of the droplets will determine the degree of deflection as they pass through the electric field. Similarly, the uncharged droplets are collected for reuse. The schematics of the binary and the multiple deflection system are shown in Fig. 2.3.

The main advantages of CIJ are its high drop frequency, which results in its high speed printing capability; and its high drop velocity, which allows for a greater distance between the print head and the substrate. These attributes make CIJ a very industrially compatible technology. Moreover, CIJ has the ability to print inks based on volatile solvents, which contributes to the rapid drying of ink upon printing and good ink adhesion to the substrate. However, the drawbacks of CIJ are its low print resolution, high maintenance requirement, and the limitation that the printed fluid has to be electrically chargeable.

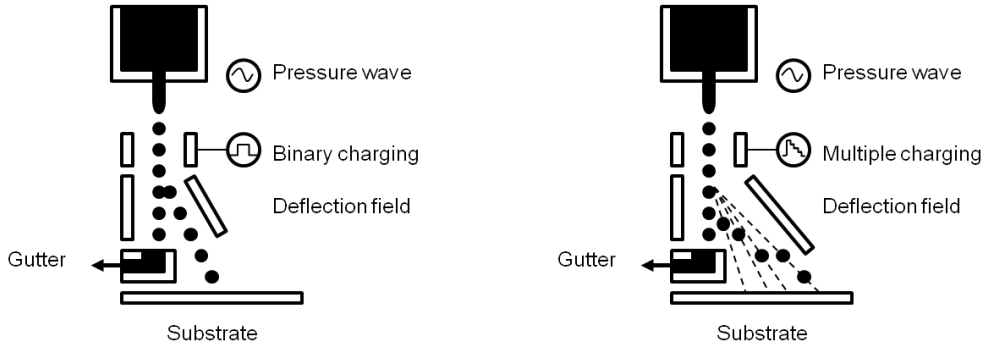


Fig. 2.3 Schematics of binary (left) and multiple (right) deflection systems, adapted from [1].

### §2.2.2 Drop-on-demand printing

The drop-on-demand inkjet printing (DOD) technology employs a different printing mechanism, in which the ink is ejected only when printing is required, as the name “drop-on-demand” suggests. DOD printers are preferred to CIJ printers as no break-off synchronization, charging, deflection, guttering and re-circulation are required. The ejection of ink is triggered by the generation of pressure pulses, typically achieved with thermal, piezoelectric or electrostatic techniques. The schematics representations of the three DOD techniques are shown in Fig. 2.4 to illustrate their respective working principles.

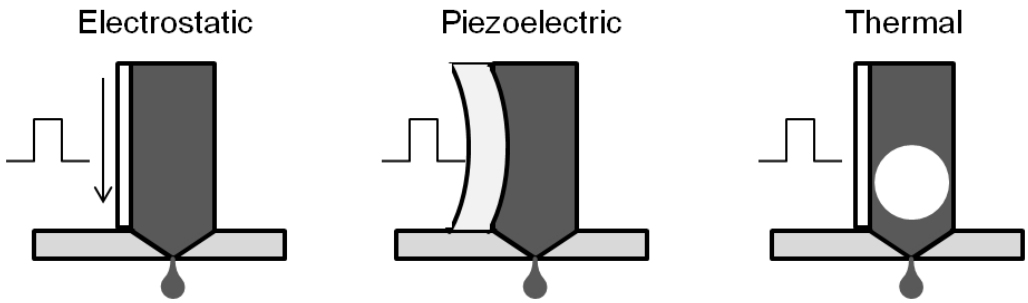


Fig. 2.4 Schematics of electrostatic, piezoelectric and thermal DOD, adapted from [12].

The first DOD inkjet printer that emerged in the 1960s was based on the electrostatic technique. A negative pressure is first applied to the nozzle to contain the conductive inks in the printing chamber. Subsequently a high voltage pulse is applied to pull the conductive ink droplets out of the nozzle when printing is required. The nature of the electrostatic DOD inkjet allows inks with a relatively higher concentration of conductive materials to be ejected from the print head. The size of the printed droplets depends on the voltage of the electrostatic pull and not the nozzle diameter, which results in a potentially smaller printed feature

size. However the functionality of the printable fluid is limited as the electrostatic DOD inkjet printing is only compatible with conductive fluids. The implementation of the technology is also costly. Therefore the other two DOD systems, namely piezoelectric and thermal are more commonly employed in industrial applications.

The thermal DOD, also known as the bubble-jet, is the printing technology commonly used in home and small office desktop printers. A small electrical heating element located in the ink cavity close to the nozzle provides rapid transient heating to the ink. This results in the vaporization of a finite volume of the ink and generates an air bubble in the ink cavity that pushes the ink out of the nozzle. When the air bubble collapses, more ink will be drawn from the reservoir to refill the cavity for ejection of subsequent droplets. Although the thermal DOD can potentially produce very small drop sizes and have high nozzle density, the technology is typically limited by its ink requirement. Besides the fact that the ink has to be vaporized, which generally limits the ink to an aqueous solvent; it also has to withstand ultra-high local temperature (~400 °C), which can also degrade the lifetime of the print heads and damage the functionality of the ink.

On the other hand the piezoelectric DOD is the preferred technology for most emerging industrial inkjet applications. In this technology an applied electric field causes distortion to a piezoelectric crystal on the print head, which generates an alternating pressure wave and changes the internal volume of the ink cavity. This alternating pressure wave mechanically pushes the ink out of the nozzle and then draws the ink from the reservoir to refill the cavity. The piezoelectric inkjet technology offers the advantages of a long print head lifetime and a high degree of freedom in terms of ink compatibility. However the relatively higher manufac-

turing cost of the piezoelectric print head limits its applications in low-end products.

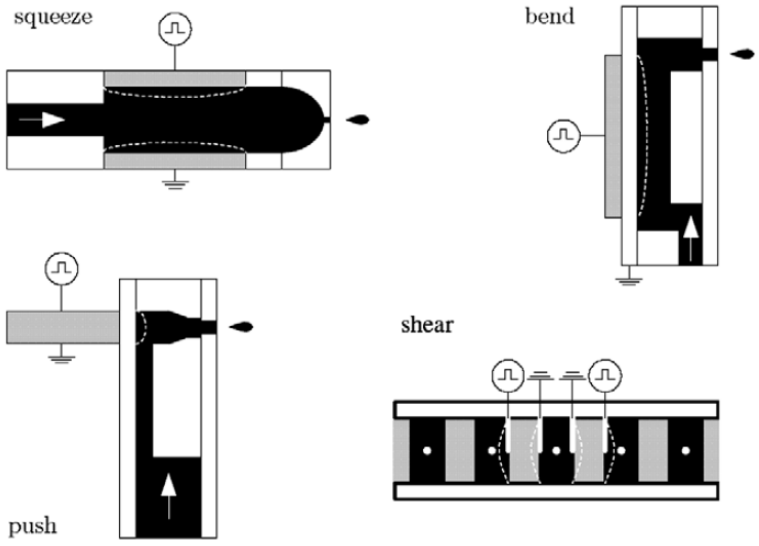


Fig. 2.5 Classifications of piezoelectric inkjet technologies by deformation modes [13].

There are four types of deformation modes to the piezoelectric crystals, as shown in Fig. 2.5, namely the squeeze, bend, push and shear modes. The ink chamber in a squeeze mode operated print head is a hollow tube of piezoelectric material, which forces an ink droplet out of the chamber when the piezoelectric tube is deformed by an applied voltage. The bend mode makes use of a flat piece of piezoelectric material to bend a wall of the ink chamber, which ejects an ink droplet. In the push mode, a piezoelectric element deforms the ink chamber above the nozzle by pushing against the ink chamber. The ink chamber wall in the shear mode operated print head is deformed by the strong shear deformation component in the piezoelectric materials. Though each mode has a different jetting mechanism, the same basic working principle applies that the ink chamber

is deformed when a voltage is applied to a piezoelectric element, thereby ejecting an ink droplet out of the nozzle.

### §2.2.3 Ink formulations

Four major types of inkjet inks are commonly used, namely phase-change [14], solvent-based [15], water-based [16], and UV curable inks [17]. Phase-change inks are typically represented by hot-melt inks, which exist as solid form at room temperature and are melted before jetting in the inkjet system. Upon reaching the viscosity and surface tension range suitable for jetting, the ink droplets will be printed onto the substrate, which is maintained at room temperature. Due to the drastic temperature difference between the substrate surface and the ink chamber, the droplets cool and solidify almost instantaneously. The rapid solidification results in minimal spreading and thus high feature definition.

The most widely used inkjet inks are solvent based inks due to their high print quality, image durability, wide range of compatible substrates and low manufacturing cost. They generally exhibit good adhesion to a variety of substrates with a fast drying time. Typically mild substrate heating is used to further accelerate the drying process. However frequent maintenance is required for the print head as the fast drying nature of the inks often results in the clogging of nozzles.

Water-based or aqueous inks are more commonly used in desktop than industrial applications. They are relatively inexpensive and mostly environmentally friendly. However the requirements for the substrates on which the water-based inks are printed are typically higher in order to achieve high feature definition and good adhesion. A surface that is too hydrophilic, typically with contact angles that are much less than 90°, results in undesirable spreading of

the printed droplets; whereas printing on a surface that is too hydrophobic causes poor adhesion.

Recent R&D in inkjet print head and ink formulation has enabled the integration of UV curing chemistry with inks and printing processes. UV curability facilitates good adhesion of inks to various substrates with near-instantaneous curing upon illumination. Inkjet printing in several industrial applications are currently making use of UV curable inks due to their flexibility. However the cost and facility requirements for the UV curing systems are limiting them from exhibiting an exponential growth.

The complexity of the inkjet printing technology places a stringent requirement on inks. Beside the need to have long shelf life, the inks also have to exhibit certain physiochemical properties so as to facilitate a stable jetting process. These conditions vary with different inkjet printing technologies. Thus, inks are usually tailored to meet specific requirements of each technology. The behaviour of liquid drops can be characterized by a number of dimensionless constants such as the Reynolds (*Re*), Weber (*We*) and Ohnesorge (*Oh*) numbers:

$$Re = \frac{v\rho\alpha}{\eta} \tag{2.1}$$

$$We = \frac{v^2\rho\alpha}{\gamma} \tag{2.2}$$

$$Oh = \frac{\sqrt{We}}{Re} = \frac{\eta}{(\gamma\rho\alpha)^{\frac{1}{2}}} \tag{2.3}$$

where $\rho$, $\eta$ and $\gamma$ are the density, dynamic viscosity and surface tension of the fluid respectively, and $v$ is the velocity and $\alpha$ is a characteristic length. As a rule

of thumb, the jetting stability of an ink is typically characterized by the parameter $Z = 1/Oh$, first proposed by Fromm [18]. Later on, Reis and Derby further refined the range of $Z$ for stable drop formation using numerical simulations to be $1 < Z < 10$ [19].

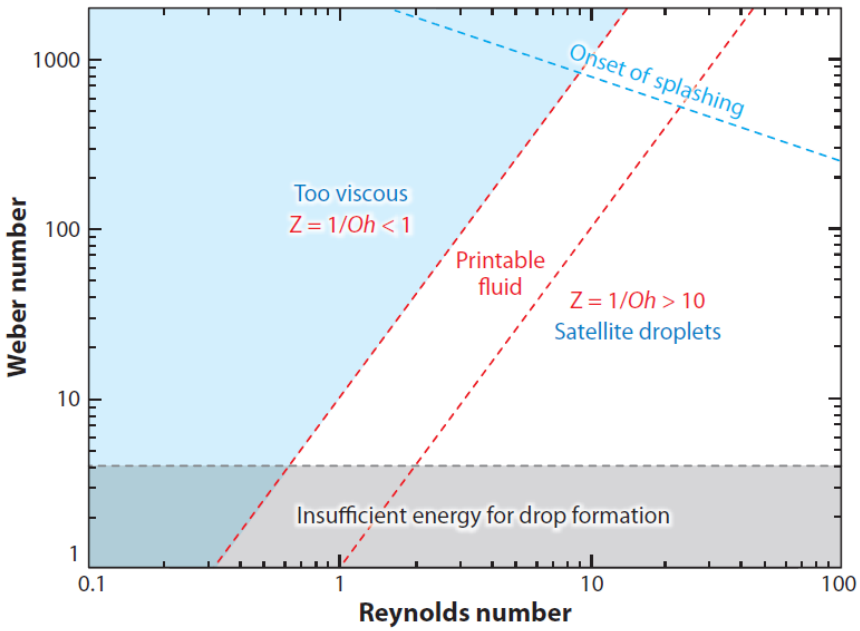


Fig. 2.6 Range of Z = 1/Oh for stable printing with respect to Reynolds number and Weber number [20].

As shown in Fig. 2.6, when $Z$ is below 1, the fluid is too viscous to be ejected through the nozzle; when Z is beyond 10, the primary drop is typically accompanied by satellite droplets. The parameter $Z$ can be adjusted to the compatible range by tuning the viscosity and surface tension of the fluid e.g. by the addition of additives. Other factors such as degassing the fluid and altering the pH value can also impact the jetting stability. A brief description of some common physiochemical properties is given in the following sections.

#### *§2.2.3.1 Viscosity*

Viscosity is a very important physical property when it comes to ink formulations. It has a great impact on the ink performance during jetting and spreading on the substrate as it determines the characteristic length scale of the internal flow phenomena in the fluid. In addition viscosity contributes to a significant portion of the total pressure that has to be overcome by the actuator to facilitate successful jetting. Assuming a Poiseuille flow profile, the pressure $p_v$ required during jetting to overcome the viscous force can be represented by [13]:

$$p_v = \frac{8\pi\eta L_n u}{A_n} \tag{2.4}$$

where $\eta$ is the viscosity, $L_n$ is the nozzle length, $u$ is the average meniscus speed and $A_n$ is the nozzle area. The ideal viscosity, typically below 20 cP for inkjet inks [12], enables the pulling and pushing of the ink in and out of the nozzle. Viscosity of a fluid can be affected by many factors such as the presence and concentration of such additives as humectants, ethylene glycol and glycerol, solvent composition and flocculation of particles. Thus, when preparing a customized jetting solution, a preliminary viscosity measurement with a viscometer prior to the jetting process can give quite an accurate prediction on the jettability of the solution and the compatible jetting waveform. Although an optimum viscosity of below 20 cP is usually desired, inks with higher viscosities at room temperature have also been successfully jetted by raising the print head temperature, as the viscosity of Newtonian fluids typically decreases with increasing temperature. However the rise in temperature can also affect other ink properties during jetting and drop breakup processes.

#### *§2.2.3.2 Surface tension*

Surface tension is another crucial jetting parameter, as it is the main driving force behind drop pinch-off [21, 22] and ink spreading upon contact [23]. The surface tension of an ink generates a capillary pressure $p_c$, which also has to be overcome by the actuator during jetting, represented as follows:

$$p_c = \frac{2\gamma \cos\theta}{R_n} \tag{2.5}$$

where $\gamma$ is the surface tension of the ink, $\theta$ is the contact angle between the ink and the nozzle and $R_n$ is the nozzle radius. If surface tension is too high, the ink cannot be jetting through the nozzle as the actuator is unable to produce enough force to overcome the capillary pressure. If surface tension is too low, the ink will stream out of the nozzle or form unstable droplets. The surface tension of an ideal ink is typically ~30 dynes/cm, which is high enough to hold the fluid in the nozzle without dripping, and yet does not result in a capillary pressure higher than that the actuator can overcome. Surface tension can be adjusted by adding surfactants and selecting proper solvent composition. Typically a surfactant is used in very low concentrations of below 1% w/w, which is already sufficient to induce a significant change in the ink performance. Beyond a concentration threshold, further addition of the surfactant does no longer alter the surface tension. The surface tension resulting from the composition of the liquid medium typically remains constant at equilibrium. Its value can be readily measured by conventional methods [23]. However, if the surface tension is tuned with the addition of surfactants, the measurement of overall surface tension should also take into consideration the contribution of dynamic surface tension [23].

#### *§2.2.3.3 pH value*

The pH value affects the inkjet performance of water-based inks most significantly due to its influence on the solubility of various components and the stability of colloidal dispersion. Water-based inks often contain polymeric binders, which are added to adjust the viscosity and surface tension of the resulting solution. Some of these polymer additives are insoluble at low pH values, thus a water-based ink typically needs to be at a high pH values to overcome the insolubility problem. The pH influences the colloidal stability of the fluid, which can be qualified by the zeta ($\zeta$) potential of particles in the fluid. The $\zeta$ potential is the electric potential difference between the dispersion medium and the stationary layer of fluid attached to the dispersed particle in a colloidal system. It indicates the degree of repulsion between adjacent and similarly charged particles in a dispersed system. A higher $\zeta$ potential usually implies a more stable system, which can be achieved by charging the adsorbed polymers by varying the pH of the system. In many aqueous media, the pH of the system is one of the most important factors affecting its zeta potential as the acidity and the alkalinity determine the amount of charges the polymer particles tend to acquire [24]. Hence if the pH value of the solution is not favourable, the polymers in the fluid will flocculate, resulting in unstable jetting.

#### *§2.2.3.4 Foaming*

Foaming is a phenomenon whereby bubbles are produced in the ink, which can be detrimental to the jetting performance. The presence of bubbles can often block the nozzles, which can cause misaligned jetting of inks or even termination of the entire jetting process. The addition of surfactants and polymers can often result in foaming. The problem can be overcome by adding a defoamer, which is

a molecule that breaks down the foams present in the system. However defoamers typically have limited solubility in the ink, and tend to precipitate from the ink with prolonged storage, which can also affect jetting significantly. Therefore the use of defoamers is often avoided or only advised in low concentrations. Another way to tackle the problem is by degassing the solution with techniques such as ultrasound degassing or vacuum pump.

## §2.3 Aerosol jet printing

Another subgroup of droplet-based direct writing techniques is aerosol jet printing, also commonly known as the Maskless Mesoscale Materials Deposition ($M^3D$), developed by Optomec Inc [25]. Instead of directly depositing individual ink droplets, aerosol jet printing dispenses a collimated aerosol beam onto the substrate at a variable stand-off (print head to substrate) distance. The technique is said to be capable of breaking through the limitations of inkjet printing, while maintaining most of its advantages. Any liquid with a viscosity of less than 5000 cP can be deposited with an aerosol printer, which significantly widens the range of printable inks and consequently the range of functional materials that can be printed. One essential part of aerosol jet printing is to place the liquid in an atomizer and create a dense aerosol of micro-droplets for printing. Depending on the viscosity of the printed fluid, the aerosol can be generated via two different methods, namely ultrasonic atomization and pneumatic atomization.

### §2.3.1 Methods of atomization

Ultrasonic atomization is typically suitable for nebulising fluids with low viscosity (~ 0.7 - 10 cP) or with suspended particles (< 50 nm) by placing a piezoelectric transducer in contact with the fluid. The piezoelectric element produces a high-frequency ultrasonic wave, which generates a vapour mist from the fluid reservoir. A carrier gas fed into the fluid reservoir then transports the vapour mist to the nozzle.

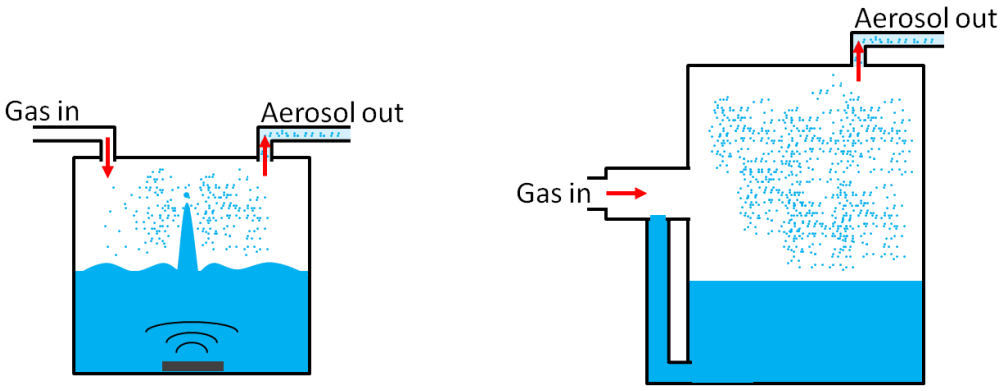


Fig. 2.7 Schematic representation of the working principle of ultrasonic atomization (left) and pneumatic atomization (right) [26].

The pneumatic atomizer is used when the nebulised fluids have much higher viscosities (~ 10 - 5000 cP) or larger suspended particles (< 0.5 µm). The carrier gas is introduced at high velocity, passing over a channel that is connected to the fluid reservoir. This results in a difference in air pressure and draws the fluid from the reservoir through the channel. The carrier gas then shears the liquid stream into droplets and produces a dense aerosol, which is subsequently transported to the nozzle. A schematic representation of the working principles of the ultrasonic atomization and the pneumatic atomization is shown in Fig. 2.7.

### §2.3.2 Beam collimation

A unique feature of aerosol jet printing is the collimation of the printed vapour mist at the deposition head. As the aerosol reaches the deposition head, it will be collimated by an incoming sheath gas, as shown in Fig. 2.8. The sheath gas surrounds the aerosol and prevents the micro-droplets and the suspended particles from coming into contact with the inner walls of the nozzle. This feature enables several advantages for the use of aerosol based direct writing techno-

logy. Besides alleviating the problem of nozzle clogging, the collimation feature also allows a jetting diameter much smaller than the nozzle diameter to be formed by adjusting the sheath gas flow rate. A larger sheath gas flow rate typically results in a smaller jetting diameter, and hence a smaller printed feature size. However increasing the sheath gas flow rate also causes the pressure to build up at the nozzle, which might lead to nozzle blocking over time. Therefore a balance between the sheath gas flow rate and the aerosol flow rate must be obtained in order to produce stable jetting and small printed feature size.

Furthermore the collimation of the aerosol enables printing at a wider range of stand-off distances, as the jetted aerosol is surrounded by the sheath gas and less likely to be affected by environmental factors upon exiting the nozzle. This also allows printing to be performed over substrates with varying topography with minimal deviation in the printed line width.

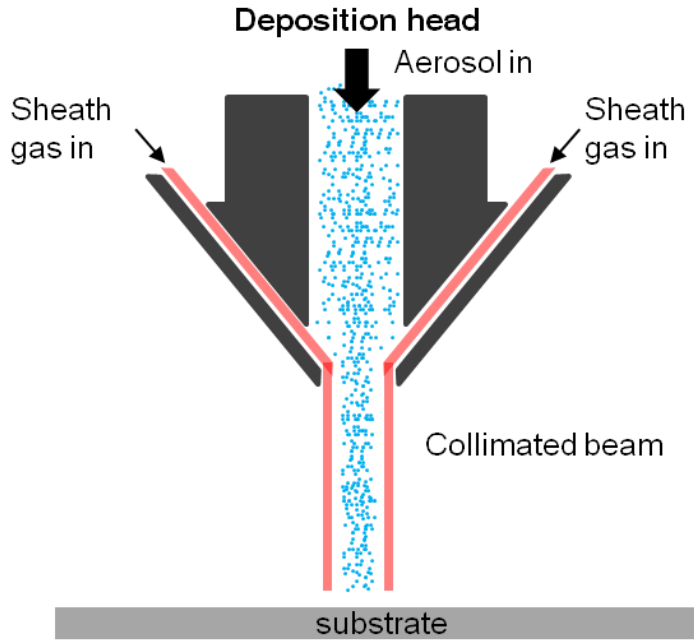


Fig. 2.8 Schematic illustration of collimation of the aerosol beam, adapted from [26].

## §2.4 Inkjet printing vs aerosol jet printing

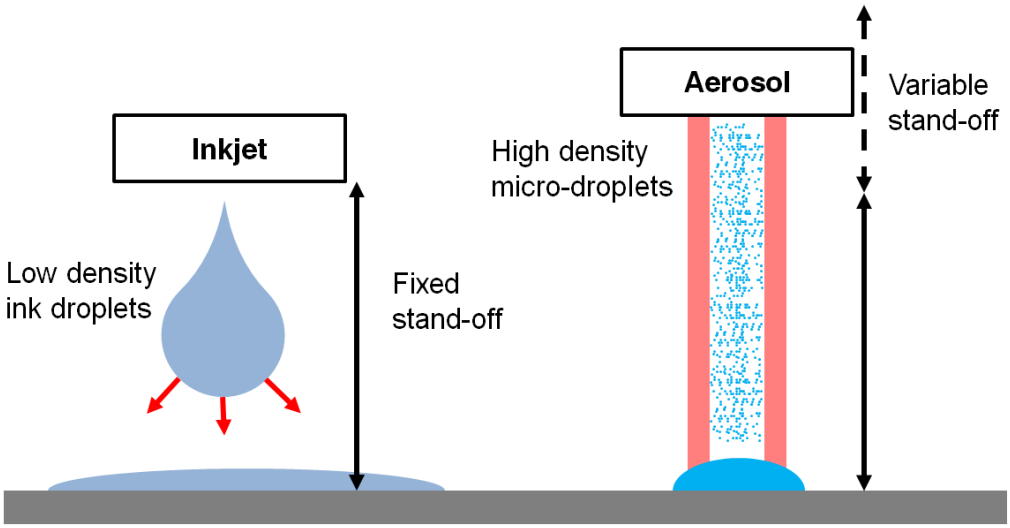


Fig. 2.9 Schematic comparison between inkjet printing and aerosol jet printing, adapted from [26].

Today, inkjet printing is one of the, if not the, most mature and widely employed technologies in the printing industry. However it has also encountered a number of intrinsic hurdles that are not easily overcome. One of these bottlenecks is the limitation on the viscosity of the printed fluids. Due to the stringent requirements for the viscosity of inks that can be inkjet printed, an inkjet printable fluid consists mostly of solvents. Two consequences arise from the printing of low-viscosity inks. The density of the ink droplets is typically low, which compromises the desired functionality of the printed fluids (i.e. to print functional materials). Low-viscosity fluids also tend to spread more easily upon impact on the substrate, which limits the minimum width of the printed features. Aerosol jet printing on the other hand is able to handle a much wider range of viscous solutions and high-density micro-droplets are typically printed. Not only does this reduce the

spreading effect, but it also increases the parameter space for the deposition of functional materials.

In addition, inkjet printing is typically optimized at a fixed stand-off distance as the printed droplets are affected by environmental factors upon exiting the nozzles. The movement of the print head and the chances of misfiring and nozzle clogging significantly influence the directionality of the printed droplets, which ultimately affects the precision of the printed pattern. In the case of aerosol jet printing these problems can potentially be solved by using a beam collimation, as shown in Fig. 2.8. The collimation of the aerosol results in a very directional printing nature, which prevents the printed aerosol from being affected by environmental factors outside of the nozzle. Unlike inkjet printing, this feature allows printing to be done at a variable stand-off distance. A comparison between inkjet printing and aerosol jet printing is schematically represented in Fig. 2.9.

## §2.5 Applications in the PV industry

Droplet-based direct writing techniques have received a fair share of attention from the photovoltaic (PV) industry in the recent years. Its unique features allow it to be used in many areas of applications, which can potentially replace some of the commonly used technologies. Some examples of these applications are given in the following sections.

### §2.5.1 Metallization

One of the main issues encountered by the PV industry today is cost reduction. In order to reduce the material cost, the thickness of the wafers used for the fabrication of solar cells is gradually decreasing. This inevitably increases the chance of wafer breakage when conventional screen printing is used for metallization. The non-contact printing feature of droplet-based direct writing techniques makes them excellent candidates to replace screen printing and the digital patterning feature omits the need for screen fabrication and facilitates flexible and fast prototyping of desired patterns.

The University Center of Excellence for Photovoltaics (UCEP) at Georgia Institute of Technology, USA collaborated with XJET Solar[1] on seed layer and full height silver metallization of silicon wafer solar cells, and produced solar cells with full ink jetted gridlines with a champion efficiency of 18.7% [27, 28]. The XJET inkjet printer has a heated substrate holder that can reach up to 230 °C, which allows fast drying of the silver inks upon deposition. However, a high-temperature substrate holder is usually not recommended as a higher proportion of additives and a less volatile solvent might be required for ink formulation, in order to produce stable and consistent jetting at elevated temperatures. This will

[1] http://www.xjetsolar.com/

inevitably compromise the proportion of conductive materials in the ink, resulting in low conductivity. The National Renewable Energy Laboratory (NREL) in the USA published initial results on various types of printed metals such as Cu and Ni, using both inkjet printing as well as aerosol jet printing [29-31]. Functional CIGS solar cells were fabricated featuring inkjet printed full silver contacts and nickel/silver bilayer contacts, with champion efficiencies of 10.7% and 11.6%, respectively [29]. The aerosol jet printing of a seed layer followed by a light-induced plating process was also studied, resulting in silicon wafer solar cells with efficiencies exceeding 20% [32, 33]. Both inkjet printing and aerosol jet printing were employed in the metallization of *n*-type silicon wafer solar cells.

### §2.5.2 Dielectric patterning

Recent developments in solar cell designs such as passivated emitter rear locally diffused (PERL) and selective-emitter solar cells often require patterning of dielectric layers. For industrial PERL or selective-emitter solar cells, laser ablation is typically used to open the dielectric films. However, laser ablation also induces some damage to the underlying silicon, which limits the potential efficiency gain. Inkjet printing has been introduced as an alternative method for opening dielectric films, as certain etchants can be inkjet or aerosol printed. Alison Lennon's group at the University of New South Wales (UNSW) developed both indirect and direct etching methods employing inkjet printing and aerosol jet printing to pattern dielectric layers [34-36]. However, both processes still have low throughput, due to the complexity of the process flows and stability issues in the jetting mechanism of the used solutions.

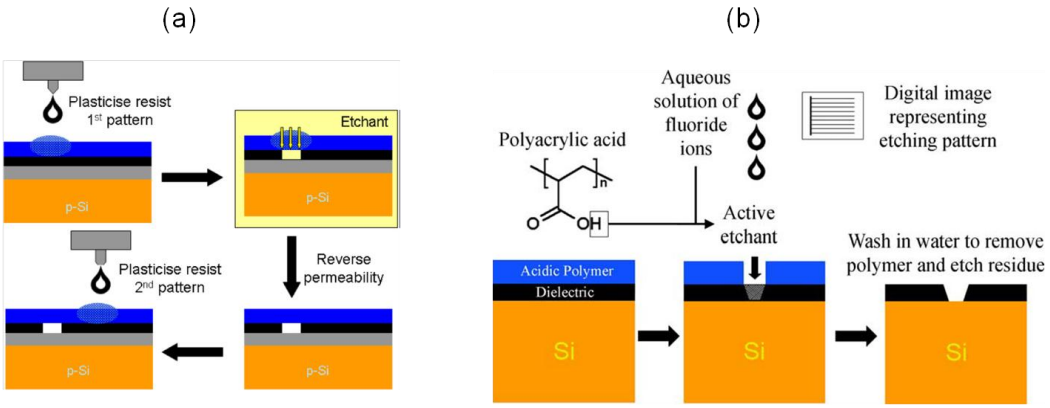


Fig. 2.10 Schematic illustration of inkjet patterning of a dielectric layer using (a) the indirect etching method [35] and (b) the direct etching method [34].

The mechanism of the indirect etching method is shown in Fig. 2.10(a). A plasticizer ink is jetted onto a resist-coated substrate, making the resist locally permeable. The sample is then immersed into etching solution and the dielectric layer underneath the permeable region is removed. A great advantage of this method is that the formation of the permeable region is reversible, by subjecting the sample to a saturated vapour of propylene glycol mono-methyl ether acetate (PGMEA) in a vacuum desiccator for 15 minutes, followed by a re-bake process at 140 °C for 10 minutes to remove excess solvents. The working principle of the direct etching method is shown in Fig. 2.10(b). The sample is first spin-coated with an acidic polymer. A fluoride containing ink is then jetted onto the acidic polymer, locally forming HF that etches through the dielectric layer.

### §2.5.3 Selective emitter

Inkjet printing can also be utilized to fabricate selective emitters of solar cells. In terms of (pre-) commercial application, the results from the companies Schmid and Innovalight are most notable. Schmid used an inkjet-printed wax in

combination with a wet-chemical etch back to obtain a selective emitter [37]. Innovalight used inkjet printing of doped Si nanoparticles with subsequent thermal diffusion for the formation of a selective emitter, however, in mass-scale manufacturing they reverted to conventional screen printing [38] for higher throughput and more reliable printing stability.

### §2.5.4 Novel ink applications

Inkjet printing, as the name suggests, consists of not only the printing technology, but also the ink technology. Novel ink formulations such as hotmelt inks and UV curable inks make it possible to print fine features (< 30 µm) with high resolution and high precision. Fraunhofer ISE in Germany, for example, used inkjet printing of hot-melt masks for metal and dielectric lift-offs [39].

## §2.6 Summary

This chapter started with an overview of direct writing methods, which comprises flow based, energy beam based, tip based and droplet based technologies. As the work of this thesis was performed solely with inkjet and aerosol jet printers, the droplet based direct writing method was discussed in some detail. For inkjet printing, a review of the different technologies and their origins were described. This was followed by a discussion of another crucial component of inkjet printing - ink formulation. The Chapter then discussed the aerosol jet printing technology, including the methods of atomization and the unique feature of beam collimation. Next, a succinct comparison between inkjet printing and aerosol printing was made. The chapter concluded with a list of current applications in the PV industry using the droplet based direct writing techniques.

## §2.7 References Chapter 2


[1] K. K. B. Hon, L. Li, and I. M. Hutchings, "Direct writing technology - advances and developments," *CIRP Annals - Manufacturing Technology,* vol. 57, p. 601, 2008.

[2] DTI, "Direct writing: Global status and opportunities for the UK in advanced manufacturing - scoping study," 2004.

[3] J. A. Lewis and G. M. Gratson, "Direct writing in three dimensions," *Materials Today,* vol. 7, p. 32, 2004.

[4] D. B. Chrisey and A. Piqué, "Introduction to direct-write technologies for rapid prototyping," in *Direct-write technologies for rapid prototyping,* San Diego: Academic Press, 2002.

[5] B. Li, P.A. Clark, and K.H. Church, "Robust direct-write dispensing tool and solutions for micro meso-scale manufacturing and packaging," in *Proc*. *International Conference on Manufacturing Science and Engineering*, Atlanta, Georgia, USA, 2007.

[6] W. Thomson, "The siphon recorder," UK Patent No 2147/1867, 1858.

[7] M. T. Plateau, "On the recent theories of the constitution of jets of liquid issuing from circular orifices," *Philosophical Magazine Series 4,* vol. 12, p. 286, 1856.

[8] L. Rayleigh, "On the instability of jets," *Proceedings of the London Mathematical Society,* vol. s1-10, p. 4, 1878.

[9] F. Savart, "Memoire sur la constitution des veines liquides lancees par des orifices circulaires en mince parol," *Ann. Chim.,* vol. 337, 1833.

[10] T. Young, "Cohesion of fluids," *Phil. Trans. R. Soc. London* vol. 95, 1804.

[11] R. Elmqvist, "Measuring instrument of the recording type," 1951.

[12] S. Magdassi, *The chemistry of inkjet inks*. World Scientific Publishing Co. Pte. Ltd, 2010.

[13] H. Wijshoff, "The dynamics of the piezo inkjet printhead operation," *Physics Reports,* vol. 491, p. 77, 2010.

[14] J. M. Berry and G. P. Corpron, "Electrostatic printing composition comprising didodecyl sebacate", US patent 3653932 A, 1972.

[15] Y. R. Bhatia and H. Stallworth, "Ink jet printing composition": US patent 7705069, 1986.

[16] A. Ahmed, C. K. Chandrasekaran, and T. E. Henzler, "Inkjet ink for textiles": US patent 20030199611, 2003.

[17] H. Noguchi and M. Shimomura, "Aqueous UV-curable ink for inkjet printing," *RadTech report,* vol. 15, p. 22, 2001.

[18] J. E. Fromm, "Numerical calculation of the fluid dynamics of drop-on-demand jets," *IBM J. Res. Dev.,* vol. 28, p. 322, 1984.

[19] N. Reis and R. Derby, "Ink jet deposition of ceramic suspensions: Modeling and experiments of droplet formation," in *Proc*. *MRS Proceedings*, p. 117, 2000.

[20] B. Derby, "Inkjet printing of functional and structural materials: Fluid property requirements, feature stability, and resolution," *Annual Review of Materials Research,* vol. 40, pp. 395, 2010.

[21] J. Lowengrub and L. Truskinovski, "Quasi-compressible Cahn-Hilliard fluids and topological transitions," *Proceeding of the Royal Society of London*, p. 2617, 1998.

[22] M. C. Pugh and M. J. Shelly, "Singularity formation in models of thin jets with surface tension," *Communications in Pure and Applied Mathematics,* vol. 51, p. 44, 1998.

[23] A. W. Adamson, "*Physical chemistry of surfaces, 5th ed."*: Wiley Interscience, 1990.

[24] R. J. Hunter, "*Zeta potential in colloid science: Principles and applications"*: Academic Press, UK, 1988.

[25] M. Renn, B. King, M. Essien, G. Marquez, M. Giridharan, and J. C. Sheu, "Apparatuses and methods for maskless mesoscale material deposition": US patent 7045015 B2, 2006.

[26] B. Kahn, "The $M^3D$ aerosol jet system, an alternative to inkjet printing for printed electronics," *Organic & Printed Electronics,* vol. 1, p. 14, 2007.

[27] A. Ebong, I. B. Cooper, K. Tate, B. Rounsaville, F. Zimbardi, V. Upadhyaya, A. Rohatgi, M. Dovrat, E. Kritchman, D. Brusilovsky, and A. Benichou, "Implementing narrow front silver gridlines through ink jet machine for high quality contacts to silicon solar cells," in *Proc*. *37th IEEE Photovoltaic Specialists Conference (PVSC)*, p. 001050, 2011.

[28] A. Ebong, B. Rounsaville, I. B. Cooper, K. Tate, A. Rohatgi, S. Glunz, M. Horteis, A. Mette, M. Gundermann, and X. Xjet, "High efficiency silicon

solar cells with ink jetted seed and plated grid on high sheet resistance emitter," in *Proc*. *35th IEEE Photovoltaic Specialists Conference (PVSC)*, p. 001363, 2010.

[29] M. F. A. M. van Hest, C. J. Curtis, A. Miedaner, R. M. Pasquarelli, K. John, P. Hersh, and D. S. Ginley, "Inkjet printed contacts for use in photovoltaics," in *Proc*. *34th IEEE Photovoltaic Specialists Conference (PVSC)*, pp. 001736, 2009.

[30] M. F. A. M. van Hest, C. J. Curtis, A. Miedaner, R. M. Pasquarelli, T. Kaydanova, P. Hersh, and D. S. Ginley, "Direct-write contacts: Metallization and contact formation," in *Proc*. *33rd IEEE Photovoltaic Specialists Conference (PVSC)*, p. 1, 2008.

[31] M. F. A. M. van Hest, S. E. Habas, J. M. Underwood, R. M. Pasquarelli, P. Hersh, A. Miedaner, C. J. Curtis, and D. S. Ginley, "Direct write metallization for photovoltaic cells and scaling thereof," in *Proc*. *35th IEEE Photovoltaic Specialists Conference (PVSC)*, p. 003626, 2010.

[32] M. Hörteis and S. W. Glunz, "Fine line printed silicon solar cells exceeding 20% efficiency," *Progress in Photovoltaics: Research and Applications,* vol. 16, p. 555, 2008.

[33] A. Mette, P. L. Richter, M. Hörteis, and S. W. Glunz, "Metal aerosol jet printing for solar cell metallization," *Progress in Photovoltaics: Research and Applications,* vol. 15, pp. 621, 2007.

[34] A. J. Lennon, A. W. Y. Ho-Baillie, and S. R. Wenham, "Direct patterned etching of silicon dioxide and silicon nitride dielectric layers by inkjet printing," *Solar Energy Materials and Solar Cells,* vol. 93, pp. 1865, 2009.

[35] A. J. Lennon, R. Y. Utama, M. A. T. Lenio, A. W. Y. Ho-Baillie, N. B. Kuepper, and S. R. Wenham, "Forming openings to semiconductor layers of silicon solar cells by inkjet printing," *Solar Energy Materials and Solar Cells,* vol. 92, p. 1410, 2008.

[36] A. Lennon, P. H. Lu, Z. Lu, and K. Wang, "Self-patterning rear contact schemes for silicon solar cells," *MRS Online Proceedings Library,* vol. 1400, 2012.

[37] Available: http://www.schmid-group.com/en/photovoltaic/cell/selective-emitter-technology.html

[38] H. Antoniadis, "Silicon ink high efficiency solar cells," in *Proc*. *34th IEEE Photovoltaic Specialists Conference (PVSC)*, p. 650, 2009.

[39] N. Mingirulli, R. Keding, J. Specht, A. Fallisch, D. Stuwe, and D. Biro, "Hot-melt inkjet as masking technology for back-contacted cells," in *Proc*. *34th IEEE Photovoltaic Specialists Conference (PVSC)*, p. 1064, 2009.

# Chapter 3. Etching of highly doped crystalline silicon in hydrofluoric acid

## §3.1 Introduction

The direct patterning processes described in this thesis are mainly applicable to the final part of the solar cell fabrication sequence. Therefore it requires proper understanding of the processes prior to direct patterning, in order to facilitate a good comparative study. Any variation in the earlier processing can result in undesirable effects to the overall performance of the solar cells. This Chapter looks into an unexpectedly high etch rate observed for heavily doped *n*-type silicon in hydrofluoric acid (HF). The observed effect is detrimental to the overall performance of the resulting solar cells, if not managed properly.

The selective removal of dielectric films is an essential process in the fabrication of microelectromechanical systems (MEMS) and other crystalline silicon (c-Si) based semiconductor devices. For this reason hydrofluoric acid (HF) - in both aqueous and vapour form - is routinely utilized in the semiconductor industry due to its highly selective etching of dielectric films over c-Si [1-3]. It has also been established previously that the etching rate of c-Si in HF is low or insignificant [4]. An in-depth study on the etch rates of c-Si in HF was done by Willeke and Kellermann [5]. They determined the room-temperature etch rates of both *n*-type (111) c-Si with a bulk resistivity in the 0.01-1000 Ωcm range and *p*-type (111) c-Si with a bulk resistivity in the 0.1-25 Ωcm range to be less than 0.01 nm/min in 50% HF [5]. They also reported an inverse relationship between the initial etch rate of c-Si

and the HF concentration. A faster etch rate of c-Si, of 0.047 nm/min, in diluted (10%) HF was previously observed by Hu and Kerr [6]. They concluded that the etching action is the result of Si oxidation by the hydroxyl ions in the aqueous solution. Jakob and Chabal performed an experiment to monitor the surface morphology of step (111) Si when it is being exposed to HF solutions buffered in $NH_4F$ and/or NaOH with various pH values [7]. They too observed that the etching rate of c-Si (111) Si in HF solutions increases with increasing pH value. The exact etching rate however was not reported. The excellent chemical stability of c-Si in HF was thus confirmed in several studies [8-14].

In recent years, there has been a growing interest in advanced industrial c-Si wafer solar cell designs that enable higher energy conversion efficiencies in a cost-effective way. Many of these designs require single-side processing of c-Si wafers, for which sacrificial masking layers, such as silicon oxide ($SiO_x$) and/or silicon nitride ($SiN_x$), are typically used [15-18]. These sacrificial masking layers are typically removed in HF solutions, as the extreme etch selectivity of HF is expected to have minimal effects on the un-masked surface regions of the c-Si wafer. However, Ebong *et al.* observed an etch back phenomenon of $n^+$ c-Si with peak doping concentration of $1.3\times10^{20}$ $cm^{-3}$ and a reduction of the surface carrier density resulting from an extended surface clean of the $n^+$ c-Si in HF [19]. The etch-back of $n^+$ c-Si in HF was also employed in the fabrication process of back contact solar cells [20]. In the present work we further investigate and show that the selectivity does not necessarily apply to highly doped *n*-type c-Si, as the etch rate of highly doped $n^+$ silicon in HF can approach 1 nm/minute. A highly doped *n*-type emitter on *p*-type c-Si, formed via dopant diffusion, is commonly used in the PV industry to form a *p*-*n* junction and a highly doped surface layer that can

be ohmically contacted with a metal electrode. The unexpectedly high etch rate significantly changes the doping characteristics of the $n^+$ emitter and thus impacts the contact formation process in the solar cell fabrication sequence, which in turn has detrimental effects on the solar cell efficiency. Based on the experimental results, we propose that heavily doped *n*-type c-Si has a different etching behaviour in dilute HF compared to lightly doped *n*-type c-Si [5]. An explanation is presented for the unusually fast etching rate observed for heavily-doped *n*-type c-Si in diluted HF that considers the contributions of: (i) hydroxide-mediated hydrolysis of silicon; and (ii) the carrier concentration dependent effects of heavily doped layers on the etching behaviour. This observed etching behaviour can potentially be exploited for device fabrication.

## §3.2 Experimental details

A batch of 25 planar Cz *p*-type (156x156 $mm^2$) monocrystalline c-Si (100) wafers with resistivity of 1.3 Ωcm ($N_a = 1.1\times10^{16}$ $cm^{-3}$) was saw damage etched in a KOH solution and subsequently underwent the RCA (Radio Corporation of America) cleaning sequence. The wafers then went through a double-sided phosphorus diffusion process. After a surface clean in diluted HF, the sheet resistances of the $n^+$ diffused emitters were measured with a four point probe (Cresbox, Napson) to have an average value of about 68 Ω/□ per side. The measurements were done in the mapping mode, using 45 measurement positions. The lateral uniformity of the sheet resistance was calculated as follows:

$$Uniformity = \frac{\max(\rho_{sheet}) - \min(\rho_{sheet})}{2 \times [\max(\rho_{sheet}) + \min(\rho_{sheet})} \times 100 \qquad (3.1)$$

One wafer was kept as a control wafer, while the remaining 24 wafers were jointly placed in the heated HF bath at 40 °C. After a certain time the wafers were removed from the HF bath, rinsed in de-ionised water and dried with $N_2$ gas one at a time at specific time intervals ranging from 1 minute to 4 hours. The sheet resistance of each wafer was measured after removal from the HF bath and DI water rinsing.

As the bath was heated from the bottom, the temperature gradient in the bath resulted in a lateral non-uniformity of the emitter sheet resistances, see Fig. 3.1. Thus, only measurements taken at the centre of the samples were used for the subsequent analysis. The doping profiles of the control sample and a few selected samples after etching were obtained with electrochemical capacitance-voltage (ECV) profiling (WEP, CVP21). Each ECV profile was calibrated with respect to the measured sheet resistance of the corresponding sample. Since

every sample underwent the same industrial diffusion process, the initial doping profiles of all the samples can be assumed to be identical.

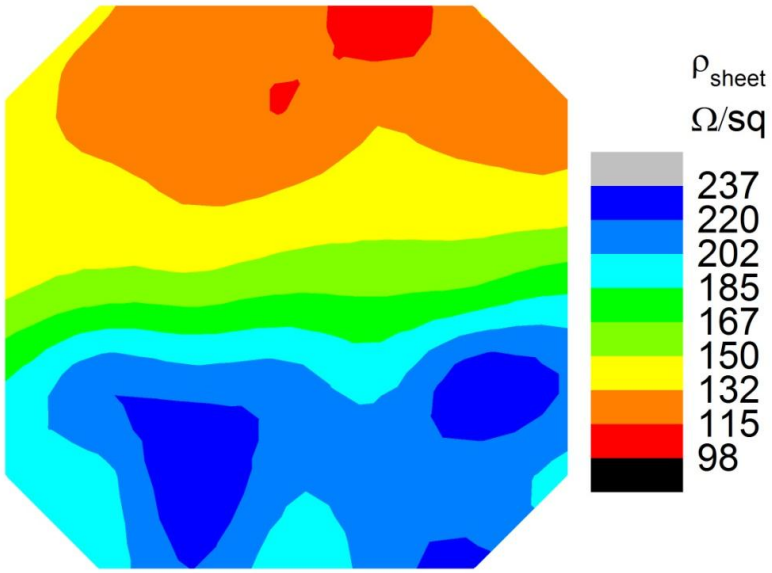


Fig. 3.1 Contour map of a 45-point sheet resistance measurement on a c-Si wafer.

## §3.3 Determining the etch rate

We checked the surface morphology with a scanning electron microscope (SEM) and observed no significant change in the surface morphology of the samples. Fig. 3.2 shows the measured sheet resistance of all investigated samples after removal from the 40 °C HF bath (and rinsing and drying), as a function of the etching time. It can be seen that the sheet resistance shows a linear dependence with the HF etching time during the early stages of etching. After about 60 minutes of HF etching, the sheet resistance starts to saturate towards a value of about 250 Ω/□. It was confirmed by hot-probe and ECV measurements that the polarity of the surface was still *n*-type, thereby confirming that the $n^+$ diffusion was only partly removed at this stage.

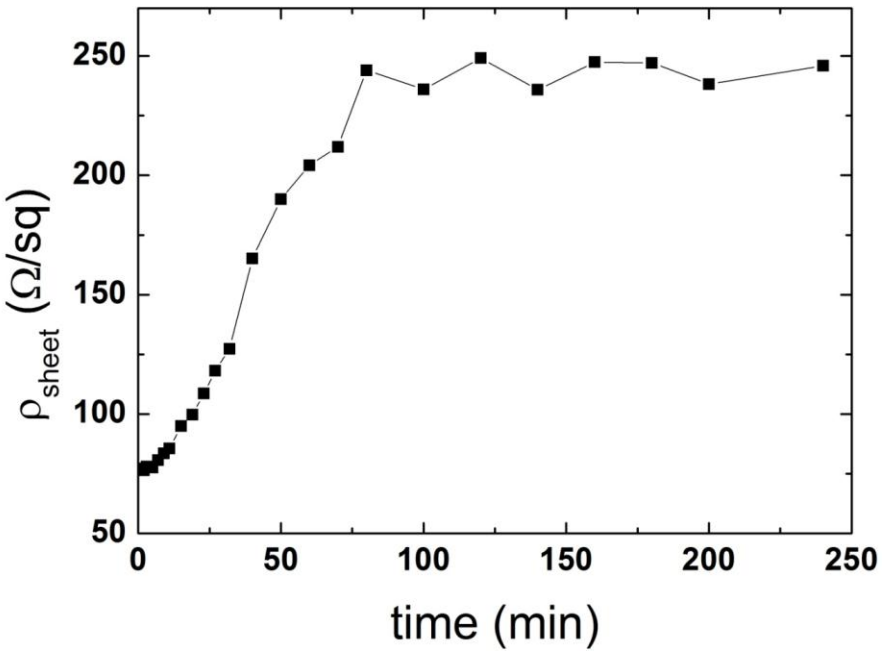


Fig. 3.2 Measured $n^+$ emitter sheet resistance as a function of the etching time in HF

To determine the Si etch rate from the experimental data of Fig. 3.2, a relationship between the etch depth and the etching time has to be established. The carrier concentration can be converted into resistivity using the following relation [21]:

$$n = \frac{6.242 \times 10^{18}}{\rho} \times 10^{\frac{A_0+A_1X+A_2X^2+A_3X^3}{1+B_1X+B_2X^2+B_3X^3}} \tag{3.2}$$

where $n$ is the carrier density, $\rho$ the resistivity, and $X$ a logarithmic function of the resistivity. $A_0$, $A_1$, $A_2$, $A_3$, $B_1$, $B_2$ and $B_3$ are constants with the values of -3.1122, -3.3347, -1.261, -0.15701, 1.0463, 0.39941 and 0.049746, respectively [21]. The corresponding sheet resistance can then be calculated with:

$$\rho_{sheet} = \frac{1}{\int_x^d \frac{1}{\rho(x)} dx} \tag{3.3}$$

where $x$ is the depth and $d$ is the junction depth.

Fig. 3.3 shows the measured active doping profile and the corresponding calculated sheet resistance as a function of the etch depth. From this data, the time dependent etch depth and its time derivative (i.e. the etch rate) can be calculated, see Fig. 3.3. During the first 40 min of etching in HF the etch depth seems to increase linearly with time, corresponding to an etch rate of 0.5-1.2 nm/min. With increasing etching time the etch rate slows down, and the etch depth seems to saturate at 43 nm. This corresponds to a sheet resistance of about 250 Ω/□ in Fig. 3.2. To confirm the etch depths calculated in Fig. 3.3, additional ECV measurements were conducted. Samples etched for 32, 50 and 200 min were taken for this analysis, as indicated in Fig. 3.4.

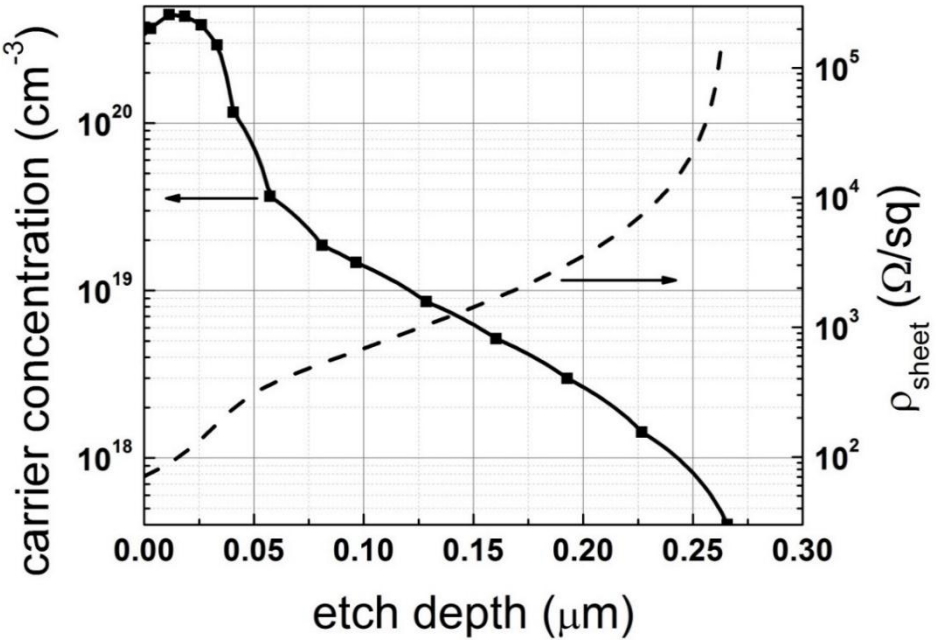


Fig. 3.3 Active $n^+$ dopant profile (filled squares with line) and corresponding calculated sheet resistance (dashed line) as a function of the etch depth of the control wafer.

The active dopant profiles are plotted in Fig. 3.5, whereby they have been offset along the *x*-axis by the etch depth calculated from the measured sheet resistance. It can be seen that the doping profiles measured by ECV generally confirm the calculated etch depths. The surface dopant concentration of the wafer that was etched in HF for 200 minutes appears to be lower than expected. Considering that the etching of silicon oxide in HF typically results in the hydrogen termination of the silicon surface [22, 23], one possible explanation for the lower-than-expected surface doping concentration of this sample is the passivation (i.e., neutralisation) of active dopants by hydrogen after extended exposure to HF. Another possible factor could be an increasing uncertainty in the ECV measurements with decreasing surface carrier concentration.

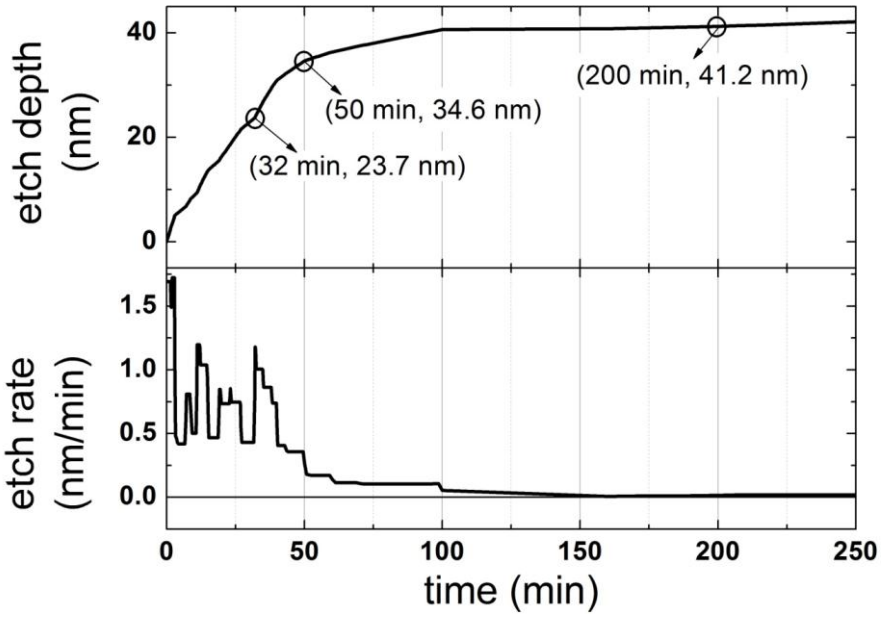


Fig. 3.4 Calculated etch depth (top) and etch rate (bottom) of $n^+$ c-Si samples as a function of the etching time. The three samples indicated by circles in the top graph were further investigated using ECV measurements, to experimentally confirm the calculated etched depth

It can be seen from Fig. 3.4 that the etching rate slows down to almost zero at an etch depth of 43 nm. To investigate the root cause of this behaviour, in Fig. 3.6 the etch rate is plotted as a function of surface carrier concentration. As can be seen, at carrier concentrations above $3\times10^{20}$ $cm^{-3}$, the etch rate is within the range of $0.8 \pm 0.4$ nm/min. Below $3\times10^{20}$ $cm^{-3}$, with decreasing carrier concentration the etch rate also decreases. When the carrier concentration crosses a value of $1.3\times10^{20}$ $cm^{-3}$, the etch rate drops to the range of $10^{-2}$ nm/min.

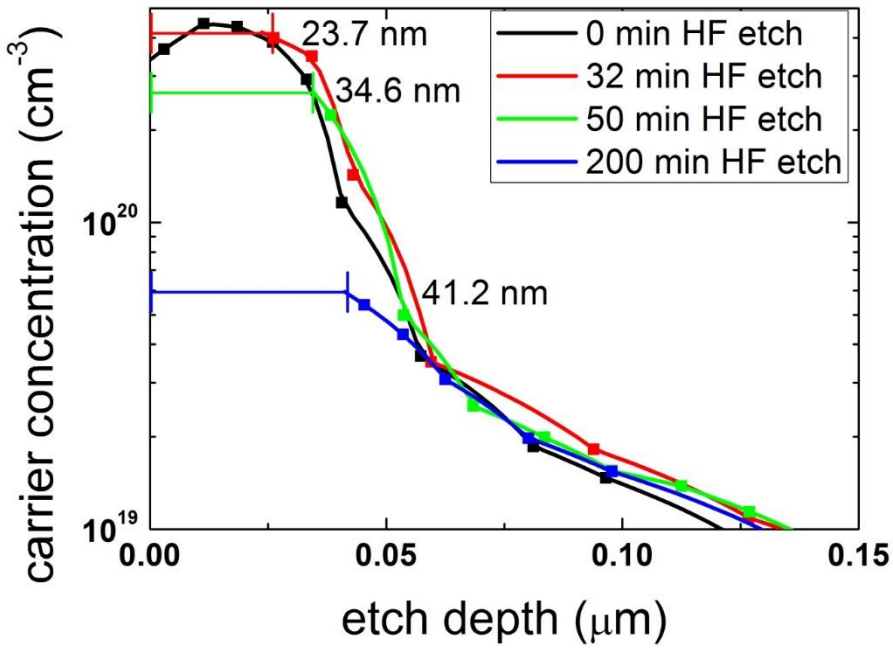


Fig. 3.5 Active $n^+$ dopant profiles determined by ECV measurements. The active doping profiles of the HF etched samples are laterally offset by the calculated etch depth shown in Fig. 3.4. It can be seen that the active dopant profiles overlap reasonably well, thereby confirming the calculated etch depths.

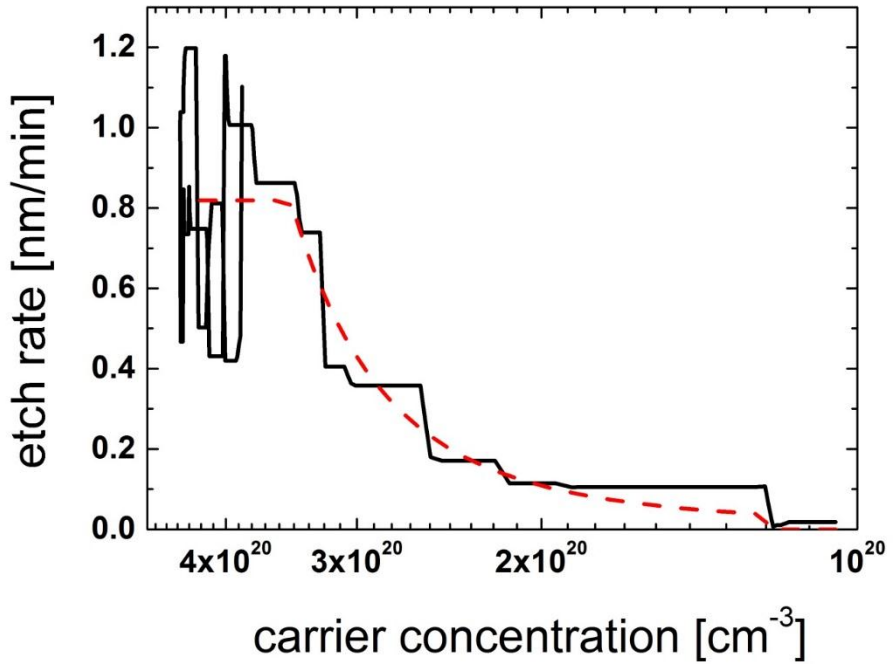


Fig. 3.6 Measured etch rate of $n^+$ c-Si as a function of the active carrier concentration in the near-surface layer. The dashed line is a guide to the eye.

As shown in Fig. 3.7, this drop in etch rate as the carrier concentration decreases below $10^{20}$ $cm^{-3}$ is in good agreement with results previously reported by other researchers. A carrier concentration of $1.3\times10^{20}$ $cm^{-3}$ corresponds to a Fermi level position of 0.11 eV below the conduction band edge, which has been identified by Kimerling as the energy level of the second acceptor level of the silicon vacancy [24]. This means that if the Fermi level of $n^+$ c-Si is above $E_C$ - 0.11 eV the silicon vacancy $V$ will be doubly charged (from here on referred to as $V^=$). On the other hand, if the Fermi level of $n^+$ c-Si drops below $E_C$ - 0.11 eV, the $V^=$ dissociates into $V^-$ and releases an electron back into the conduction band.

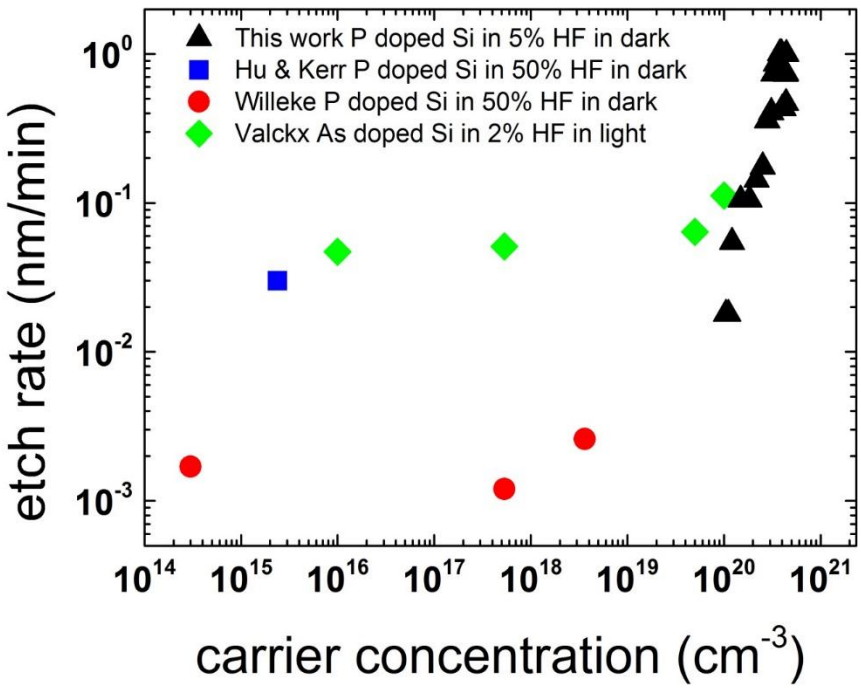


Fig. 3.7 Experimentally determined relationship between the etch rate in HF and the carrier concentration at the surface of n-type c-Si wafers. The results from the literature (square, circles and diamonds) are taken from Refs. 5, 6 and 30.

## §3.4 Etching mechanism

We believe that the fast etching behaviour is due to a combination of several etching mechanisms, one being the hydroxide-mediated hydrolysis of silicon. The etching rate of *n*-type silicon at 25 °C increases with increasing $OH^-$ concentration or pH value [6, 25]. The hydroxide-mediated hydrolysis of silicon becomes increasingly significant as the pH value increases beyond 8, and its rate increases exponentially with temperature [26]. In this work, the etching of $n^+$ silicon was performed at 40 °C in 5 % (w/w) HF, which corresponds to a pH of 4.4 and hence an $[OH^-]$ of $2.5\times10^{-10}$ M [27]. The etch rate for hydroxide-mediated etching of silicon at 40 °C is about 3 times higher than that at 25 °C [28, 29].

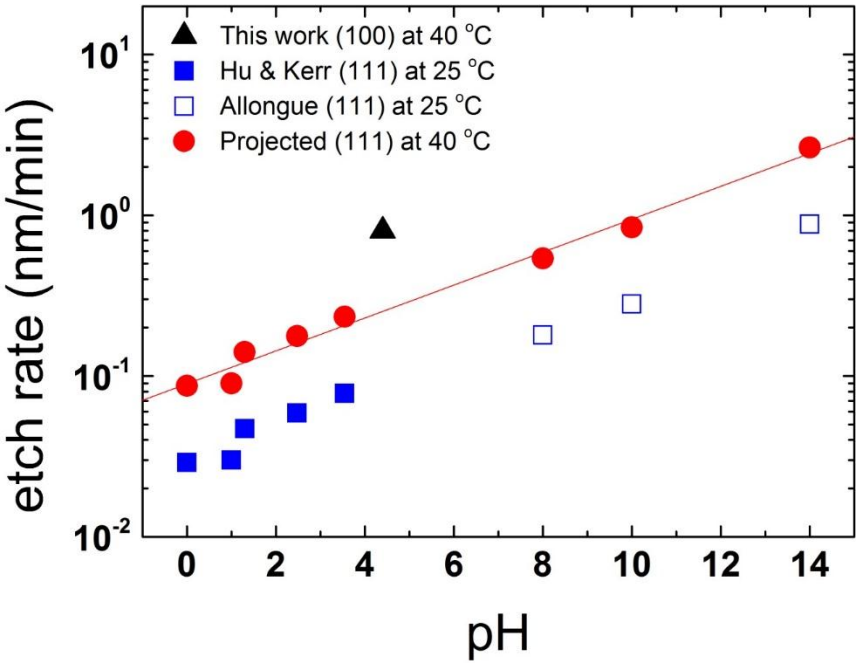


Fig. 3.8 Comparison of etch rates in HF with respect to the pH value. The open and filled squares are the results of etch rates at 25 °C taken from Refs. 5 and 25. The filled circles are their corresponding etch rates adjusted for 40 °C. The line is a linear fit of the projected logarithmic etch rates.

The etch rate observed in this work is plotted with respect to pH in Fig. 3.8 and is compared to previously reported etch rates for (111) silicon which were measured at 25 °C and have been adjusted for a temperature of 40 °C. The logarithmic etch rate demonstrates a linear relationship with increasing pH value. The etch rate observed in this work is higher than the previously reported etch rates, even if the effect of temperature is taken into consideration. Furthermore, hydroxide-mediated etching of (100) silicon is significantly faster than that of (111) silicon (which results from an alkaline-textured silicon surface) [28, 29], and therefore the expected etch rate from hydroxide-mediated etching in the current work would be expected to be lower than that for (100) silicon. Therefore it is concluded that whilst hydroxide-mediated silicon etching may contribute to the observed high etching rate, it cannot fully account for the observed etching behaviour.

Another key factor to consider is the impact of the high dopant concentration on etch rate. Valckx *et al.* also observed a higher etch rate of *n*-type silicon in 2% HF solution at high arsenic dopant concentration under light-biased etching conditions [30]. They proposed that the stress induced by the high arsenic doping level leads to amorphization to the silicon surface crystal, resulting in a higher than expected etch rate. Their reported etch rate for *n*-type silicon is included in Fig. 3.7 for comparison. Although the etch rate they observed at the carrier concentration of $10^{20}$ $cm^{-3}$ is comparable to that observed in this work, a significant difference is that the etching of silicon in this work was performed in the dark. Etching of silicon in HF is faster under illumination due to the band bending at the silicon-electrolyte interface [26]. However, the strain induced in the silicon crystal by arsenic doping is lower than that by phosphorus doping due to a greater

difference in size between silicon and phosphorus atoms [31]. The atomic radii of silicon, arsenic and phosphorus are 1.17 Å, 1.18 Å and 1.10 Å, respectively [32], which inevitably results in a larger induced stress for the phosphorus doped silicon. Moreover, as the phosphorus dopant concentration exceeds $2\times10^{19}$ $cm^{-3}$, the induced stress is already high enough to cause plastic deformation to the silicon surface [33]. Hence even though the etching process was performed without illumination, the stress induced amorphization of the silicon surface may have a significant impact on the etching behaviour as the dopant concentration increases beyond the point of plastic deformation. It may also explain the reduced etch rate with decreasing dopant concentration as the extent of amorphization is reduced at lower dopant concentrations. This contribution to the etching rate is likely to be very sensitive to the phosphorus doping profile.

High dopant concentration may also enhance vacancy-induced hole creation. Gerischer and Mindt proposed that the presence of holes plays a crucial role in initiating the chemical etching of *n*-type silicon in HF as it weakens the bonds in its vicinity and subjects the substrate atoms to nucleophilic attacks [34]. The holes are typically injected via photoexcitation or applied voltage bias, both of which were not present in this work. On the other hand Fair and Tsai proposed that as a vacancy absorbs (i.e., removes) an electron from the conduction band, a hole is simultaneously created as a free carrier in the valance band [35]. Furthermore the concentration of *n*-type silicon vacancies is expected to increase exponentially with increasing phosphorus concentration, i.e., with the shift of the Fermi level into the conduction band [32]. Thus as the carrier concentration increases beyond $1.3\times10^{20}$ $cm^{-3}$, the increasing number of doubly negatively

charged vacancies $V^{=}$ may act as a source of holes, which initiate the dissolution of *n*-type silicon in HF.

As the carrier concentration falls below $1.3\times10^{20}$ $cm^{-3}$, the dissociation of $V^{=}$ vacancies and the decrease in the total vacancy concentration result in a drastic reduction in the number of mobile holes available to kick-start the initiation process for silicon etching. This effect, coupled with the reduction in the dopant induced stress with decreasing carrier concentration, may have caused the etch rate to decrease drastically. It is therefore concluded that a number of factors may contribute to the observed high etching rate of $n^+$ silicon, however given the strong dependence of the etching rate on the $n^+$ layer's carrier concentration shown in Fig. 3.6, it is likely that mechanisms associated with the dopant concentration dominate over the hydroxide-mediated hydrolysis. Although such high etching rates for $n^+$ silicon have not been previously reported, none of the previous studies has measured the etching rate of $n^+$ Si at such high carrier concentrations and high temperature. Interestingly, this explanation of the etching mechanism implies that the etching of $n^+$ silicon in 5% (w/w) HF is self-limiting and most likely very sensitive to the nature of the phosphorus doping profile.

## §3.5 Application in solar cell fabrication sequence

### §3.5.1 Integration with $SiN_x$ mask removal

The use of a sacrificial masking layer such as $SiN_x$ and $SiO_2$ for single-side processing and its subsequent removal in HF is an essential part of the fabrication sequence of several devices [36-39]. In particular, $SiN_x$ has been used as sacrificial mask for single-side texturing and diffusion processes in the fabrication sequence of silicon solar cells [40-42]. During the mask removal process in HF, the exposed surface of the silicon wafer, which is typically heavily doped, will inevitably be affected by the etching solution. This will, for example, result in poor contact formation between the emitter and the front screen printed Ag contacts due to the increase in the sheet resistance of the unprotected $n^+$ emitter. As the etch rate of $SiN_x$ in HF is still much higher than that of $n^+$ c-Si as observed in the present work, the improved understanding of the etching of $n^+$ c-Si in heated HF can be exploited in conjunction with the mask removal process, providing a well-controlled etch-back of a heavily doped $n^+$ c-Si layer to obtain a more desirable emitter profile for solar cell fabrication.

A batch of monocrystalline Czochralski *p*-type large-area (156x156 $mm^2$) Si (100) wafers with resistivity of 1.3 Ωcm ($N_a$ = $1.1\times10^{16}$ $cm^{-3}$) was RCA cleaned and rear-side coated with a $SiN_x$ mask of a certain thickness (in the 75-150 nm range) for the subsequent front-side texturing and phosphorus diffusion. The sheet resistance of the formed $n^+$ emitter was measured as about 60 Ω/□. The removal of the rear-side $SiN_x$ mask was done in a 40 °C dilute HF bath at a concentration of 5% (w/w). Complete etching of the $SiN_x$ film is confirmed via hydrophobic surface conditions at the rear surface of the wafer. The time taken to completely

remove the masking layer was recorded for each $SiN_x$ thickness, and the resulting sheet resistance of the unprotected $n^+$ emitter was also measured with a four point probe. The results are shown in Fig. 3.9.

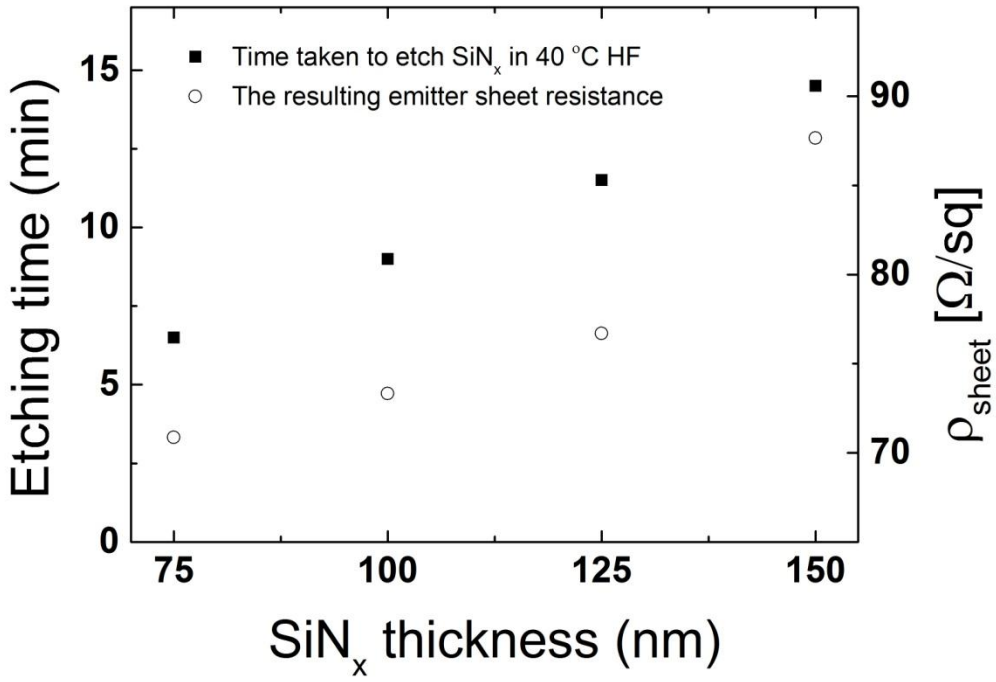


Fig. 3.9 Time taken to completely remove the $SiN_x$ mask in 40 °C HF, as well as the resulting sheet resistance on the unprotected $n^+$ emitter.

It can be seen from Fig. 3.9 that the etching time for complete removal of the $SiN_x$ mask increases linearly with $SiN_x$ thickness, as expected. The etching behaviour of the heavily doped $n^+$ c-Si manifests itself in the slight etch back of the $n^+$ emitter, resulting in an increase of the emitter sheet resistance. The sheet resistance increment is found to increase with increasing etching time. The thickness of the $SiN_x$ mask can be varied with different process requirements and sensitivities, to achieve the desired degree of protection. The corresponding

etch-back of the $n^+$ c-Si can be taken into account via the initial design of the diffusion profile.

The higher etch rate of $SiN_x$ relative to that of $n^+$ c-Si can also be exploited in device applications. For example, the etching temperature can be increased if only a slight variation in the sheet resistance is desired, as the effect of a temperature increment is more significant for the etch rate of $SiN_x$ as compared to that of $n^+$ c-Si.

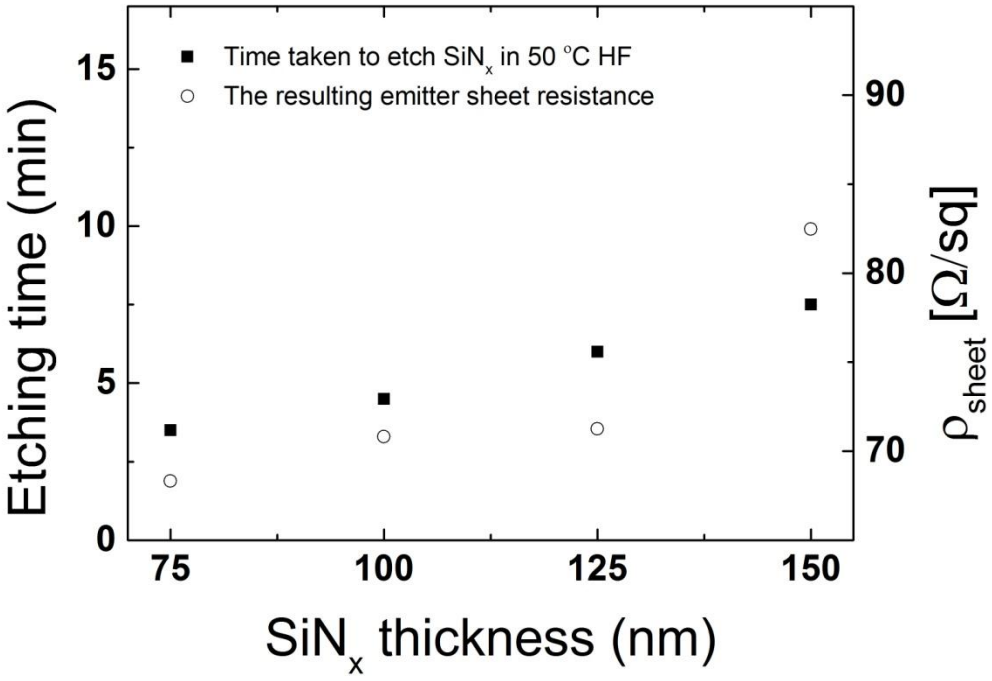


Fig. 3.10 Time taken to completely remove the $SiN_x$ mask in 50 °C HF and the resulting sheet resistance on the unprotected $n^+$ emitter.

It can be seen from Fig. 3.10 that an increase of 10 °C in the etching temperature from 40 °C to 50 °C significantly reduces the etching time required to completely remove the SiNx mask. In addition, the increment in the resulting sheet resistance of the $n^+$ emitter is comparatively lower. Therefore, the integration of the

etching of $n^+$ c-Si in HF with the mask removal process can be tailored to achieve the desired outcome, by suitably selecting the initial diffusion profile, the $SiN_x$ mask thickness, and the temperature of the HF bath.

### §3.5.2 Formation of lightly doped emitters

The self-limiting nature of the $n^+$ etching mechanism in HF can be exploited industrially to simplify the solar cell fabrication sequence. An example of its industrial application is to simultaneously achieve the formation of an advanced front emitter and the rear junction removal process when used in combination with photo-enhanced etching of silicon. A schematic representation is shown in Fig. 3.11.

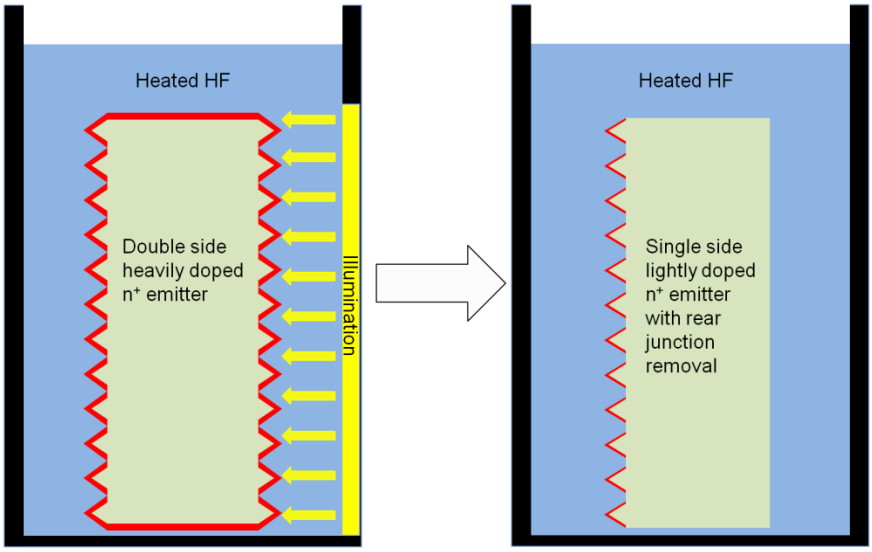


Fig. 3.11 Schematic representation of the experimental setup for simultaneously achieving an advanced front emitter and rear junction removal. This figure assumes a p-type wafer.

The etch rate of silicon in HF is significantly enhanced by illumination as hole injection can be initiated by photons [26], and is independent of the free carrier

concentration at the $n^+$ surface. By performing a double-sided $n^+$ diffusion to the *p*-type c-Si wafer, and subsequently illuminating one side of the diffused wafer during etching in heated HF, the p-n junction on the illuminated side can be removed while the self-limiting $n^+$ etching as described in the earlier section of this chapter can be achieved on the non-illuminated side. This process can form a single-side lightly doped $n^+$ emitter, which is being investigated for several solar cell applications [43-45], with a less stringent requirement on the initial design of the $n^+$ emitter profile.

A possible design of an inline tool utilizing the technology is shown in Fig. 3.12. The proposed design consists of two main chambers, namely the etching chamber and the rinsing chamber. The diffused wafers will be loaded onto a roller and transported into the etching chamber, where they will be secured by a double roller system. The bottom side of the wafers will be in direct contact with a heated HF bath for the self-limiting etching described above. The top side will also be sprayed with heated HF (via suitable nozzles). A UV lamp illuminates the wafers from the top, which will result in p-n junction removal through accelerated etching. The wafers will then be transported into the rinsing zone, whereby the top side of the wafers will be sprayed with de-ionized water via the water nozzles and the bottom side of the wafers will be in direct contact with the rinsing water bath. Subsequently the wafers will be unloaded. The etching time can be adjusted by changing the rotational speed of the rollers.

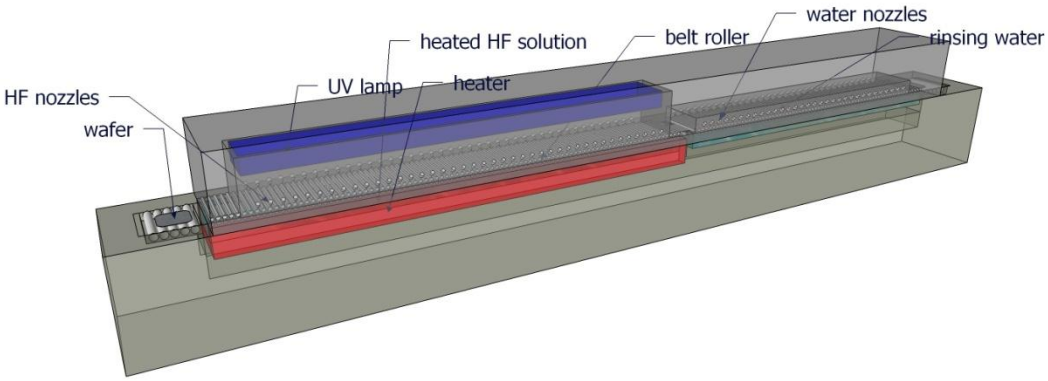


Fig. 3.12 Possible design of an inline tool.

## §3.6 Conclusion

In this Chapter, a detailed study of the etching behaviour of phosphorus emitters in a heated HF bath was carried out. By a combination of sheet resistance and active dopant profile measurements it was found that the etch rate of highly doped $n^+$ c-Si is unexpectedly high, ~0.8 nm/min for surface carrier densities of above $3\times10^{20}$ $cm^{-3}$. The etching rate was found to decrease rapidly when the surface carrier concentration dropped below $3\times10^{20}$ $cm^{-3}$. At surface carrier concentrations below $1.3\times10^{20}$ $cm^{-3}$ (which corresponds to a Fermi level position of 0.11 eV below the c-Si conduction band) the etching rate approached negligible levels of around 0.02 nm/minute. The cause of the fast etching was proposed to be related to a combination of hydroxide-mediated hydrolysis and carrier concentration dependent effects, and therefore is very sensitive to the phosphorus doping profile. This self-limiting etching behaviour of $n^+$ layers can potentially be exploited for the fabrication of advanced semiconductor devices such as solar cells. Some possible applications in solar cell fabrication sequences were described.

## §3.7 References Chapter 3

[1] K. Takagahara, K. Kuwabara, T. Sakata, H. Ishii, Y. Sato, and Y. Jin, "Selective removal of dry-etching residue derived from polymer sacrificial layer for microelectromechanical-system device fabrication," *Japanese Journal of Applied Physics,* vol. 51, p. 096502, 2012.

[2] W. S. Yang and S. W. Kang, "Comparative study on chemical stability of dielectric oxide films under HF wet and vapour etching for radiofrequency microelectromechanical system application," *Thin Solid Films,* vol. 500, p. 231, 2006.

[3] K. W. Kolasinski, "Chapter 16 growth and etching of semiconductors," in *Handbook of surface science*. vol. 3, E. Hasselbrink and B. I. Lundqvist, North-Holland, 2008.

[4] K. R. Williams and R. S. Muller, "Etch rates for micromachining processing," *Journal of Microelectromechanical Systems* vol. 5, p. 256, 1996.

[5] G. Willeke and K. Kellermann, "Crystalline silicon etching in quiescent concentrated aqueous HF solutions," *Semiconductor Science and Technology,* vol. 11, p. 415, 1996.

[6] S. M. Hu and D. R. Kerr, "Observation of etching of n-type silicon in aqueous HF solutions," *Journal of The Electrochemical Society,* vol. 114, p. 414, 1967.

[7] P. Jakob and Y. J. Chabal, "Chemical etching of vicinal Si(111): Dependence of the surface structure and the hydrogen termination on the pH of the etching solutions," *The Journal of Chemical Physics,* vol. 95, p. 2897, 1991.

[8] D. Martin Knotter and T. J. J. Denteneer "Etching mechanism of silicon nitride in HF-based solutions," *Journal of the Electrochemical Society,* vol. 148, p. F43, 2001.

[9] M. Balasubramanian, L. K. Bera, S. Mathew, N. Balasubramanian, V. Lim, M. S. Joo, and B. J. Cho, "Wet etching characteristics and surface morphology evaluation of MOCVD grown $HfO_2$ film," *Thin Solid Films,* vol. 462–463, p. 101, 2004.

[10] M. A. Quevedo-Lopez, M. El-Bouanani, R. M. Wallace, and B. E. Gnade, "Wet chemical etching studies of Zr and Hf-silicate gate dielectrics," *Journal of Vacuum Science & Technology A: Vacuum, Surfaces, and Films,* vol. 20, p. 1891, 2002.

[11] A. Witvrouw, B. Du Bois, P. De Moor, A. Verbist, C. Van Hoof, H. Bender, and K. Baert, "Comparison between wet HF etching and vapour HF etching for sacrificial oxide removal," in *Proc. SPIE 4174 Micromachining and Microfabrication Process Technology VI*, p. 130, 2000.

[12] K. R. Williams, K. Gupta, and M. Wasilik, "Etch rates for micromachining processing-part II," *Journal of Microelectromechanical Systems,* vol. 12, p. 761, 2003.

[13] C. E. Morosanu, "The preparation, characterization and applications of silicon nitride thin films," *Thin Solid Films,* vol. 65, p. 171, 1980.

[14] K. E. Bean, P. S. Gleim, R. L. Yeakley, and W. R. Runyan, "Some properties of vapour deposited silicon nitride films using the $SiH_4$-$NH_3$-$H_2$ system," *Journal of the Electrochemical Society,* vol. 114, p. 733, 1967.

[15] I. Fränz and W. Langheinrich, "Silicon nitride as a mask in phosphorus diffusion," *Solid-State Electronics,* vol. 12, p. 955, 1969.

[16] P. Ortega, G. Lopez, A. Orpella, I. Martin, M. Colina, C. Voz, S. Bermejo, J. Puigdollers, M. Garcia, and R. Alcubilla, "Crystalline silicon solar cells beyond 20% efficiency," in *Proc. 8th Spanish Conference on Electron Devices (CDE),* p. 1, 2011.

[17] S. Gatz, H. Hannebauer, R. Hesse, F. Werner, A. Schmidt, T. Dullweber, J. Schmidt, K. Bothe, and R. Brendel, "19.4%-efficient large-area fully screen-printed silicon solar cells," *Physica Status Solidi (RRL) – Rapid Research Letters,* vol. 5, p. 147, 2011.

[18] M. Ngamo, L. Tous, E. Cornagliotti, J. Horzel, T. Janssens, R. Russell, J. Poortmans, and B. Lombardet, "Integration of high sheet resistance homogeneous emitters in a process flow for PERC-type solar cells with Cu contacts," in *Proc. 38th IEEE Photovoltaic Specialist Conference (PVSC)*, p. 003371 Austin, Texas, 2012.

[19] A. Ebong, I. B. Cooper, B. Rounsaville, K. Tate, A. Rohatgi, B. Bunkenburg, J. Cathey, S. Kim, and D. Ruf, "High efficiency inline diffused

emitter (ILDE) solar cells on mono-crystalline Cz silicon," *Progress in Photovoltaics: Research and Applications,* vol. 18, p. 590, 2010.

[20] J. M. Gee and P. Hacke, "Back-contact solar cells and methods for fabrication," US Patent US20050176164A1, 2005.

[21] W. R. Thurber, R. L. Mattis, Y. M. Liu, and J. J. Filliben, "Resistivity-dopant density relationship for phosphorus-doped silicon," *Journal of The Electrochemical Society,* vol. 127, p. 1807, 1980.

[22] H. Ubara, T. Imura, and A. Hiraki, "Formation of Si-H bonds on the surface of microcrystalline silicon covered with $SiO_x$ by HF treatment," *Solid State Communications,* vol. 50, p. 673, 1984.

[23] G. F. Cerofolini, "A study of the ionic route for hydrogen terminations resulting after $SiO_2$ etching by concentrated aqueous solutions of HF," *Applied Surface Science,* vol. 133, pp. 108, 1998.

[24] L. C. Kimerling, "Influence of deep traps on the measurement of free-carrier distributions in semiconductors by junction capacitance techniques," *Journal of Applied Physics,* vol. 45, p. 1839, 1974.

[25] P. Allongue, V. Kieling, and H. Gerischer, "Etching mechanism and atomic structure of H-Si (111) surfaces prepared in $NF_4F$," *Electrochimica Acta,* vol. 40, p. 1353, 1995.

[26] K. W. Kolasinski, "Etching of silicon in fluoride solutions," *Surface Science,* vol. 603, p. 1904, 2009.

[27] H. T. Service, "Hydrofluoric acid properties," Honeywell2002.

[28] H. Seidel, L. Csepregi, A. Heuberger, and H. Baumgärtel, "Anisotropic etching of crystalline silicon in alkaline solutions: I. Orientation dependence and behavior of passivation layers," *Journal of The Electrochemical Society,* vol. 137, p. 3612, 1990.

[29] R. Hull, "Properties of crystalline silicon": Institution of Engineering and Technology, 1999.

[30] N. Valckx, D. Cuypers, R. Vos, H. Philipsen, J. Rip, G. Doumen, P. Mertens, M. Heyns, and S. D. Gendt, "Study of the etching mechanism of heavily doped Si in HF," *Solid State Phenomena,* vol. 187, p. 41, 2012.

[31] M. L. Joshi and F. Wilhelm, "Diffusion-induced imperfections in silicon," *Journal of The Electrochemical Society,* vol. 112, p. 185, 1965.

[32] M. L. Joshi and S. Dash, "Precipitation of phosphorus, arsenic, and boron in thin silicon foils," *IBM Journal of Research and Development,* vol. 11, p. 271, 1967.

[33] R. K. Jain and R. J. van Overstraeten, "Calculation of the diffusion induced stresses in silicon," *physica status solidi (a),* vol. 25, p. 125, 1974.

[34] H. Gerischer and W. Mindt, "The mechanisms of the decomposition of semiconductors by electrochemical oxidation and reduction," *Electrochimica Acta,* vol. 13, pp. 1329, 1968.

[35] R. B. Fair and J. C. C. Tsai, "A quantitative model for the diffusion of phosphorus in silicon and the emitter dip effect," *Journal of the Electrochemical Society,* vol. 124, p. 1107, 1977.

[36] J. Bühler, F. P. Steiner, and H. Baltes, "Silicon dioxide sacrificial layer etching in surface micromachining," *Journal of Micromechanics and Microengineering,* vol. 7, p. R1, 1997.

[37] D. J. Monk, D. S. Soane, and R. T. Howe, "Sacrificial layer $SiO_2$ wet etching for micromachining applications," in *Proc*. *International Conference on Solid-State Sensors and Actuators. Digest of Technical Papers, TRANSDUCERS '91*, p. 647, 1991.

[38] D. Gao, R. T. Howe, and R. Maboudian, "High-selectivity etching of polycrystalline 3C-SiC films using HBr-based transformer coupled plasma," *Applied Physics Letters,* vol. 82, pp. 1742, 2003.

[39] M. Schier, "Reactive ion etching of benzocyclobutene using a silicon nitride dielectric etch mask," *Journal of the Electrochemical Society,* vol. 142, p. 3238, 1995.

[40] V. Y. Doo, "Silicon nitride, a new diffusion mask," *Electron Devices, IEEE Transactions on,* vol. 13, p. 561, 1966.

[41] P. Papet, O. Nichiporuk, A. Kaminski, Y. Rozier, J. Kraiem, J. F. Lelievre, A. Chaumartin, A. Fave, and M. Lemiti, "Pyramidal texturing of silicon solar cell with TMAH chemical anisotropic etching," *Solar Energy Materials and Solar Cells,* vol. 90, p. 2319, 2006.

[42] J. Szlufcik, S. Sivoththaman, J. F. Nijs, R. P. Mertens, and R. Van Overstraeten, "Low-cost industrial technologies of crystalline silicon solar cells," *Proceedings of the IEEE,* vol. 85, p. 711, 1997.

[43] A. Meisel, M. Burrows, M. Abbott, F. Lemmi, and H. Antoniadis, "Impact of metal contact misalignment in silicon ink selective emitter solar cells," in *Proc*. *35th IEEE Photovoltaic Specialists Conference (PVSC)*, p. 001456, 2010.

[44] K. D. Shetty, M. B. Boreland, V. Shanmugam, J. Cunnusamy, C.-K. Wu, S. Iggo, and H. Antoniadis, "Lightly doped emitters for high efficiency silicon wafer solar cells," *Energy Procedia,* vol. 33, p. 70, 2013.

[45] Z. G. Li, K. R. Mikeska, L. Liang, A. Meisel, G. Scardera, L. K. Cheng, P. D. VerNooy, M. E. Lewittes, M. Lu, F. Gao, L. Zhang, A. F. Carroll, and C. S. Jiang, "Microstructural characterization of front-side Ag contact of crystalline Si solar cells with lightly doped emitter," in *Proc*. *38th IEEE Photovoltaic Specialists Conference (PVSC)*, p. 002196, Austin, Texas, 2012.

# Chapter 4. Geometric confinement of directly deposited features on hydrophilic rough surfaces using a sacrificial layer

## §4.1 Introduction

It is challenging to achieve high definitions for inkjet printed features on hydrophilic rough surfaces, such as a textured silicon surface coated with a dielectric film. A spreading diameter of ~5 mm is typically observed for a 10 pL inkjet droplet when printed onto a textured silicon surface coated with silicon nitride. In this Chapter, a new geometric confinement method is employed to facilitate a much higher inkjet printing definition in the range of ~50 μm, which is within the desired range for locally contacted silicon wafer solar cells.

In recent years there has been growing interest in the use of inkjet printing technology in many industries, due to its flexibility in digital prototyping and its ability to perform precise spatial deposition of structural and functional materials [1-3]. Some notable applications of inkjet printing are: the printing of cells and DNA (deoxyribonucleic acid) patterns in the life sciences industry [4, 5]; the fabrication of organic and inorganic electronic components in the microelectronic industry [6, 7]; the fabrication of layers and electrodes of organic and inorganic solar cells in the photovoltaic industry [8-10]. A major challenge for inkjet printing is to achieve high definition for the printed features, particularly on hydrophilic surfaces. The contact angle is lower when an inkjet droplet impacts a rough surface [11] and partial wetting is enhanced with the presence of topography [12],

therefore resulting in a large drop spreading area and extremely low printed feature definition.

Reduction of inkjet-printed feature sizes has been attempted through drop size modulation, ink formulation, and substrate pretreatments. Reducing the inkjet nozzle size, modifying a printhead's actuating signal, and tuning ink viscosity have been proposed as ways to modulate the printed drop size [13, 14]. For example, Meier *et al*. managed to reduce the size of an inkjet droplet deposited from a standard 10 pL printhead to only ~2 pL by tuning the driving waveform and heating the print cartridge and the substrate to 55 °C [15]. Inkjet printed lines of 25 µm width were produced. However further reductions in drop size do not lead to significant reductions in the spreading diameter on hydrophilic rough surfaces and, moreover, require more prints to achieve the required structure or functionality. Consequently, several approaches focusing on fine-tuning the physiochemical properties of the ink, as mentioned in Chapter 2, have been proposed. [16-22]. It is, however, well known that tailoring ink formulation is complex, as it requires a balance between ink jettability and functionality. Modifications to the substrate prior to inkjet printing were performed to achieve higher feature definition. One way is to create alternating hydrophobic and hydrophilic regions by photolithography, so that the spreading of the printed droplets is confined to the hydrophilic regions by the repelling hydrophobic regions [7, 23, 24]. However, the use of photolithography negates one of the main advantages intrinsic to inkjet printing, of being able to form patterns without a mask. Instead of changing surface chemical homogeneity, another approach is to modify the surface topography to physically confine inkjet printed droplets. Numerical studies demonstrated the effectiveness of a predefined surface

topography to align inkjet printed features towards critical device dimensions [25]. Hendriks *et al.* created trenches on a polymeric substrate through hot-embossing before performing inkjet printing [26]. However, this approach is not applicable to rigid substrates such as textured silicon wafers.

We report here a geometric confinement process for inkjet printing of hydrophilic rough surfaces. The process uses an organic sacrificial layer and negates the need for photolithography or complex ink formulation. Inorganic materials such as silicon oxide ($SiO_x$) and silicon nitride ($SiN_x$) are frequently used as sacrificial layers for surface micromachining and protection [27-29]. The deposition of such materials usually involves high-temperature processes or complicated chemical reactions. In this work, a water soluble polymer, polyacrylic acid (PAA), was utilised at room temperature as a sacrificial layer to change both surface chemistry and topography of a hydrophilic rough surface to assist in confining the inkjet droplet placement. PAA, when spin-coated, can form films of excellent uniformity and homogeneity [30]. The resulting film is highly soluble in water without the need for corrosive reagents and organic solvents. Another key characteristic of PAA films exploited in this study is the change of its solubility in water when heated above 170 °C [31, 32].

The confinement process was experimentally demonstrated through a subtractive inkjet printing process whereby ~200 nm of $SiN_x$ coated on an alkaline-textured silicon surface was selectively removed with multiple printing passes. Line patterns were first formed by inkjet printing $H_3PO_4$ on the spin coated PAA, which was then heated to 200 °C. The change in the PAA solubility at 200 °C enabled the confinement of the subsequently printed $H_3PO_4$ droplets which

etches through the $SiN_x$ film. Fig. 4.1 shows a schematic depicting the steps of the geometric confinement process.

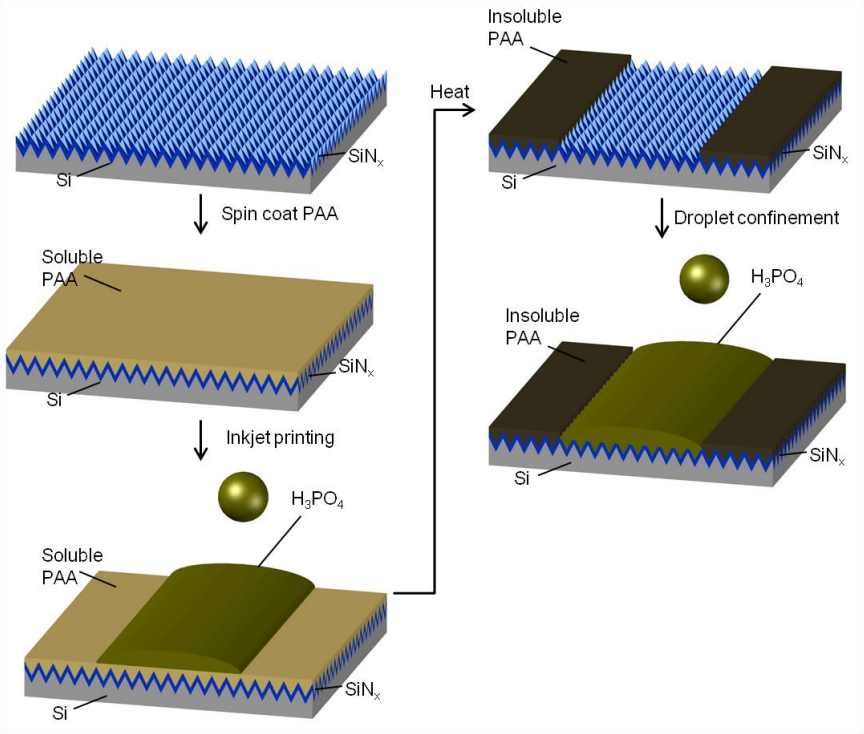


Fig. 4.1 Process flow for the selective etching of a dielectric on a hydrophilic textured silicon surface using the proposed geometric confinement process.

## §4.2 Materials and methods

Two types of monocrystalline Czochralski silicon wafers with polished (100) and alkaline-textured surfaces were used as substrates. The wafers were cleaned using the standard RCA cleaning sequence, followed by immersion in 5% (w/w) hydrofluoric acid for ~10 seconds. The wafers were then rinsed in deionised water for ~10 minutes and blown dry with a nitrogen gun. Subsequently 200 nm of $SiN_x$ was deposited on the wafers by plasma-enhanced chemical vapour deposition (PECVD, AK400, Roth & Rau). The surface roughness of polished and textured silicon wafers coated with $SiN_x$ film was less than 10 nm and 5 µm, respectively.

PAA (average molecular weight of ~ 100 kg $mol^{-1}$, 35 % (w/w) in $H_2O$, viscosity ~1030 cP, Sigma-Aldrich) was diluted to 10, 17.5, 25, and 30 % (w/w) in de-ionised water, corresponding to PAA viscosities of 12, 46, 160, and 380 cP, respectively. The viscosity of the diluted PAA solutions was measured with a Couette viscometer (DV-II+ Pro, Brookfield). The prepared PAA solutions were spin-coated (WS-650MZ-8NPP, Laurell Technologies) onto the wafers at spin speeds of 2000, 3000, 4000, 6000, and 8000 rpm. Contact angle measurements were performed on the PAA coated surfaces using a Ramé-Hart telescopic goniometer with a 2 ml syringe and 22 gauge flat-tipped needle. The probe fluid was purified water using a Millipore Milli-Q system. The PAA coating thickness on polished silicon wafers was measured with a surface profilometer (Dektak IIA, Veeco) after selectively removing the PAA layer by dipping the sample partially into deionised water. The amount of PAA spin-coated on the polished silicon wafer was compared to that on the textured silicon wafer by weighing (GR-200, A&D Company Limited) the samples before and after the spin-coating process.

A 50% (w/w) phosphoric acid ($H_3PO_4$, J.T. Baker) was inkjet printed (DMP 2831, FUJIFILM Dimatix Inc.) using 10 pL printheads (DMC-11610, FUJIFILM Dimatix Inc.) onto the PAA-coated silicon wafers. The $H_3PO_4$ solution was found to be jettable with a measured surface tension of ~76 mN/m and a viscosity of ~6 cP [33]. A customised waveform was developed to actuate the printhead at 5 kHz, producing ~10 pL droplets with a terminal velocity of 10 m/s. Multiple droplets were printed and the drop spacing (the distance between the centres of two consecutively printed droplets) was optimized to form fine grooves. The patterned samples were then baked at 200 °C in a non-fan forced LABEC general purpose oven.

As the etch rate of $SiN_x$ in $H_3PO_4$ is only significant at temperatures greater than ~180 °C [34], which is much higher than the maximum temperature obtainable (~70 °C) by the heating component of the inkjet printer, the acid was further inkjet deposited into the fine grooves and the substrate was again heated to 200 °C in an oven. The process was repeated several times in order to selectively etch through the 200 nm thick $SiN_x$ film. Finally the wafers were cleaned in piranha solution, which consisted of 98% (w/w) $H_2SO_4$ and 30% $H_2O_2$ in a 3:1 ratio, to remove the remaining PAA material. Optical microscope (BX51, Olympus) images of the etched surfaces were recorded to ensure that the PAA was fully removed after the piranha etching.

## §4.3 Results and discussion

### §4.3.1 PAA thickness

First it was necessary to calibrate the PAA layer thickness as a function of PAA concentration and the spin speed used during spin coating. The PAA layer needs to be sufficiently thin to allow full removal of the PAA film by inkjet printing of the 50% $H_3PO_4$ solution, and sufficiently thick to physically confine the droplets during the etching of the $SiN_x$ film. Furthermore, a sufficiently thick PAA coating on the textured silicon substrate is needed to smoothen the surface.

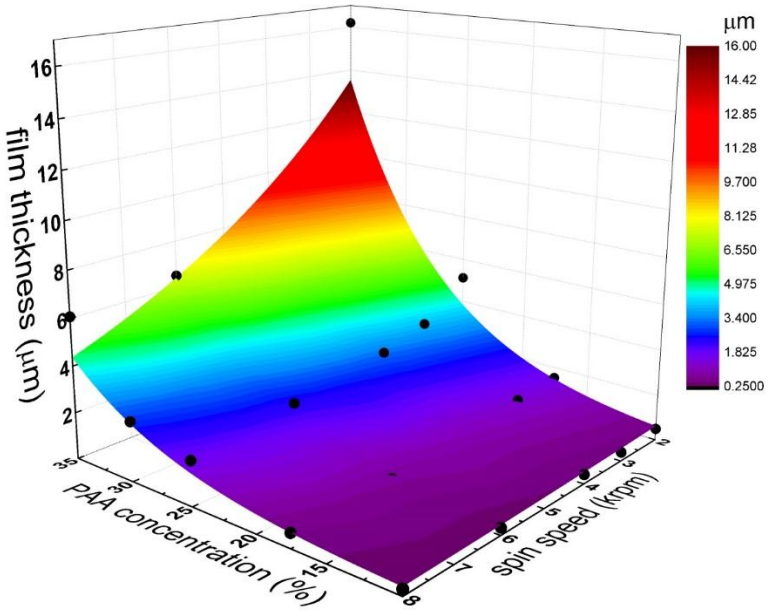


Fig. 4.2 Non-linear Gauss 2D surface fit of PAA thickness with respect to PAA concentration and spin speed. The black dots are the raw data points.

As the PAA viscosity and the spin speed significantly affect the resulting PAA thickness, these parameters were tuned to vary the PAA thickness. The resulting PAA thickness on a polished silicon wafer as shown in Fig. 4.2 was fitted as a function of the PAA concentration and spin speed, using a nonlinear fitting

method (Gauss2D model, OriginLab). Within the investigated range, the spin-coated PAA thickness increases exponentially with increasing PAA concentration and decreasing spin speed. The surface fit relates any desired PAA thickness to its required experimental conditions, which facilitates the thickness optimization process.

As it is difficult to measure the film thickness of the spin-coated PAA on a textured silicon surface, an experiment was designed to compare the PAA mass gained on a textured wafer to that on a polished wafer after the spin-coating process. Several spin-coating conditions corresponding to various film thicknesses were extracted from Fig. 4.2. These conditions were then used to spin coat PAA on both textured and polished silicon wafers. A textured and a polished silicon wafer were laser-cleaved to have an identical area (39 mm × 39 mm), and the weight gain after the spin-coating process was determined for both the wafers. For each test condition, at least three measurements were performed on both polished and textured wafers. The wafers were rinsed thoroughly in deionised water after each measurement, dried with a nitrogen gun, and reused for the next spin-coating process. The initial weight of the sample was measured to be identical, thereby indicating a thorough cleaning of the PAA from the previous spin coating step.

Fig. 4.2 clearly shows a one-to-one relationship between the spin-coated PAA weight on a textured wafer versus a polished wafer. The textured silicon surface is a special example of a rough surface, as all of the pyramids have the exact same crystal orientation while the height of the pyramids is randomly distributed in the range of 1 to 5 µm as a result of the alkaline texturing process. This results in an area factor of ~1.7 for a textured silicon surface compared to a polished

surface. However, as we are mostly interested in the thickness range where the pyramid structure of the surface is smoothed by the PAA, this difference in surface area becomes irrelevant.

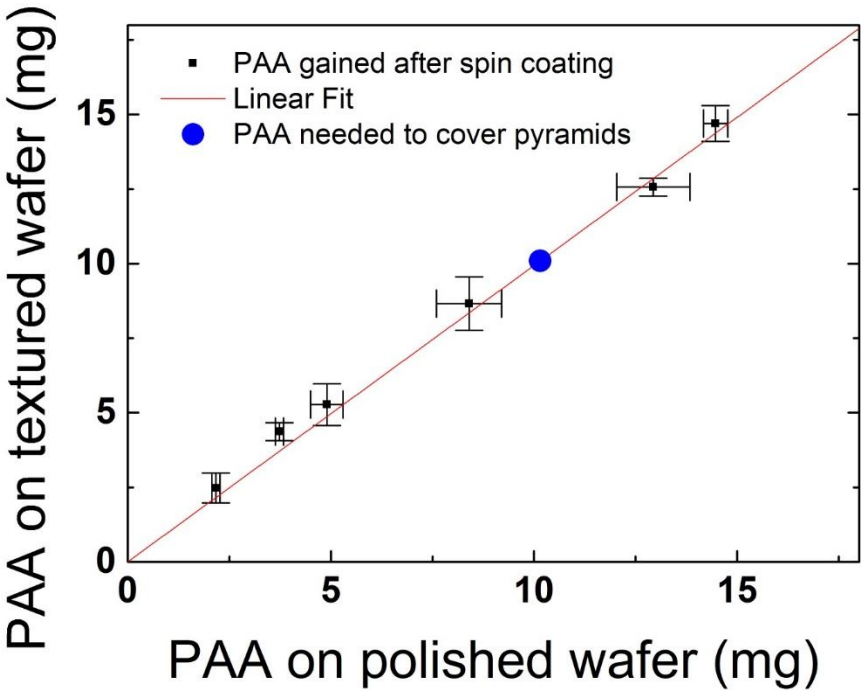


Fig. 4.3 Plot of the spin-coated PAA weight on a textured wafer versus that on a polished wafer. The error bars indicate the difference between the maximum and minimum measurements for each spin coating condition on both textured and polished wafers. The red line is a linear fit with the intercept fixed at 0. The blue circle is the amount of PAA that is required to cover the pyramids of the textured silicon.

To further illustrate this, PAA layers with a projected thickness ranging from 0.6 µm to 6 µm were spin-coated onto $SiN_x$ coated textured silicon wafers. Subsequently a single ~ 10 pL droplet of 50% (w/w) $H_3PO_4$ was inkjet deposited onto the coated surface. Micrographs of the spin-coated surface and the printed droplets are shown in Fig. 4.4. The blue spots seen in the micrographs are the pyramid structures of the alkaline-textured silicon wafers. A significant number of

pyramids are observed when the textured wafers were coated with a 0.6 µm PAA layer, suggesting that the film thickness is strongly affected by the pyramid texture. As the height of the random pyramids ranges from 1 µm to 5 µm, the number of observable pyramids decreased with increasing PAA thickness as the textured surface is gradually smoothened by an increasingly thicker PAA film. This further advocates that the difference in the surface area between a textured and a polished surface is becoming less relevant as the number of pyramids affecting the spin-coated thickness decreases. The above observation agrees well with the results from Yu *et al*. [12] whereby a similar conclusion was made for patterned nanoscale roughness. Furthermore the increasing PAA thickness also decreases the number of pyramids exposed to the subsequent etching process, which facilitates in the confinement process.

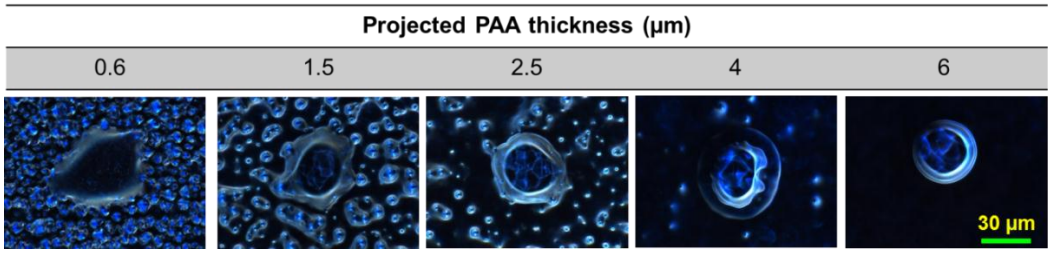


Fig. 4.4 Microscopic views (at 100 times magnification) of single inkjet printed droplets (each ~10 pL) on textured surfaces, spin coated with PAA of various apparent thicknesses. The PAA projected thickness is extrapolated from Fig. 4.2 with known PAA concentration and spin speed.

Fig. 4.4 also illustrates how the PAA coating changes the inkjet droplet spreading on textured silicon surfaces. It was observed that when an inkjet droplet impacted a $SiN_x$ coated textured silicon surface, the spreading diameter was in the range of ~5 mm, and consequently not compared in Fig. 4.4. As PAA fills up the valleys of the pyramid textured surface, both the hydrophilicity and the roughness of the

surface are reduced. This reduces the capillarity-induced spreading of the deposited droplet and improves the regularity of the spreading contact line. The resulting feature size of the deposited droplet is in the range from 40 to 60 µm, depending on the PAA thickness. It can be seen that a 0.6 µm thick PAA film is already enough to constrict the feature size to ~60 µm. However as the 0.6 µm thick PAA film is insufficient to alter the surface characteristics of the textured silicon, the deposited droplet spreads irregularly. With increasing PAA thickness, the contact line regularity of the deposited droplet continuously improves, gradually replicating that of an inkjet droplet deposited on polished silicon. When the PAA thickness is increased to 6 µm, no exposed pyramid tips remain (see Fig. 4.4), rendering a smooth and homogenous surface. The resulting feature size of the deposited droplet is reduced to ~40 µm. This indicates that, by increasingly covering a hydrophilic rough surface with chemicals of tuneable surface energy, the surface topography and hydrophilicity can be easily modified for high definition and better geometrical confinement of inkjet printed features (the contact angle of water on PAA was measured to be 63.2 ± 2.0 °).

### §4.3.2 Drop spacing optimization

It is well known that drop spacing has a significant impact on the line formation of inkjet deposited features [35]. When the drop spacing is larger than the droplet diameter, there is no overlap between two consecutively printed droplets. On the other hand, too much overlap due to small drop spacings induces the formation of so-called bulging lines, as shown in Fig. 4.5.

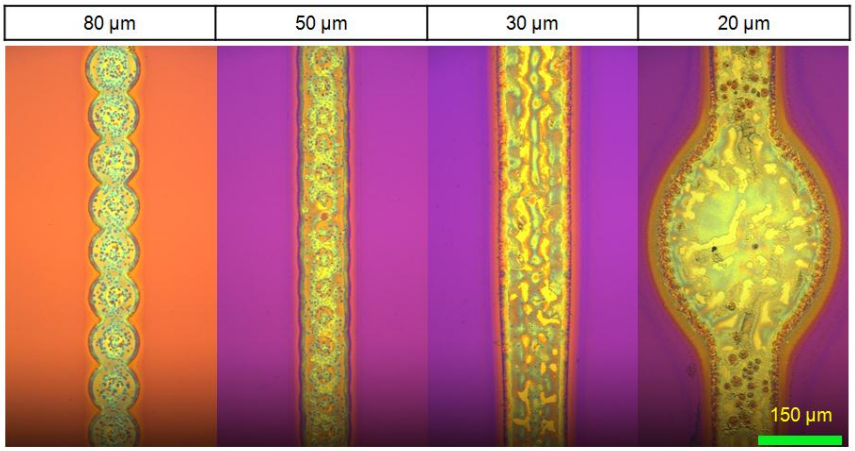


Fig. 4.5 Microscope images of various inkjet defined lines obtained by changing the drop spacing from 80 to 20 µm. The drop diameter was measured to be ~27 µm. The substrate was a 200-nm $SiN_x$ coated polished silicon wafer. The $SiN_x$ was coated with a 4-µm PAA film in order to reduce the surface's hydrophilicity. The micrographs were taken after single lines of 50% (w/w) $H_3PO_4$ 10-pL droplets were printed and the PAA film was removed by immersion in piranha solution. The colour differences of the backgrounds of the four images result from different microscope lighting conditions and should be ignored.

Fig. 4.5 shows the lines etched in a 200 nm $SiN_x$-coated polished silicon wafer after a single print of $H_3PO_4$ with a drop spacing ranging from 20 to 80 µm and a 5 minutes heat treatment at 200 °C. Upon the removal of the PAA by immersion in piranha solution, the colour difference of the etched lines observed on the $SiN_x$ indicates that the PAA was fully dissolved and a thin layer of $SiN_x$ was also removed by the $H_3PO_4$ in a single print. It is shown that the etched line formed at a drop spacing of 80 µm is marginally continuous and appears wavy, which indicates that the overlap of the printed droplets is insufficient. When the drop spacing is decreased to 50 µm, the droplets are deposited closer together and a better overlap is obtained resulting in a well-defined continuous etched line. An increase in line width was also observed with decreasing drop spacing, which is evident in the wider etched line resulting from inkjet printing at the drop spacing

of 30 µm. Further reduction in the drop spacing to 20 µm results in the formation of a bulging line. The observations made for inkjet printing of negative features are in agreement with previous studies on inkjet printing of positive features [36, 37]. It is imperative to produce well defined, yet narrow etched lines. Therefore the drop spacing of 50 µm appears to be optimal with a corresponding line width of 75 µm.

### §4.3.3 Dielectric opening

The confinement process is experimentally demonstrated through selectively etching 200 nm of hydrophilic $SiN_x$ deposited on an alkaline-textured silicon surface with pyramid height of 3 - 5 µm. The $SiN_x$ coated textured silicon surface is a special representation of a hydrophilic rough surface, on which a ~10 pL inkjet droplet (~27 µm in diameter) forms an irregular pattern with a significant spreading dimension in the millimetre range. As mentioned earlier, a PAA thickness greater than the height of the subsequently deposited droplets was required to achieve physical confinement. If the printed line is assumed to be continuous with rectangular cross-sectional area, an estimation of the line height can be obtained by:

$$h = \frac{V_{drop} \times n}{w_{line} \times l_{line}} \tag{4.1}$$

where $V_{drop}$ is the volume of a single droplet, $n$ is the number of droplets printed, and $w_{line}$ and $l_{line}$ are the width and length of the printed line. In this work, the required height of the printed lines was calculated to be about 3.5 µm. This means that physical confinement can only be achieved when the PAA thickness is greater than 3.5 µm.

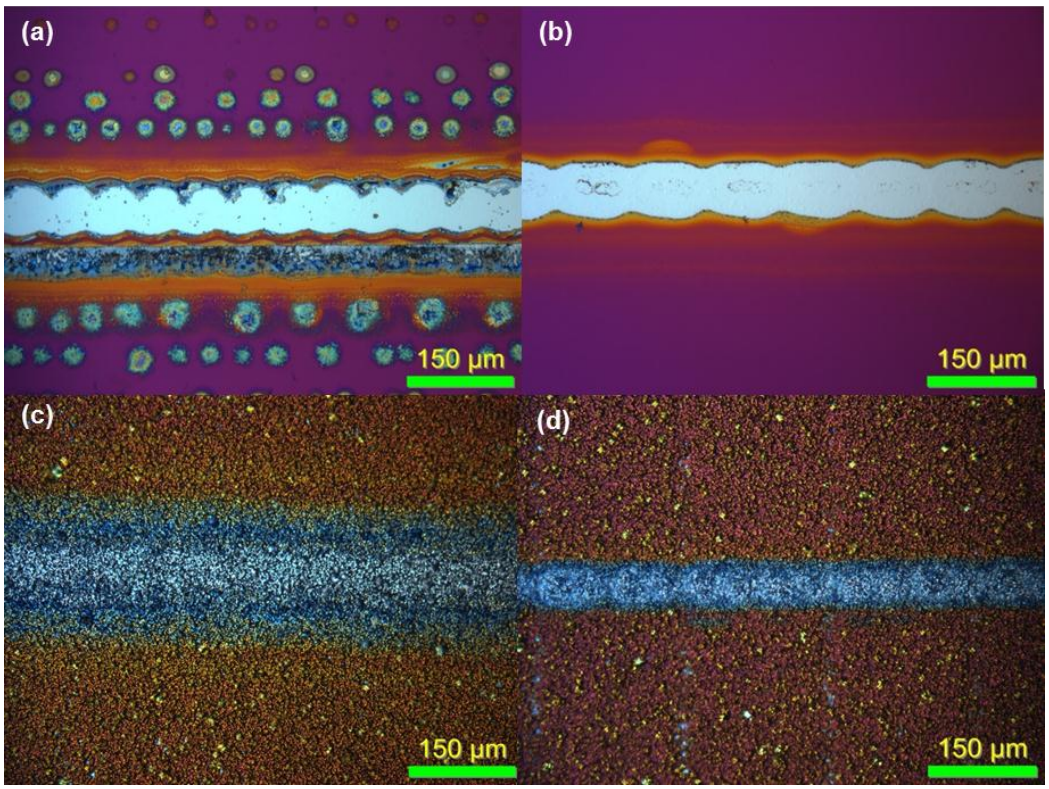


Fig. 4.6 Line openings of 200-nm $SiN_x$-coated polished silicon with (a) 1.3 µm PAA and (b) 4 µm PAA, and on a pyramid textured silicon wafer with (c) 1.3 µm PAA and (d) 4 µm PAA.

To confirm this hypothesis, etching of 200 nm $SiN_x$ on both polished and textured silicon wafers coated with 1.3 and 4 µm PAA was investigated. It was found that for PAA films with a thickness of up to 4 µm, the change in solubility can be achieved by a heat treatment at 200 °C for least 2 minutes. The impact of PAA thickness on the physical confinement process is shown in Fig. 4.6. In the case of using 1.3 µm PAA on both polished and textured substrates, as the thickness is smaller than the estimated height of the inkjet printed line, the PAA is unable to physically confine the printed $H_3PO_4$. During the initial phase of the heating process, a decrease in viscosity induces the $H_3PO_4$ to further wet the PAA surfaces on both sides of the groove. As evaporation occurs rapidly, the $H_3PO_4$

concentration increases quickly and breaks up into small droplets. The $H_3PO_4$ concentration was ~94.5 wt. % in a 200 °C ambient [34]. The small droplets left on the PAA surfaces on both sides of the groove are believed to locally etch the PAA and the underlying $SiN_x$. This phenomenon is clearly evident in Fig. 4.6 (a) and (c), whereby the $SiN_x$ on both sides of the groove is affected by the etching process. As shown in the micrographs, the interaction between the $H_3PO_4$ and the substrate surface at high temperatures is also different for polished and textured substrates. Local etching in the form of circular spots was observed on both sides of the groove formed on the polished substrate, which was not observable in the case of the textured substrates due to the surface unevenness of the sample in Fig. 4.6(c). A thinner PAA film relative to the height of the surface texture is not sufficient to alter the surface characteristics of the textured substrate. In the case of 4 µm of PAA, physical confinement of the $H_3PO_4$ was achieved when the PAA thickness was greater than the estimated height of the inkjet printed $H_3PO_4$, which prevented the $H_3PO_4$ from overflowing onto the sides of the groove. This is also shown in Fig. 4.6 (b) and (d), whereby no sign of local etching on either sides of the groove was observed.

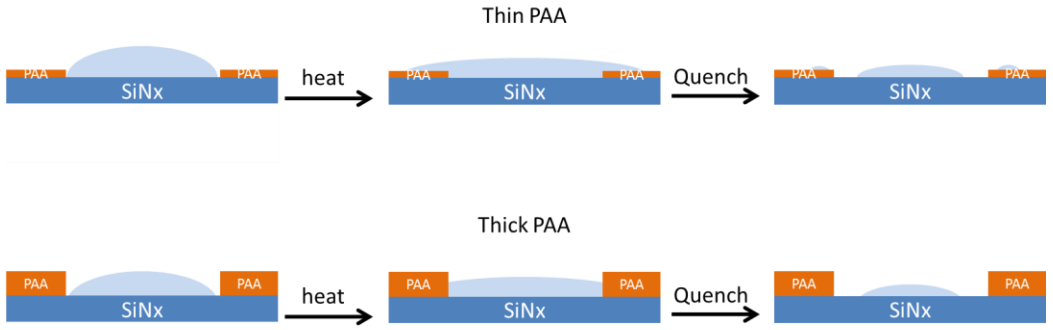


Fig. 4.7 Schematic representation of proposed explanation for Fig. 4.6.The quenching process is achieved by abruptly removing the sample from heat.

The proposed explanation is represented schematically in Fig. 4.7. It is typically difficult to achieve fine feature sizes for direct etching of thick (~200 nm) dielectric layers, as several print passes are required to completely etch such a dielectric layer. Without physical confinement, an increasing number of printing passes increases the spreading of the printed solution and results in a wider line width. Line widths in the range of 150 µm to 200 µm in ~15 printing passes were reported for direct etching of a dielectric stack consisting of 40 nm of $AlO_x$ and 100 nm of $SiN_x$, using a 10 pL printhead [38]. In comparison, the method proposed in this work is able to form a geometric confinement that significantly reduces the degree of spreading. The final line width after ~5 printing passes was measured to be ~75 µm, which did not deviate much from the line width obtained during the first printing process.

## §4.4 Design of an *in-situ* heating platform

The line width can potentially be further reduced by using a 1-pL printhead. An etched line on a polished wafer coated with 200 nm of $SiN_x$ is shown in Fig. 4.8. The line width was measured to be only ~30 µm.

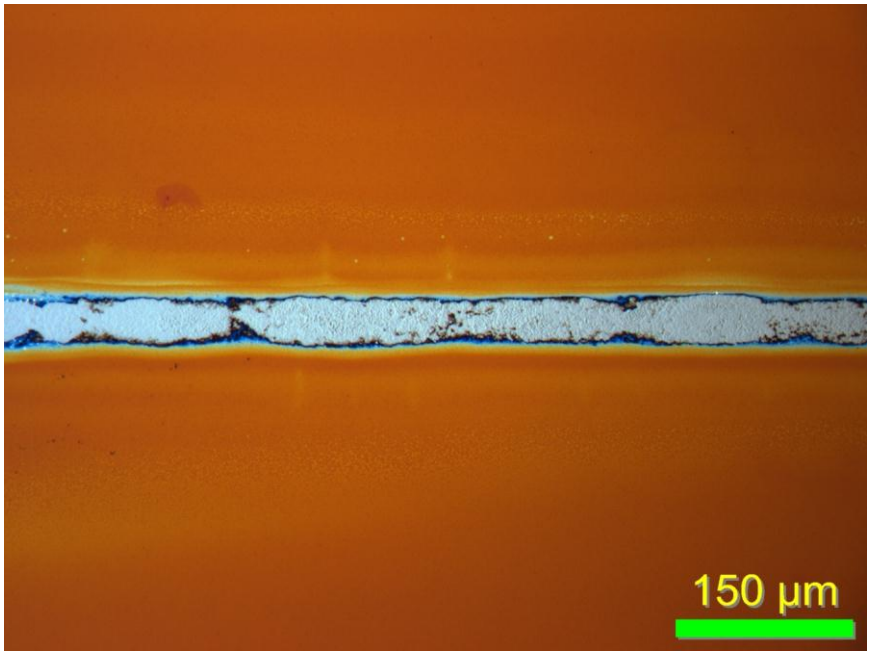


Fig. 4.8 Etched line with 1-pL printhead on a polished wafer coated with 200 nm $SiN_x$.

However as the direct etching process requires repeated printing and heating, the formation of a well-defined etch line depends heavily on the accuracy of realigning the subsequently printed droplets with the previously etched grooves after heating. The intrinsic alignment precision of the inkjet printer of about ± 5 µm therefore becomes the limiting factor affecting the definition of the printed features using the 1-pL printhead. Once the substrate is removed from the platen for heating in the oven, it is impossible to re-align the printhead back to the exact printing origin. As a consequence, the etching of the 200 nm $SiN_x$ on the polished

wafer was very inconsistent. The high visibility of the polished surface under the fiducial camera of the inkjet printer facilitated better re-alignment and enabled complete etching of some portion of the printed line. However misalignment affected other parts of the printed line and only partial etching was achieved in those regions. Re-alignment was much more problematic when the etching of $SiN_x$ was performed on a textured wafer, as the visibility under the fiducial camera was very low. No successful etching of the printed line was achieved.

The only way to overcome the alignment issue is to heat the substrate without removing it from its original printing position throughout the entire inkjet printing process. An *in-situ* heating platform, shown in Fig. 4.9, that enables substrate heating to over 200 °C was thus built in-house and placed on the platen of the inkjet printer.

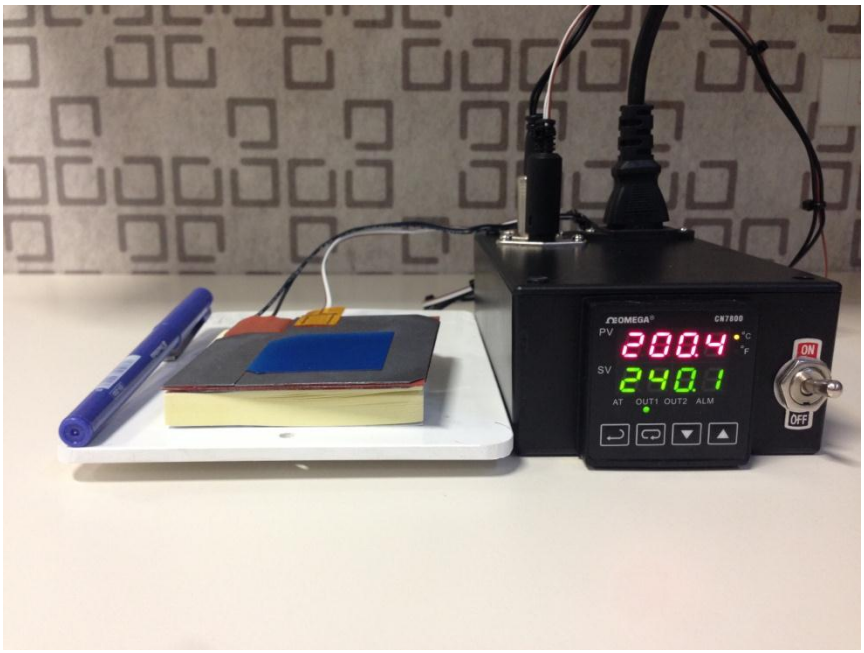


Fig. 4.9 Photograph of the in-house built *in-situ* heating platform used in this work.

The in-house built heating device comprised of a heating element (placed in between two silicon wafers to ensure that the substrate could be placed on a flat surface), a heat sensor, a switch, and a controller that regulated the temperature and displayed the set temperature and actual temperature. The heating device was able to handle Si wafer samples with a diameter of up to 3 inch.

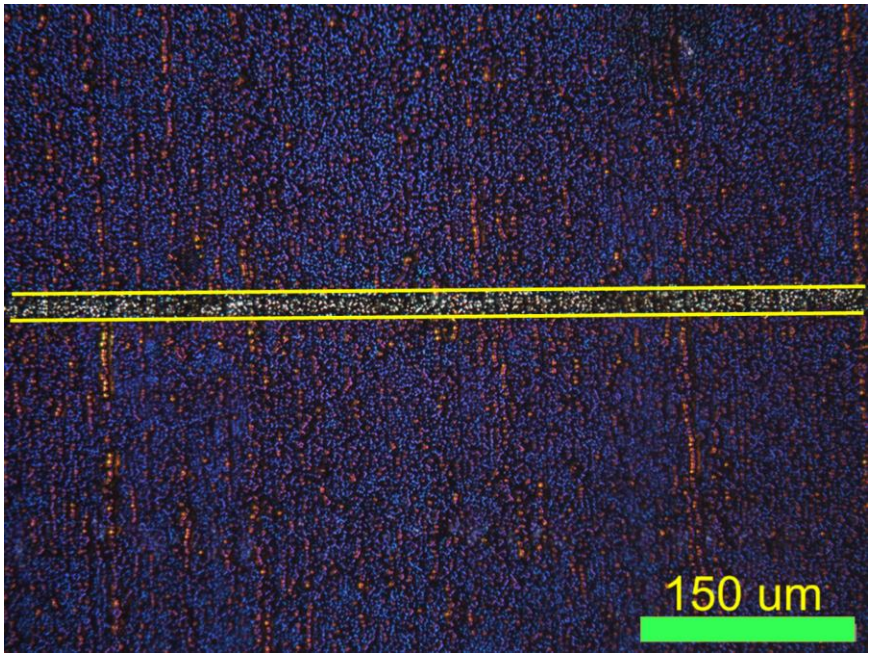


Fig. 4.10 Etched line with 1-pL printhead on a textured wafer coated with 200 nm $SiN_x$ using the in-situ heating platform to maintain the substrate temperature above 200 °C throughout the entire printing process.

Using the *in-situ* heating platform, the temperature of the substrate could be maintained at 200 °C throughout the entire printing process. As long as the substrate is kept stationary, no re-alignment is necessary. A textured wafer was coated with 200 nm of $SiN_x$ and spin coated with ~3.5 µm of PAA. The sample was then fixed to the heating platform and inkjet printed with $H_3PO_4$ at 200 °C. After 8 layers of printing, the sample was rinsed in piranha solution to remove the

insoluble PAA and the residual $H_3PO_4$. A micrograph of the etched line is shown in Fig. 4.10.

The line width of the opened dielectric layer was measured to be only ~15 µm. The feature size was reduced by a factor of two compared to the feature size obtained without using the *in-situ* heating platform. The significant reduction in the feature size can be related to two factors. Firstly, with the *in-situ* heating device in place, as long as the sample is kept stationary throughout the entire printing and heating process, the printing origin for each layer can be restored to exactly the same spot. The platen theta, which determines the relative tilt angle of the substrate with respect to the printing platen, can also be kept identical. Unless clogging of nozzles or misfiring takes place, the printing pattern of the subsequent layers will not deviate from that of the original printing layer. Secondly, it is also advantageous to perform inkjet printing at high temperatures, particularly the printing of $H_3PO_4$. When the substrate is heated to 200 °C, the viscosity of the inkjet printed $H_3PO_4$ droplets increases immediately upon impact on the substrate surface. The concentration of a heated $H_3PO_4$ solution in a reflux bath at 200 °C, as mentioned earlier, is greater than 90%. The water content of the solution decreases sharply, which results in an increase in the $H_3PO_4$ concentration and a decrease in the total mass of the printed droplets. Therefore the effective area occupied by each printed droplet is smaller. The surface tension of $H_3PO_4$ also increases with increasing temperature, which increases the contact angle of the printed droplets and minimizes the spreading diameter.

Therefore, with the advantages brought forth by the *in-situ* heating platform, in combination with the unique properties of $H_3PO_4$ at high temperatures, the line width of the printed $H_3PO_4$ could be well-controlled down to a value of 15 µm.

## §4.5 Conclusion

This Chapter described a new method for the geometric confinement of inkjet-printed features by patterning via a spin-on sacrificial layer. Physical confinement was successfully demonstrated on both polished and textured $SiN_x$-coated c-Si surfaces with a subtractive inkjet printing method, which involved using PAA as the spin-on sacrificial layer and inkjet printing of $H_3PO_4$ to selectively etch the 200 nm thick $SiN_x$ layer.

It was found that the behaviour of line formation with respect to changing drop spacing for subtractive inkjet printing is similar to that for additive inkjet printing. A large drop spacing results in the formation of a discontinuous etched line. Likewise, a small drop spacing induces the occurrence of bulging lines. It was also found that the thickness of the spin-on sacrificial layer plays a crucial role in the confinement process. A thick sacrificial layer not only confines the inkjet printed features and prevents localized etching on both sides of the main etched line, but also acts as a smoothening agent for rough surfaces. The apparent thickness of the spin-coated PAA on a textured surface was gauged relative to the true thickness of PAA on a polished surface and a one-to-one linear relationship was found. Finally, 200 nm of $SiN_x$ was successfully selectively etched on both polished and textured silicon surfaces. In each case, the final line width after repeated printing was measured to be around 75 µm, which did not deviate much from the line width obtained during the first printing process.

The line width of the patterned dielectric layer was further reduced to ~30 µm by printing with a 1-pL printhead. However, the etching was inconsistent due to the physical limitation of the inkjet printer during re-alignment. An *in-situ* heating device was therefore fabricated to eliminate the re-alignment step. The advan-

tages of *in-situ* heating and the unique properties of $H_3PO_4$ at high temperature resulted in the high definition of the printed lines of ~15 µm.

The physical confinement described in this Chapter is not limited to the subtractive inkjet printing application and the usage of PAA as the base material for the sacrificial layer. The process can also be coupled with additive inkjet printing or aerosol printing. Furthermore, the sacrificial layer can also be modified and tuned for other applications.

## §4.6 References Chapter 4

[1] P. Calvert, "Inkjet printing for materials and devices," *Chemistry of Materials,* vol. 13, p. 3299, 2001.

[2] B. J. de Gans, P. C. Duineveld, and U. S. Schubert, "Inkjet printing of polymers: State of the art and future developments," *Advanced Materials,* vol. 16, p. 203, 2004.

[3] M. Singh, H. M. Haverinen, P. Dhagat, and G. E. Jabbour, "Inkjet printing - process and its applications," *Advanced Materials,* vol. 22, p. 673, 2010.

[4] T. Goldmann and J. S. Gonzalez, "DNA-printing: Utilization of a standard inkjet printer for the transfer of nucleic acids to solid supports," *Journal of Biochemical and Biophysical Methods,* vol. 42, p. 105, 2000.

[5] E. A. Roth, T. Xu, M. Das, C. Gregory, J. J. Hickman, and T. Boland, "Inkjet printing for high-throughput cell patterning," *Biomaterials,* vol. 25, p. 3707, 2004.

[6] N. Stutzmann, R. H. Friend, and H. Sirringhaus, "Self-aligned, vertical-channel, polymer field-effect transistors," *Science,* vol. 299, p. 1881, 2003.

[7] H. Sirringhaus, T. Kawase, R. H. Friend, T. Shimoda, M. Inbasekaran, W. Wu, and E. P. Woo, "High-resolution inkjet printing of all-polymer transistor circuits," *Science,* vol. 290, p. 2123, 2000.

[8] V. Fauzia, A. A. Umar, M. M. Salleh, and M. Yahya, "Optimizing of the inkjet printing technique parameters for fabrication of bulk heterojunction organic solar cells," in *Proc*. *Semiconductor Electronics (ICSE), 2010 IEEE International Conference*, p. 60, 2010.

[9] A. Ebong, I. B. Cooper, K. Tate, B. Rounsaville, F. Zimbardi, V. Upadhyaya, A. Rohatgi, M. Dovrat, E. Kritchman, D. Brusilovsky, and A. Benichou, "Implementing narrow front silver gridlines through ink jet machine for high quality contacts to silicon solar cells," in *Proc*. *37th IEEE Photovoltaic Specialists Conference (PVSC)*, p. 001050, 2011.

[10] A. J. Lennon, R. Y. Utama, M. A. T. Lenio, A. W. Y. Ho-Baillie, N. B. Kuepper, and S. R. Wenham, "Forming openings to semiconductor layers of silicon solar cells by inkjet printing," *Solar Energy Materials and Solar Cells,* vol. 92, p. 1410, 2008.

[11] L. Gao and T. J. McCarthy, "How Wenzel and Cassie were wrong," *Langmuir,* vol. 23, p. 3762, 2007.

[12] G. McHale, N. J. Shirtcliffe, S. Aqil, C. C. Perry, and M. I. Newton, "Topography driven spreading," *Physical Review Letters,* vol. 93, p. 036102, 2004.

[13] A. U. Chen and O. A. Basaran, "A new method for significantly reducing drop radius without reducing nozzle radius in drop-on-demand drop production," *Physics of Fluids,* vol. 14, p. L1, 2002.

[14] O. A. Basaran, H. Gao, and P. P. Bhat, "Nonstandard inkjets," *Annual Review of Fluid Mechanics,* vol. 45, p. 85, 2013.

[15] H. Meier, U. Löffelmann, D. Mager, P. J. Smith, and J. G. Korvink, "Inkjet printed, conductive, 25 µm wide silver tracks on unstructured polyimide," *Physica Status Solidi (A),* vol. 206, p. 1626, 2009.

[16] C. W. Sele, T. von Werne, R. H. Friend, and H. Sirringhaus, "Lithography-free, self-aligned inkjet printing with sub-hundred-nanometer resolution," *Advanced Materials,* vol. 17, p. 997, 2005.

[17] A. Fallisch, D. Stuwe, R. Neubauer, D. Wagenmann, R. Keding, J. Nekarda, R. Preu, and D. Biro, "Inkjet structured EWT silicon solar cells with evaporated aluminum metallization and laser-fired contacts," in *Proc*. *35th IEEE Photovoltaic Specialists Conference (PVSC)*, p. 003125, 2010.

[18] F. Gao and A. A. Sonin, "Precise deposition of molten microdrops: The physics of digital microfabrication," *Proceedings of the Royal Society of London. Series A: Mathematical and Physical Sciences,* vol. 444, p. 533, 1994.

[19] N. Mingirulli, R. Keding, J. Specht, A. Fallisch, D. Stuwe, and D. Biro, "Hot-melt inkjet as masking technology for back-contacted cells," in *Proc*. *34th IEEE Photovoltaic Specialists Conference (PVSC)*, p. 1064, 2009.

[20] S. Schiaffino and A. A. Sonin, "Molten droplet deposition and solidification at low weber numbers," *Physics of Fluids,* vol. 9, p. 3172, 1997.

[21] S. Schiaffino and A. A. Sonin, "Formation and stability of liquid and molten beads on a solid surface," *Journal of Fluid Mechanics,* vol. 343, p. 95, 1997.

[22] A. M. J. van den Berg, A. W. M. de Laat, P. J. Smith, J. Perelaer, and U. S. Schubert, "Geometric control of inkjet printed features using a gelating polymer," *Journal of Materials Chemistry,* vol. 17, p. 677, 2007.

[23] J. Léopoldès, A. Dupuis, D. G. Bucknall, and J. M. Yeomans, "Jetting micron-scale droplets onto chemically heterogeneous surfaces," *Langmuir,* vol. 19, p. 9818, 2003.

[24] H. P. Jansen, K. Sotthewes, C. Ganser, C. Teichert, H. J. W. Zandvliet, and E. S. Kooij, "Tuning kinetics to control droplet shapes on chemically striped patterned surfaces," *Langmuir,* vol. 28, pp. 13137, 2012.

[25] W. Lee and G. Son, "Numerical study of droplet impact and filling in a microgroove," *Progress in Computational Fluid Dynamics,* vol. 11, p. 175, 2011.

[26] C. E. Hendriks, P. J. Smith, J. Perelaer, A. M. J. van den Berg, and U. S. Schubert, "'Invisible' silver tracks produced by combining hot-embossing and inkjet printing," *Advanced Functional Materials,* vol. 18, p. 1031, 2008.

[27] J. Bühler, F. P. Steiner, and H. Baltes, "Silicon dioxide sacrificial layer etching in surface micromachining," *Journal of Micromechanics and Microengineering,* vol. 7, p. R1, 1997.

[28] S. Gatz, H. Hannebauer, R. Hesse, F. Werner, A. Schmidt, T. Dullweber, J. Schmidt, K. Bothe, and R. Brendel, "19.4%-efficient large-area fully screen-printed silicon solar cells," *Physica Status Solidi (RRL) – Rapid Research Letters,* vol. 5, p. 147, 2011.

[29] M. Ngamo, L. Tous, E. Cornagliotti, J. Horzel, T. Janssens, R. Russell, J. Poortmans, and B. Lombardet, "Integration of high sheet resistance homogeneous emitters in a process flow for PERC-type solar cells with cu contacts," in *Proc*. *38th IEEE Photovoltaic Specialist Conference*, p. 003371 Austin, Texas, 2012.

[30] V. Linder, B. D. Gates, D. Ryan, B. A. Parviz, and G. M. Whitesides, "Water-soluble sacrificial layers for surface micromachining," *Small,* vol. 1, pp. 730, 2005.

[31] I. C. McNeill and S. M. T. Sadeghi, "Thermal stability and degradation mechanisms of poly(acrylic acid) and its salts: Part 1 - poly(acrylic acid)," *Polymer Degradation and Stability,* vol. 29, p. 233, 1990.

[32] L. Li and Y.-L. Hsieh, "Ultra-fine polyelectrolyte fibers from electrospinning of poly(acrylic acid)," *Polymer,* vol. 46, p. 5133, 2005.

[33] R. Y. Utama, "Inkjet printing for commercial high efficiency silicon solar cells," PhD thesis, University of New South Wales, Sydney, Australia, 2009.

[34] W. van Gelder and V. E. Hauser, "The etching of silicon nitride in phosphoric acid with silicon dioxide as a mask," *Journal of The Electrochemical Society,* vol. 114, p. 869, 1967.

[35] D. Soltman and V. Subramanian, "Inkjet-printed line morphologies and temperature control of the coffee ring effect," *Langmuir,* vol. 24, p. 2224, 2008.

[36] P. C. Duineveld, "The stability of ink-jet printed lines of liquid with zero receding contact angle on a homogeneous substrate," *Journal of Fluid Mechanics,* vol. 477, p. 175, 2003.

[37] J. Stringer and B. Derby, "Formation and stability of lines produced by inkjet printing," *Langmuir,* vol. 26, p. 10365, 2010.

[38] L. Liu, Z. Du, F. Lin, B. Hoex, and A. G. Aberle, "Aluminum local back surface field solar cells with inkjet-opened rear dielectric films," in *Proc. 38th IEEE Photovoltaic Specialists Conference*, p. 002204, Austin, Texas, 2012.

# Chapter 5. Aluminium local back surface field (Al-LBSF) solar cells with directly etched dielectric films

## §5.1 Introduction

The PV industry is continuously trying to reduce costs per Watt-peak by increasing the efficiency of increasingly thinner Si wafer solar cells. For this reason novel solar cell designs are required that e.g. have a higher level of surface passivation at both surfaces and exhibit lower reflection losses. The aluminium local back surface field (Al-LBSF) silicon wafer solar cell is one such cell design that is currently being intensively investigated for mass-scale manufacturing. In an Al-LBSF solar cell the full-area aluminium rear is replaced by a dielectric film covered with an Al film. The dielectric is locally opened to provide electrical contact between the Al rear electrode and the Si wafer. During the firing step the Al and the c-Si form an alloy, which then creates a local back surface field. The local dielectric openings are typically formed by a laser, either before printing of the Al film [1] or after deposition of the Al film (laser-fired contacts [2]). The laser process typically induces some damage to the underlying silicon [3], and hence potentially limits the theoretically possible PV efficiency gain. Direct printing technologies such as inkjet and aerosol jet have been introduced as alternative methods to pattern dielectric layers for solar cell fabrication.

The direct printing of HF containing etchants is usually not recommended as such etchants can have detrimental effects on both the inkjet and aerosol jet

printheads. Inkjet printheads are typically made of silicon, which oxidizes very quickly in air. As a result, a thin layer of native $SiO_2$ is formed on the surface of the printheads and the nozzles. The HF containing etchants easily remove the thin layer of native $SiO_2$ in the printheads and precipitate the $SiO_2$ at the nozzles. During the jetting process, the $SiO_2$ is not necessarily removed from the nozzles, resulting in the clogging of nozzles over time. In the worst case scenario, nozzle clogging can happen even before printing. In the case of aerosol jet printing, the nozzle tip is generally made of alumina ($Al_2O_3$). The printing of HF containing etchants can easily corrode the nozzle tip, which results in an enlargement of the printed feature size, or even a leakage of HF fumes. The production of HF aerosol through atomization is by itself a very dangerous process, let alone its leakage. Therefore other etching methods are being investigated.

The printing of acid resistant hot melt ink as mask for dielectric layer structuring was proposed by Fallisch *et al.* [4]. The phase changing requirement of the hot melt ink when heated to above 70 ˚C poses a significant constraint on the printhead design and strongly limits the accessible functionality of the ink. A reversible masking technique was developed by Lennon *et al.* [5], as mentioned in Chapter 2, to pattern the dielectric film. This approach not only involves many processing steps, it also requires some form of protection to the uncoated side. Therefore, in terms of device fabrication, the process is tedious and not easily controllable. Lennon *et al.* have also developed a maskless patterning technique [6, 7] (refer to Chapter 2). A schematic representation of the process using both inkjet printing and aerosol jet printing is shown in Fig. 5.1. In this work the mask-less patterning technique was investigated for the opening of the rear dielectric of Al-LBSF silicon wafer solar cells, using both the inkjet printing and the aerosol jet

printing technologies. The Al-LBSF solar cells produced with inkjet opened rear dielectric films have a homogeneous emitter structure, with screen printed Ag front and Al rear contacts. The Al-LBSF solar cells produced with aerosol jet opened rear dielectric films have a selective emitter structure, with evaporated aluminium as the rear contact and plated nickel (Ni) and copper (Cu) as the front contact.

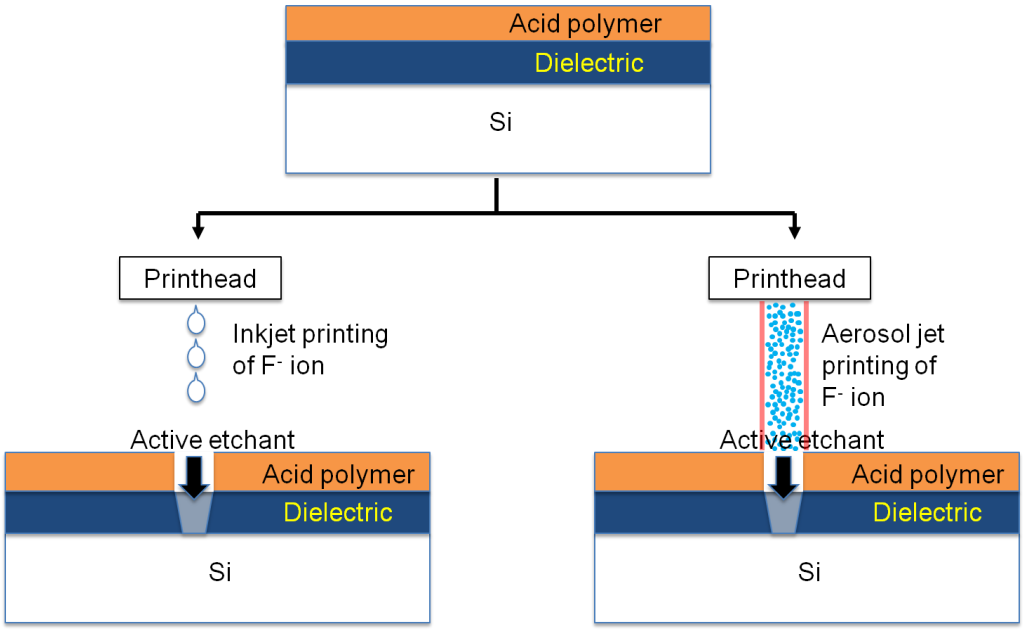


Fig. 5.1 Schematic representation of the maskless patterning techniques used in this work.

## §5.2 Experimental details

### §5.2.1 Inkjet printing

A batch of 21 (125 × 125 $mm^2$, pseudo-square) Al-LBSF silicon wafer solar cells was produced with inkjet opened dielectric layers, using the process flow of Fig. 5.2. The Cz *p*-type monocrystalline silicon wafers were first saw damage etched by the slow silicon etch (SSE) [8], followed by a single-side $SiN_x$ mask deposition by PECVD (SiNA XS, Roth & Rau). The exposed surface of the wafers was then textured in an alkaline solution. After a RCA and HF clean, the samples were diffused in a $POCl_3$ diffusion tube furnace resulting in a sheet resistance of 60 Ω/□. Subsequently, the phosphorus silicate glass (PSG) was removed by etching in diluted HF (5%) and the wafers received an RCA clean prior to coating the wafers with a $SiN_x$ (80 nm) film at the front side and a stack of $AlO_x$ (40 nm) and $SiN_x$ (100 nm) at the rear surface. Subsequently, the rear surface of six wafers was patterned by a picosecond laser ablation (SuperRapid, LUMERA) with a 1 mm line pitch, while the remaining 15 wafers were patterned with an inkjet printer (DMP3000, Fujifilm Dimatix) with a 1 and 2 mm line pitch. As mentioned earlier, the direct etching technique using an inkjet printer developed by Lennon *et al.* [6, 7] was used for the opening of the dielectric layer. First PAA was spin coated onto the wafers and left to dry. Subsequently, a solution containing ammonium fluoride ($NH_4F$) was printed onto the acid-coated rear surface of the wafer, locally forming HF that etches the rear dielectric layer. Residual etchants and deposits were then rinsed off in deionized water. The printing solution is prepared from 40% (w/v) ammonium fluoride (Sigma Aldrich) and polyethylene glycol (PEG) 400 (Sigma Aldrich). The resulting solution consisted of 11.2% (w/v) ammonium fluoride ($NH_4F$) and 20% (v/v) polyethylene glycol (PEG) 400.

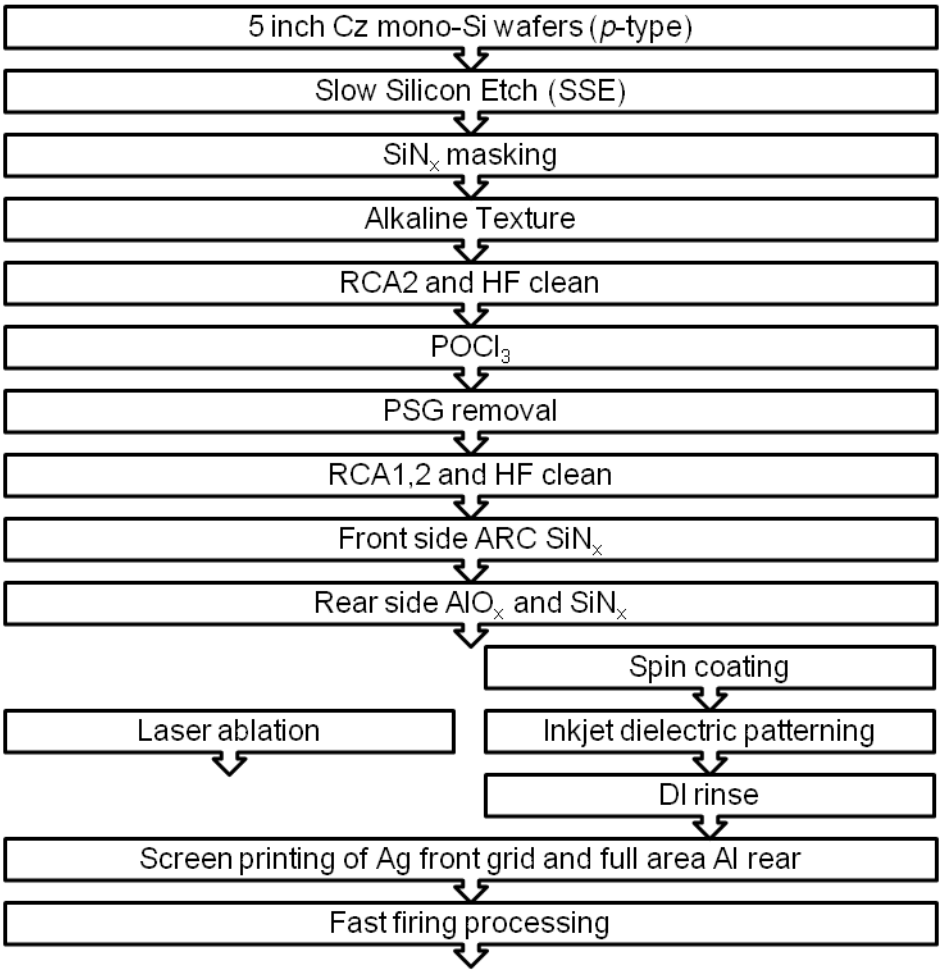


Fig. 5.2 Process flow for Al-LBSF solar cell fabrication with inkjet opened rear dielectric layer.

The wafers were printed using three different conditions: 10 layers of $NH_4F$ solution and 15 layers of $NH_4F$ solution at 1.0 mm pitch distance and 10 layers of $NH_4F$ solution at 1.5 mm pitch distance. For pitch distances of 1.0 and 1.5 mm, 125 and 83 line openings were created, respectively. It was ensured that the total processing time of the wafers was comparable to allow complete etching of the dielectric. The printed wafers were then rinsed in DI water, dried, and then screen printed with a Ag front metal grid and a full-area Al paste at the back, followed by a fast co-firing process (Ultraflex, Despatch Industries).

### §5.2.2 Aerosol jet printing

Another batch of small (40 × 40 $mm^2$) modified Al-LBSF solar cells with a selective emitter was fabricated. The wafers were partially processed by an industry partner with a homogenously diffused $POCl_3$ emitter (120 Ω/□), a $SiN_x$ (75 nm) antireflection coating at the front, and a stack of $AlO_x$ (10 nm) and $SiN_x$ (200 nm) at the rear. The subsequent processes and the resulting cell structure are schematically shown in Fig. 5.3.

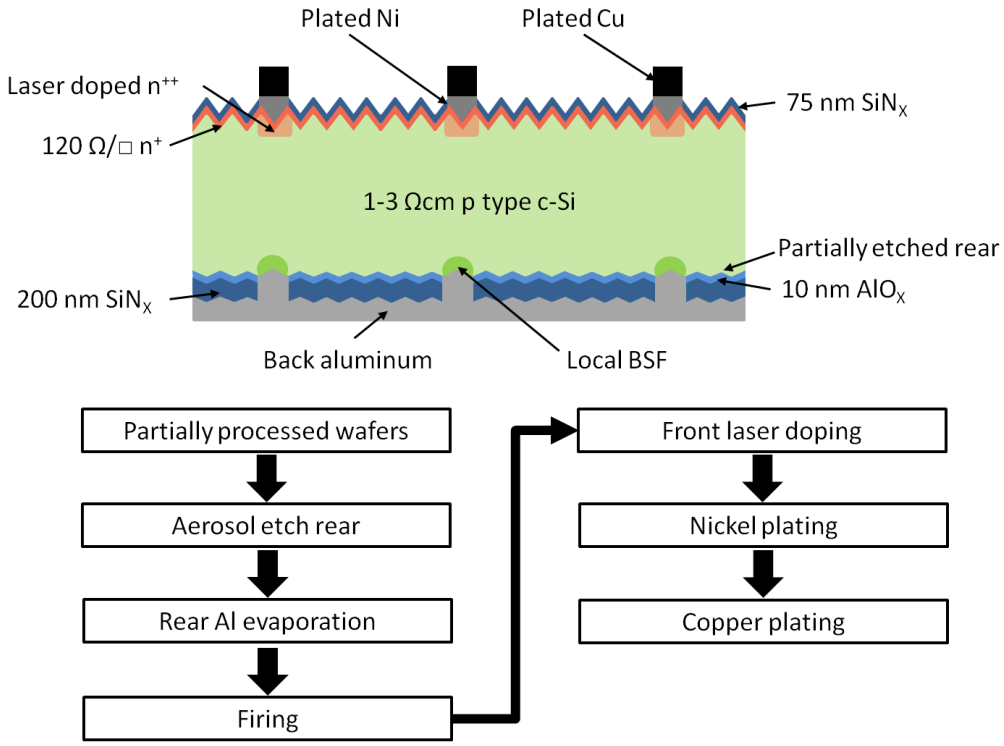


Fig. 5.3 Schematic representation of the process flow (bottom) and the resulting cell structure (top).

The rear dielectric was first spin coated with PAA, and subsequently patterned with an aerosol jet printer (Solar Lab System, Optomec) by depositing dilute $NH_4F$ solution (10 wt. %). The substrate was then rinsed in deionised water for

10 minutes to remove the residual etchant and deposits, and dried with a nitrogen gun. Next, Al was evaporated and fired for the formation of rear contact and localized BSF. Three different firing temperatures were used for the last two zones of the firing furnace, namely 750, 810 and 850 °C. The front side of the wafers was spin coated with phosphorus acid (85 wt%), prior to the formation of the selective emitter by laser doping [9]. The resulting sheet resistance of the laser doped area was ~15 Ω/□. Subsequently, plating of nickel and copper was performed to form the front contact.

## §5.3 Results and discussion

### §5.3.1 Inkjet preparation

It is important to first tailor the spin coating conditions to process large wafers (5 inch wide). The amount of PAA used for spin coating must be sufficient to uniformly cover the wafer. The spin coating condition comprises three steps, as shown in Table 5.1. The first step spins at low speed of 1000 rpm. PAA was added to the centre of the wafer during the first step until the wafer is fully covered with PAA. The second and third steps gradually smoothen the surface and reduce the thickness of the spin coated PAA by increasing the spin speed and the spin time.

Table 5.1 Spin coating conditions used for the PAA coating process.

| Step | Rpm | Time (s) |
|---|---|---|
| 1 | 1000 | 10 |
| 2 | 3000 | 10 |
| 3 | 5000 | 30 |

It is commonly known that fluoride ions and water are both essential to the etching of many dielectric materials [10, 11]. Since the HF solutions are not suitable for printing, the $NH_4F$ based solution is the best bet for direct patterning of dielectric layers. As discussed in Chapter 2, inks should have a viscosity of 10 - 12 cP and a surface tension of 28 - 32 dynes/cm in order to achieve optimal jetting. The solution obtained had a viscosity of only 4 cP and a surface tension of ~50 dynes/cm. Although the physiochemical properties lie outside of the optimal jetting range, stable jetting of the solution was achieved by Lennon *et al*.

from a single nozzle of a 1 pL printhead. However, with the use of multiple nozzles of a 10 pL printhead, the jetting process was observed to be very unstable. Several alterations such as increasing the pH by adding ammonium hydroxide (NaOH, 28 wt. %) [7] and degassing the prepared solution were thus performed, in order to stabilize the jetting condition. The jetting parameters were also tailored to ensure a smoother jetting process.

#### *§5.3.1.1 Waveform modification*

Modifications were performed to three main jetting parameters, namely the firing voltage, the meniscus vacuum and the jetting waveform. The firing voltage is an indication of the jetting force applied to a piezoelectric membrane to push the fluid out of the nozzle. As the surface tension of the prepared solution is higher than the optimal range, the inertia for the solution to emerge from the nozzles to form droplets is also higher. Thus the firing voltage was increased to increase the magnitude of the pressure wave.

The meniscus vacuum on the other hand determines the negative pressure inside the pumping chamber to prevent undesired leakage of the solution. Since the viscosity of the prepared solution was lower than the optimal range, the meniscus vacuum was also slightly increased to minimize leakage, but not to the extent of counterproductive effect of firing voltage increment.

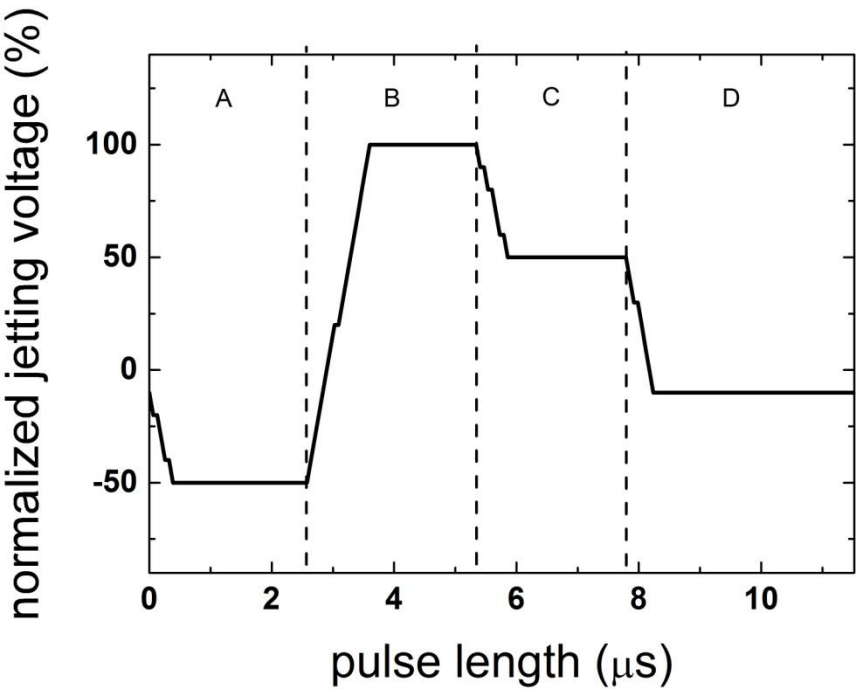


Fig. 5.4 Default jetting waveform used for a DMP cartridge.

Modification to the jetting waveform is the most crucial part in optimizing the jetting conditions, as it dictates how the jetting pressure is exerted. A typical jetting waveform for a Dimatix Material Printer (DMP) cartridge print head is shown in Fig. 5.4, which consists of 4 sections. A negative pulse in Section A bends the piezoelectric membrane backwards, drawing the ink from the reservoir into the ink cavity. This is followed by a positive pulse in Section B that bends the membrane forward to fully jet out the stored ink. In Sections C and D, a step wise recovery of the piezoelectric membrane to its original position is put in place to ensure no drastic change in the air pressure around the nozzle, which might affect the jetted droplet, or introduce undesired air bubbles into the nozzle.

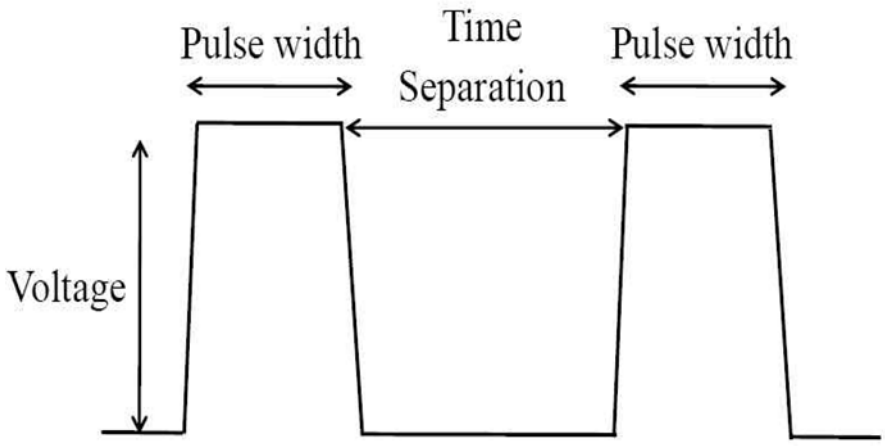


Fig. 5.5 Double waveform proposed for low viscosity fluids [12].

However, this waveform is tailored for inks with ideal viscosity and surface tension. The viscosity of the prepared solution prepared is way below the ideal range, which results in a weak damping force of the fluid during jetting. Furthermore the thickener, PEG 400, used in this solution is a long chain polymer. It tends to elongate during the jetting process and thus not break up into droplets. As a result, the jetted fluid is usually accompanied by a long satellite tail and it has a tendency to retract back into the nozzles and cause clogging to the nozzles. Thus a new waveform has to be designed in order to print the low viscosity solution. Shin and Sung proposed the use of double waveforms, as shown in Fig. 5.5, to drive their piezoelectric inkjet nozzle for the jetting of low viscosity liquid [12]. Although the idea of multiple driving pulses in one jetting waveform was investigated prior to this work [13-15], the focus was mostly on moderately viscous liquid.

The main issue with a low-viscosity fluid is that it usually has a weak damping force during the recovery phase of the piezoelectric membrane, which results in the leaking of the fluid and wetting of the nozzle area. A double waveform concept introduces a second pressure wave, which acts as an additional damping mechanism by reducing the liquid momentum during the recovery phase of the jetting process. Moreover, the second pressure pulse also introduces an additional push to enhance the break-up mechanism for the jetting of long-chain polymers.

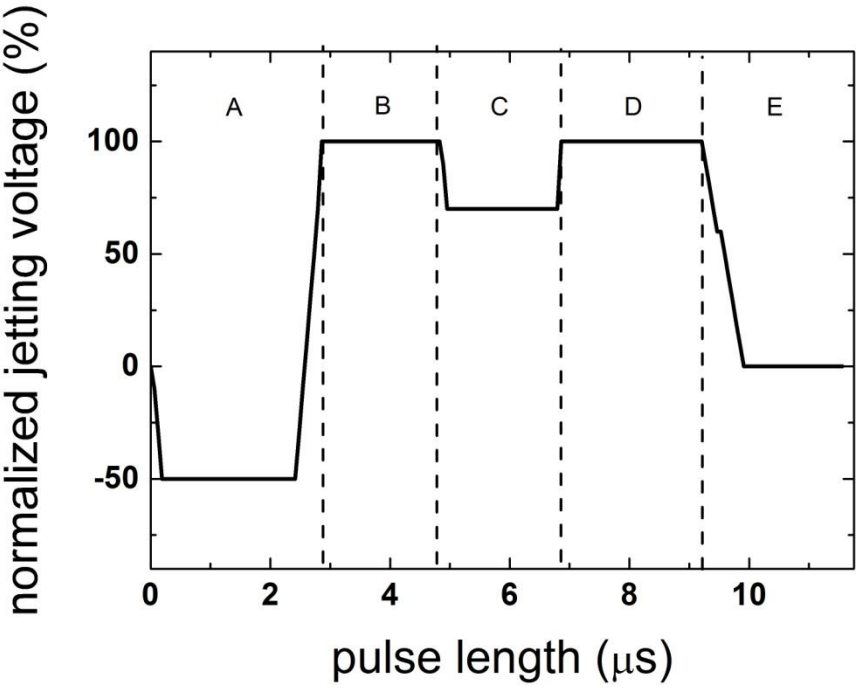


Fig. 5.6 The alteration made to the driving waveform that produces a jetting process that was stable for hours.

To implement this concept into the DMP default cartridge waveform, an additional peak was introduced after the first recovery step in Section C of Fig. 5.4. The second pressure peak was not added after the full recovery step in

Section D so as to prevent undesired filling of the ink cavity before the second pressure wave was applied.

Fig. 5.6 and Fig. 5.8 show two waveform alterations to the default cartridge waveform. The first alteration produced a jetting process that was stable for hours, as shown in Fig. 5.7. It was observed that the primary droplets were accompanied by long satellite tails, which seemed to be rectified by reducing the amplitude of the jetting voltage.

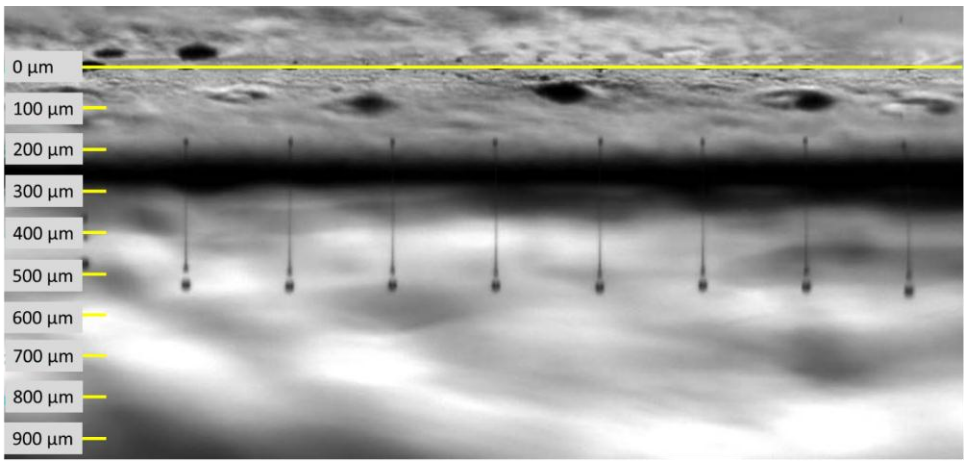


Fig. 5.7 Photograph of the nozzle plate and the jetted droplets taken by the high-speed camera of the DropWatcher of the DMP printer, showing a stable jetting process produced by the waveform alteration as shown in Fig. 5.6.

At full voltage, the first pulse exerts a force that causes the solution to exit the nozzle at a high velocity, which usually leads to tail break-up. The long-chain polymer in the solution however tends to resist the separation and elongates into a long tail. The second pulse then further reinforces the tail breakup process. As a result, the droplet formed comprises a fast moving leading drop and an elongated satellite tail. When the voltage is decreased, the exit velocity of the leading drop will decrease. This reduces the room for the tail to elongate and

provides more time for the remaining droplet to catch up with the leading drop. Although the reduction in jetting pressure seemed to produce single droplets without satellite tails, the jetting became unstable over time as the low voltage only partially emptied the ink cavity. The solution left in the cavity was believed to have affected the subsequent jetting process and eventually resulted in clogging.

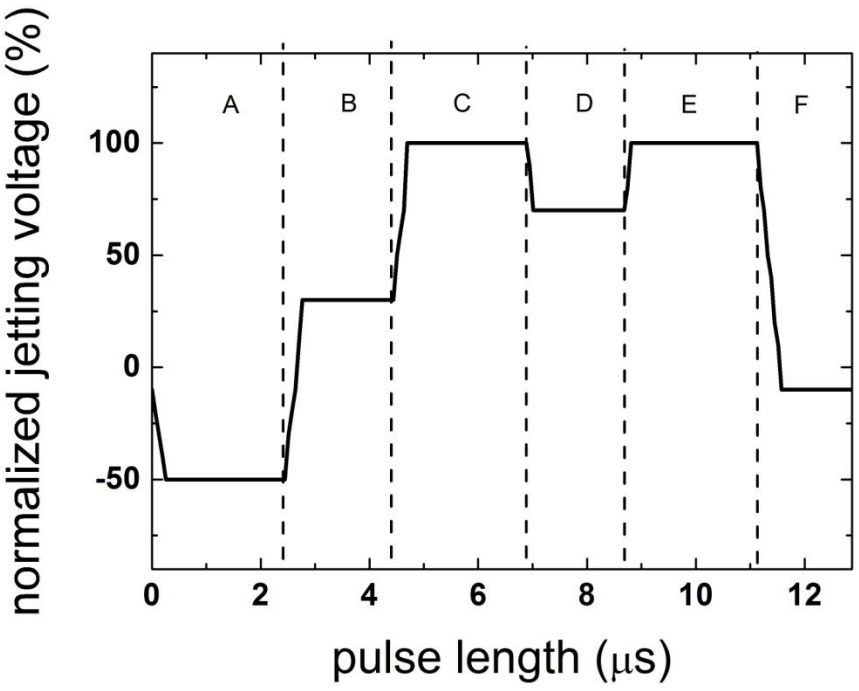


Fig. 5.8 The alteration made to the driving waveform that produces well defined droplets.

To overcome the jetting instability, a step-wise increase of pressure pulse was implemented to the piezoelectric membrane during jetting, as shown in Fig. 5.8. The first part of the positive pulse pushes the fluid out of the nozzle at a lower velocity, and the second part of the pulse fully empties the ink cavity. The jetting process using this waveform is shown in Fig. 5.9. The pulse duration for this waveform was ~12.9 μs. Thus it can be seen from Fig. 5.9 that tail breakup

occurs between 10 and 20 µs. As the second part of the positive wave empties the ink cavity, a more substantial amount of solution is jetted out of the nozzle at the end of the tail. The high surface tension of the solution causes the elongated tail to break up, resulting in the formation of a primary leading droplet and a secondary droplet between 20 and 30 µs. However, as the exit velocity of the leading droplet is not very high, the secondary droplet quickly catches up and merges with the primary droplet at ~40 µs. Single droplets were formed ~50 *µs* into the jetting process, as shown in Fig. 5.9. However as prolonged jetting is more stable using the first alteration, the waveform as shown in Fig. 5.7 is used for device fabrication.

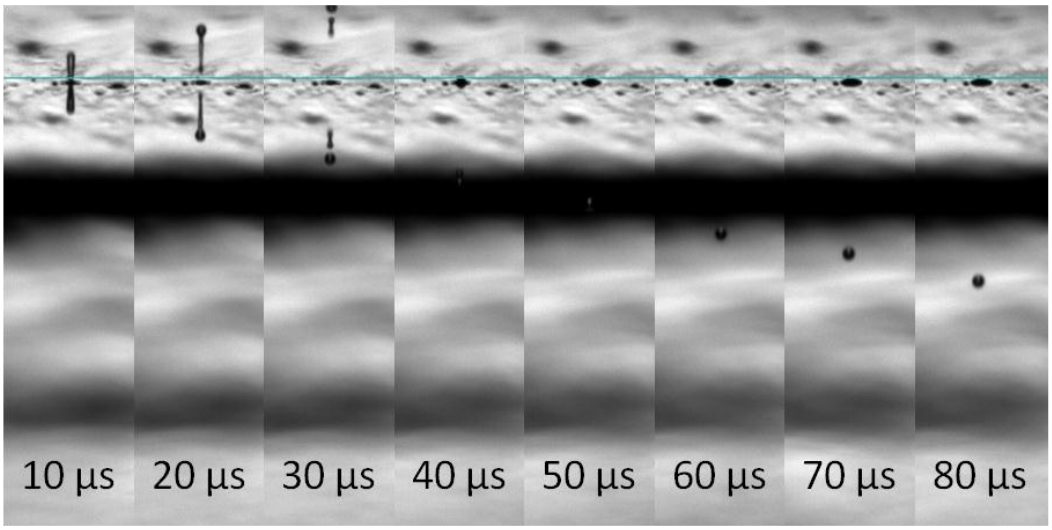


Fig. 5.9 Photographs of a nozzle and the positions of the jetted droplet at various time intervals produced by the waveform alteration as shown in Fig. 5.8, taken by the high-speed camera of the DropWatcher of the DMP printer, illustrating the drop formation process.

### §5.3.2 Al-LBSF with inkjet patterned dielectric layer

A summary of the average results obtained for the 21 solar cells is provided in Table 5.2. It can be seen that the open-circuit voltage ($V_{oc}$) values obtained by

the solar cells with inkjet printed dielectric openings were not significantly different from those with laser ablated dielectric openings. Theoretically one would expect a higher $V_{oc}$ for the solar cells with the inkjet opened rear dielectric due to the absence of laser induced damages. However, it can be seen from Table 5.2 that, except for cells printed with 10 layers of $NH_4F$ solution at 1.5 mm pitch distance, the average $V_{oc}$ values for the other two printing conditions were actually lower than that obtained for the solar cells with laser opened rear contacts. This is mainly due to the reduced metallization fraction for these solar cells.

Table 5.2 Average of five one-Sun *I-V* results for the Al-LBSF solar cells produced in this study. The uncertainty given represents the standard deviation of the measurement.

| **Pitch (mm)** | **Method of opening** | $V_{OC}$ **(mV)** | $J_{SC}$ **(mA/cm$^2$)** | ***FF*** **(%)** | ***Eff*** **(%)** |
|---|---|---|---|---|---|
| **1.0** | Inkjet 10 layers | 627.1 ± 4.1 | 37.4 ± 0.4 | 74.1 ± 2.9 | 17.4 ± 0.5 |
| | Inkjet 15 layers | 627.4 ± 1.0 | 37.2 ± 0.1 | 75.8 ± 0.6 | 17.7 ± 0.2 |
| | ps laser | 628.7 ± 1.7 | 37.6 ± 0.1 | 72.1 ± 1.6 | 17.1 ± 0.4 |
| **1.5** | Inkjet 10 layers | 631.4 ± 1.6 | 37.6 ± 0.1 | 75.0 ± 0.8 | 17.8 ± 0.2 |

For laser ablated line openings, the line width is well controlled at 100 µm, resulting in a dielectric coverage of about 90% for rear side passivation. Whereas for inkjet opened dielectric with a 1.0 mm pitch distance, the chemical etching of

the dielectric layer was not controlled sufficiently to produce a consistent line width. The line width ranges from 150 µm to 200 µm, resulting in an 80% to 85% dielectric coverage only, which results in a significant reduction to the degree of rear side passivation. On the other hand, for inkjet opened dielectrics with a 1.5 mm pitch distance, the dielectric coverage was found to be in the 86-90% range. This is comparable to the laser ablated lines, resulting in a better passivation quality compared to the solar cells with a 1.0 mm pitch distance.

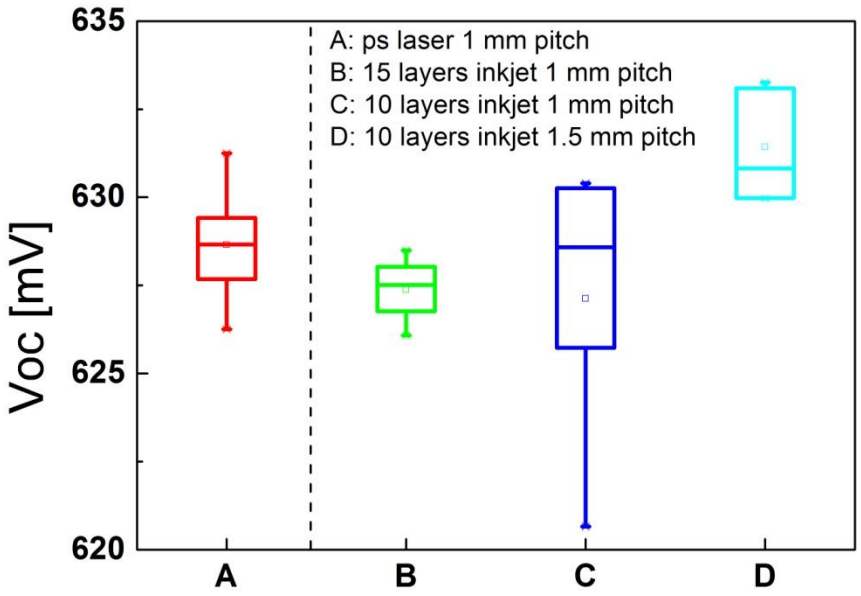


Fig. 5.10 Box plots of the one-Sun $V_{oc}$ of the solar cells with inkjet and laser opened dielectric films.

Fig. 5.10 shows the statistical distribution of the $V_{oc}$ of the 21 cells. It can be seen that Group C has the largest spread of data compared to the rest of the inkjet printed groups, because not all the line openings were fully etched by 10 layers of $NH_4F$ printed solution. The data spread in Group B is the smallest, as these samples were printed with 15 layers of $NH_4F$. Although the cells in Group D were

also printed with 10 layers of $NH_4F$ solution, the additional etching time allowed the dielectric layer to be fully opened.

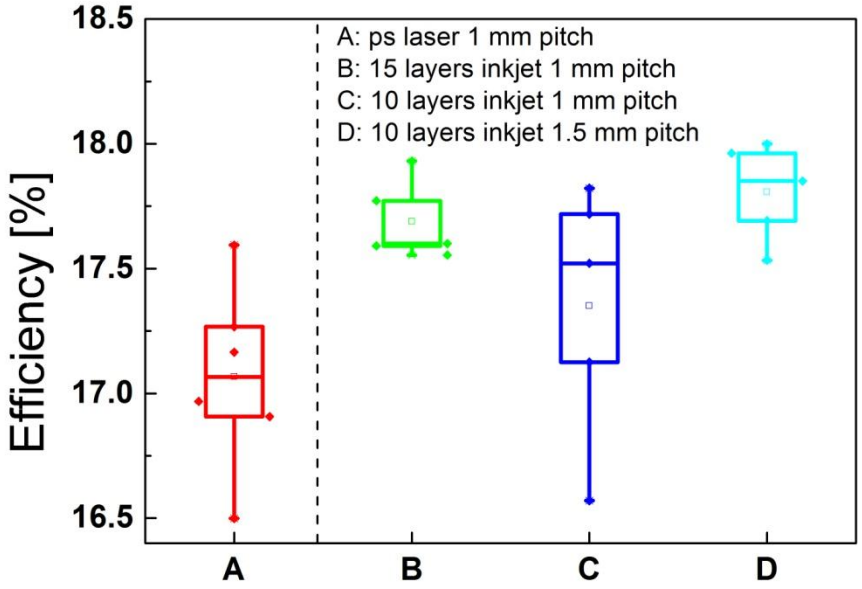


Fig. 5.11 Box plots of the one-Sun efficiency of the solar cells with inkjet and laser opened dielectric films.

Fig. 5.11 shows the statistical distribution of the one-Sun solar cell efficiencies. Although the average $V_{oc}$ of the laser ablated cells was higher than that of the inkjet printed cells at 1.0 mm pitch distance, the average efficiency was lower. It can be seen from Table 5.2 that this is due to a lower average fill factor in the laser ablated cells, which resulted from a higher series resistance. As mentioned previously, the line width of the laser ablated openings were maintained consistently at 100 µm, whereas the inkjet printed openings ranged from 150 µm to 200 µm. For smaller line widths, there is a higher chance of Kirkendall void [16] formation during the fast firing process between the screen-printed aluminium and the underlying silicon. This results in an increase in contact resistance, which in turn increases the overall series resistance. However a smaller line width also

implies in a larger dielectric coverage, which is beneficial for the overall $V_{oc}$ of the solar cell. A larger dielectric coverage can typically be achieved by either increasing the pitch distance or decreasing the line width. Cui *et al.* reported a decreasing BSF thickness with increasing pitch distance, due to the spread limit of c-Si in Al [17]. At smaller pitch distance, the spread limit of Si in Al overlaps one another, thereby saturating the Al layer above the dielectric opening [18]. With increasing pitch distance that surpasses the spread limit, the saturation of Al above the dielectric opening decreases, resulting in a decreasing BSF thickness. This effect is more pronounced with thin layer of Al. Urrejola *et al.* also observed that the spread limit does not depend on the opening width [19]. Therefore the reduction in line width is preferred in order to achieve a thick BSF for good contact formation while maintaining a large dielectric coverage for a good passivation effect. Furthermore the firing profile has to be tuned to minimize the resistive losses due to smaller line width.

### §5.3.3 Al-LBSF with aerosol jet opened dielectric layer

The line width of an inkjet patterned dielectric film is limited by the physio-chemical properties of the ink and its jetting stability. As the printed solution has a low viscosity, a high number of printing passes typically results in large feature sizes of > 150 µm. In addition, inkjet printing of $NH_4F$ solution mixed with PEG400 thickener still demonstrates relatively poor jetting stability. By patterning the dielectric layer with aerosol jet printing, the line width can be reduced due to the beam collimation feature. In addition, the aerosol formation from the $NH_4F$ solution is also very stable. Therefore the dielectric layers were reliably patterned at a line width of ~70 µm. The Al used for the rear contact was evaporated, rather

than screen printed, for its relative ease in the formation of thicker BSF. The effect of peak firing temperature on contact formation was investigated, while the dielectric coverage was maintained at > 90%. Three peak firing temperatures, namely 750, 810 and 850 °C, were employed for the last two firing zones. The fill factors of the cells and their corresponding pseudo fill factors are plotted against the peak firing temperatures in Fig. 5.12.

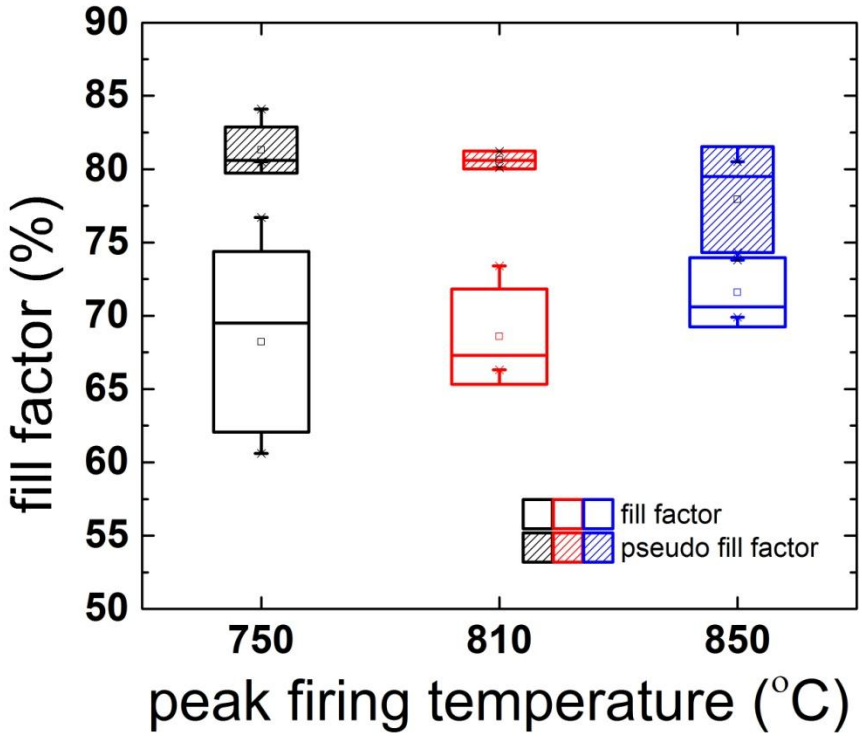


Fig. 5.12 Boxplot of the *FF* (clear boxes) and the pseudo fill factors (shaded boxes) of the cells fired at a peak firing temperature of 750 °C, 810 °C and 850 °C. The box plot represents the standard deviation of 3-5 cells.

At the lowest peak firing temperature of 750 °C the variation in the *FF* was found to be relatively large, whereas the variation of the pseudo fill factor (*pFF*) was found to be smaller. This suggests that series resistance plays a significant role in the overall *FF* loss, as the *pFF* represents the (almost) series resistance free

*FF*. The contact formation is inconsistent and varies significantly from cell to cell. As the peak firing temperature increases, the standard deviation of the fill factor decreases, indicating an improvement in consistency in the contact formation. At the highest peak firing temperature of 850 °C, the standard deviation of the *FF* does not deviate much from that of the *pFF*, indicating a more consistent contribution of series resistance to the overall fill factor loss. This can be understood by a better BSF formation with increasing peak firing temperature, as also observed by Cui *et alia* [17].

The series resistance of the Al-LBSF solar cells was calculated by comparing the one-Sun *I-V* curve to the dark *I-V* curve [20]. The results are shown in Fig. 5.13. Overall, the series resistance decreases with increasing peak firing temperature. The variation in series resistance from cell to cell at the same peak firing temperature also decreases with increasing peak firing temperature, indicating a more consistent contact formation process. The trend shown in the series resistance plot is in good agreement with that in the fill factor plot. The inconsistency in contact formation is also evidently demonstrated in the Al-LBSF solar cells with the highest and lowest series resistances, which were both fired at a peak temperature of 750 °C.

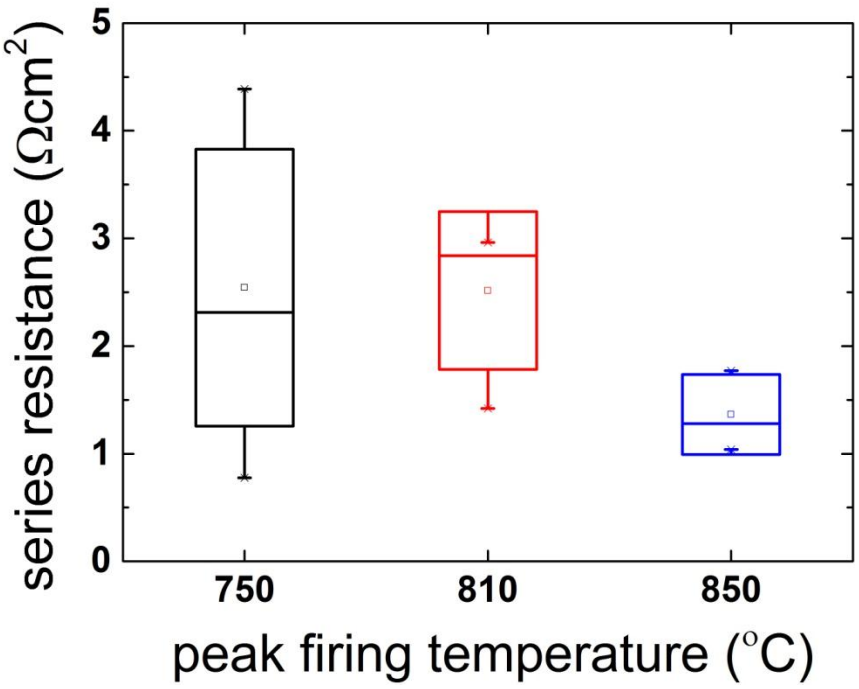


Fig. 5.13 Boxplot of calculated series resistance of the Al-LBSF solar cells at the peak firing temperatures of 750 °C, 810 °C and 850 °C. The box plot represents the standard deviation of 3-5 cells.

A comparison of the plot of local ideality factor versus the voltage extracted from the dark *I-V* measurement, or the *m-V* curve, between the two solar cells is shown in Fig. 5.14. The *m-V* curves of the two solar cells are generally identical in the dark voltage range of < 500 mV, showing a slight hump at ~100 mV. Typically the humps in the *m-V* curves are caused by a change in recombination due to the activation of a certain type of defects, or a change in the dominating recombination mechanism [21, 22]. This suggests a consistent passivation of the recombination processes in both solar cells fired at the peak temperature of 750 °C. However a significant difference in the *m-V* curves that results in the observed disparity in the fill factors of the two solar cells occurs at voltages

above 500 mV. This portion of the *m-V* curve is typically affected by the series resistance of the solar cell.

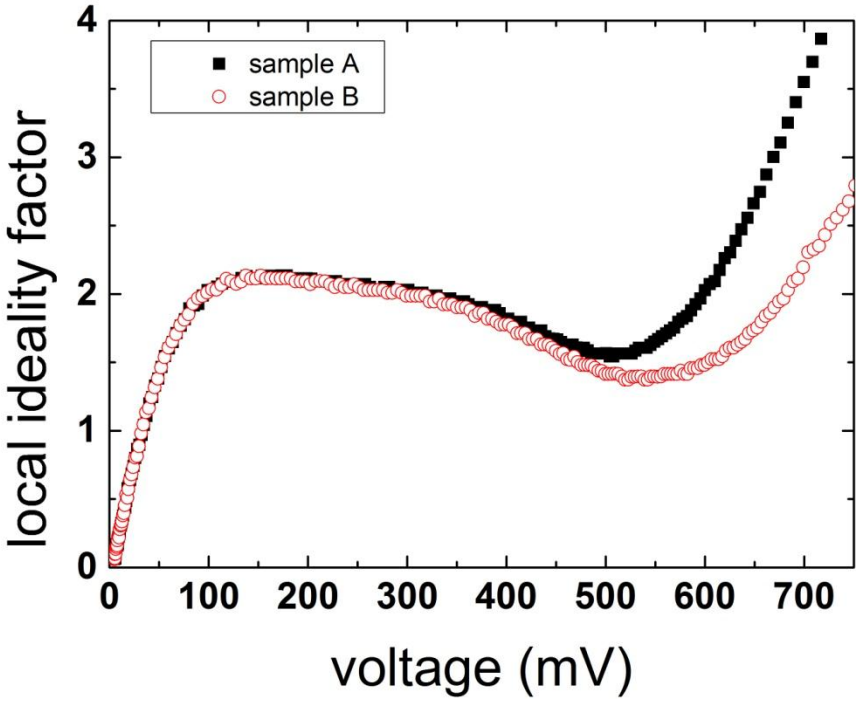


Fig. 5.14 Local ideality factor as a function of the voltage for two Al-LBSF solar cells, as extracted from their dark *I-V* measurements. Sample A (black filled squares) and sample B (red open circles) are the Al-LBSF solar cells with the lowest and highest measured *FF*, respectively, among all the samples fired at 750 °C.

As shown in Fig. 5.14, the *m-V* curve for the Al-LBSF solar cell with the lowest *FF* shows a much earlier and steeper increase in the local ideality factor for voltages > 500 mV as compared to the solar cell with the highest *FF*. This indicates a significant difference in the series resistance of the two solar cells, resulting from the inconsistency in contact formation when fired at a peak temperature of 750 °C.

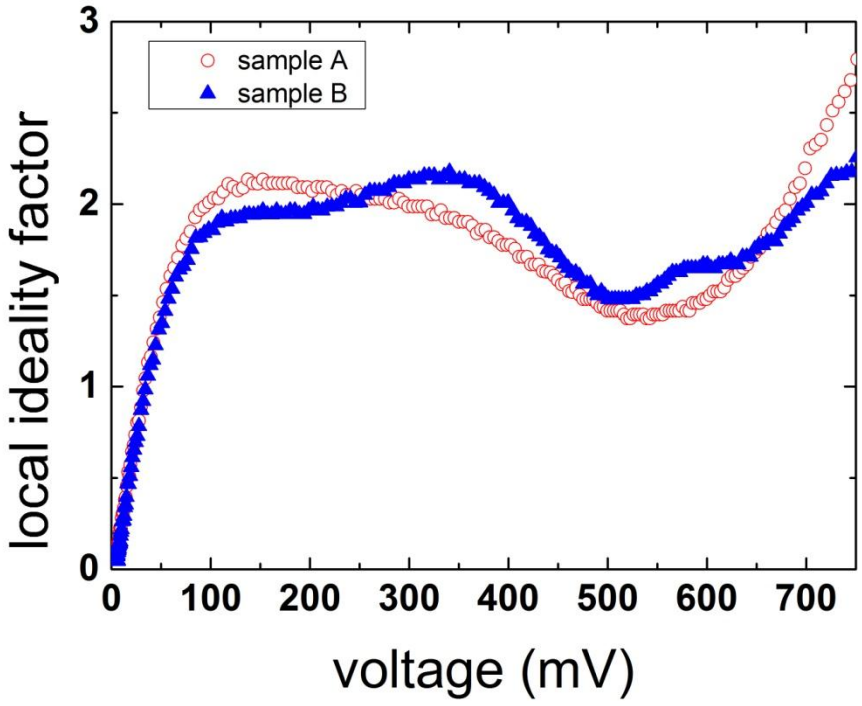


Fig. 5.15 Local ideality factor as a function of the voltage for two Al-LBSF solar cells, as extracted from their dark *I*-V measurements. Sample A (red open circles) and sample B (blue filled triangles) are the Al-LBSF solar cells with the highest measured *FF* among all the samples fired at 750 °C and 850 °C, respectively.

The comparison of the *m*-*V* curve of the Al-LBSF solar cell with the highest *FF* fired at 750 °C with that fired at 850 °C is shown in Fig. 5.15. The hump in the *m*-*V* curve of the two solar cells at low voltages of < 500 mV occurs at different dark voltages. One reason could be that different defects are activated at different firing temperatures, and a difference of 100 °C in the peak firing temperature might be able to activate different defects that influence recombination processes at different injection levels or voltages. For voltages above 500 mV, the local ideality factor of the solar cell fired at 850 °C demonstrates a more gentle increase as compared to the solar cell fired at 750 °C. Thus a higher peak firing temperature should be employed for better contact and BSF formation in order to reduce the series resistance and improve the fill factor. However a high peak

firing temperature typically has an adverse effect on the passivating dielectric stack underneath the Al. Aluminium oxide ($AlO_x$) used for the passivation of *p*-type c-Si typically requires a thick $SiN_x$ layer for firing protection. The problem with $SiN_x$ is that it is porous in nature, and thus Al can easily spike through the rear passivation layer if the peak firing temperature is set too high. This can cause severe degradation to the overall passivation and the performance of the solar cells. For instance, the Al-LBSF solar cell produced in this batch with the lowest $V_{oc}$ of 604 mV was also fired at the peak firing temperature of 850 °C. A scanning electron microscope (SEM) image of a non-contact region that suffers from the spiking of Al at the rear side of the solar cell and its corresponding energy-dispersive X-ray spectroscopy (EDS) image are shown in Fig. 5.16.

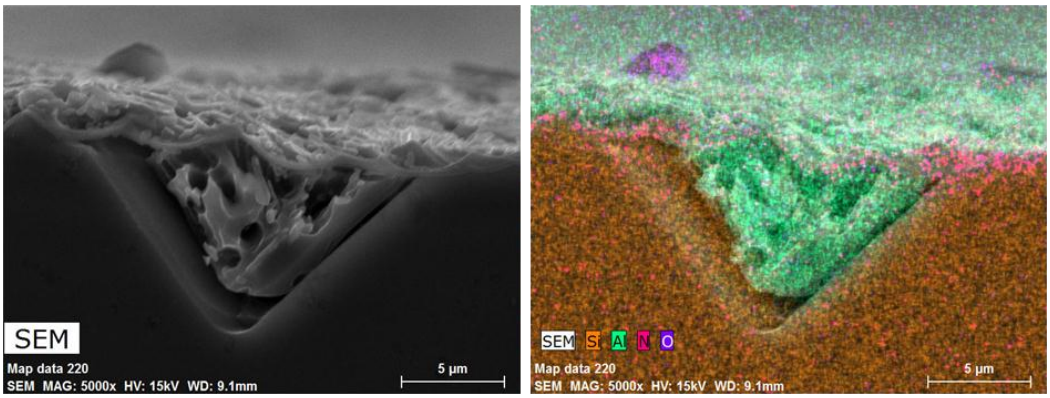


Fig. 5.16 SEM (left) and EDS (right) micrograph of Al spiking into c-Si at a non-contact area. The orange, green, pink and purple regions in the EDS micrograph correspond to c-Si, Al, N and O, respectively.

Normally, if there is no Al spiking during firing, three discrete stacked layers of c-Si, N and Al should be observed in the EDS micrograph. The N component is a representation of the $SiN_x$ capping layer. However it can be observed from the centre portion of Fig. 5.16 that a significant amount of Al is detected in the Si region and traces of N can still be observed in the Al layer. This indicates that the

aluminium has spiked through the $SiN_x$ capping layer into the c-Si. The EDS image shows that the nitrogen (N) component, which probably originates from the $SiN_x$ layer, was severely disrupted by the spiking of Al. The rear passivation layer will be significantly compromised when the occurrence of Al spiking increases with increasing peak firing temperature. Therefore a trade-off is required when choosing the peak firing temperature to obtain a good contact and BSF formation, while minimizing damages to the passivation layer and preventing shunting of the solar cells. The champion cell produced in this batch with an efficiency of 18.5% was fired at a peak temperature of 810 °C. The one-Sun *I-V* cell parameters are shown in Table 5.3.

Table 5.3 One-Sun solar cell parameters of the champion solar cell.

| $V_{oc}$ (mV) | $J_{sc}$ (mA/cm$^2$) | FF (%) | $R_s$ (Ωcm$^2$) | $\eta$ (%) |
|---|---|---|---|---|
| 643.7 | 39.2 | 73.4 | 1.42 | 18.5 |

Although the starting material for the fabrication of Al-LBSF solar cells with inkjet and aerosol jet opened dielectric layers were different, the increment in PV efficiency was expected be higher than the current 0.5%, especially with a selective-emitter structure implemented at the front of the solar cells for those with aerosol jet opened dielectric layers. The fill factor was relatively low (< 75%) for the entire batch of solar cells. The series resistance of the champion cell was found to be ~1.42 Ωcm$^2$, which considerably lowers the *FF* and thus the efficiency of the solar cell. In order to visualise the BSF thickness, selective etching of the rear contacts was performed, whereby the etching rate of highly doped c-Si is faster. By taking the SEM images of the rear contacts thereafter,

the BSF thickness can be represented by the out-of-focus regions underneath the contact areas, as shown in Fig. 5.17. An observable phenomenon is that the thickness of the evaporated Al above the dielectric openings varies from contact to contact. Although the immediate thickness of Al after evaporation was ~2 µm, the thin layer of Al might have redistributed during the firing process as the temperature exceeded the Al melting temperature. As a consequence, some opening areas were covered with a thicker Al film, some with a thinner Al film, and others with an accumulation of Al on one side and a depletion on the other, as shown in Fig. 5.17 (a), (b) and (c), respectively.

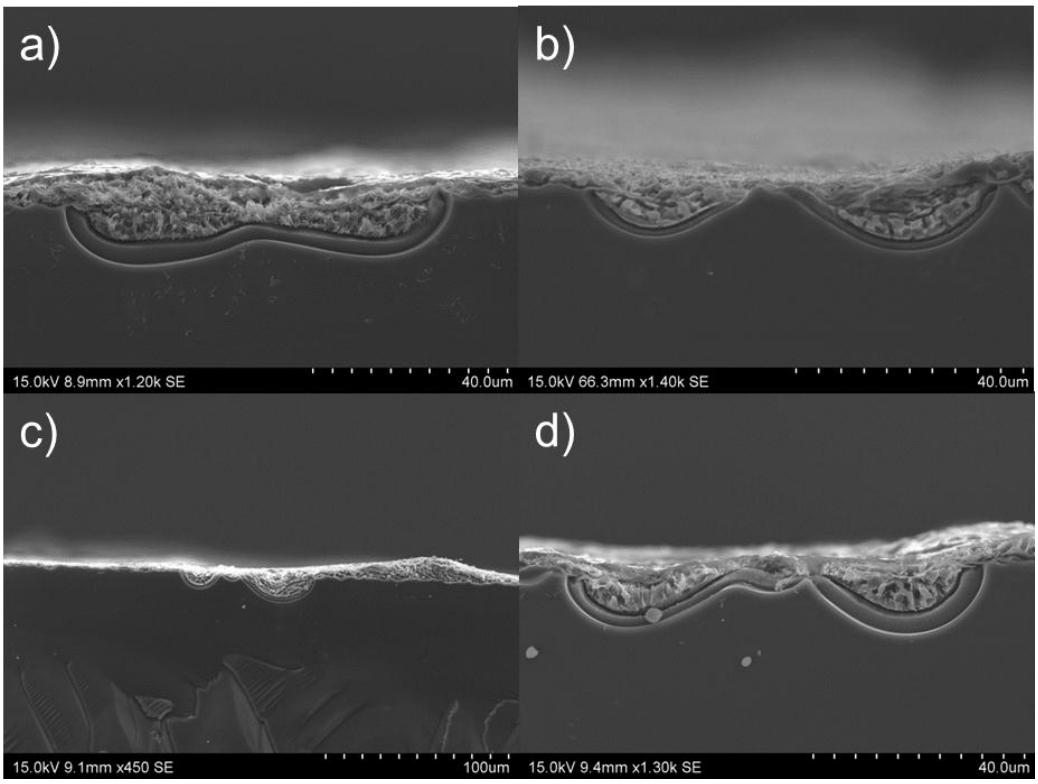


Fig. 5.17 SEM micrographs of rear contact areas having a) a thick BSF due to a thick layer of Al, b) a thin BSF due to a thin layer of Al, c) an accumulation of Al to one side and a depletion to the other and d) a thicker BSF on the side of Al accumulation and a thinner BSF on the side of Al depletion.

The BSF thickness also changes correspondingly, as it is greatly affected by the amount of Al available for contact and BSF formation. A relatively thick and uniform BSF is shown in Fig. 5.17(a) as it is covered under a thick layer of Al. On the contrary, a much thinner BSF can be seen in Fig. 5.17(b). In the case of Al accumulation on one side of the contact and depletion on the other, it is also demonstrated in Fig. 5.17(d) that a thicker BSF is formed on the side of Al accumulation and a thinner BSF on that of Al depletion. Furthermore, evaporated aluminium - in comparison to screen printed Al - also has a higher tendency to spike through the dielectric layer and shunt the solar cell as its Al purity is much higher than its screen printed counterpart. As a result, the spiking of Al similar to that shown in Fig. 5.16 has also been observed in a few places on the rear of the champion solar cell. Such non-uniformity in the formation of BSF might have had a significant impact on the fill factor losses. Theoretically, the solar cell performance can be further enhanced by improving both the bulk and surface passivation, reducing the feature size of the opened dielectric layer, and increasing the fill factor. The most apparent approach at hand is to mitigate the uniformity in the BSF thickness by having a thicker Al layer at the rear, and improve the fill factor by fine-tuning both the laser doping and plating processes.

## §5.4 Conclusion

This Chapter looked into an application of direct printing for the opening of dielectric films. Inkjet printing and aerosol jet printing were employed to selectively open the rear dielectric film by applying a direct etching method in the fabrication of Al-LBSF solar cells. As the physiochemical properties of the fluoride containing solution lay outside of the optimal jetting range, the preparation and jetting condition of the inkjet solution was optimized. Modifications were also performed in detail to the jetting waveform. It was found that by using a two-peak waveform, stable jetting can be achieved that lasts for hours. A dwelling section was introduced in the positive driving waveform to facilitate the formation of well-defined droplets.

The stable jetting condition was applied to the fabrication of solar cells. A batch of Al-LBSF solar cells with rear dielectric layer locally opened with either an inkjet printer or a ps laser was produced. Three printing conditions were used to investigate their effects on the solar cell efficiency, and a preliminary comparison between inkjet printed and laser ablated dielectric openings was done. The first result showed champion solar cell efficiencies of 18.0% and 17.6% that were obtained in this work for Al-LBSF solar cells with inkjet and laser opened contacts, respectively.

In order to increase the dielectric coverage to > 90%, aerosol jet printing was employed to reduce the line width of the opened dielectric layer. Evaporation of Al was used for the formation of a thicker BSF. The effects of the peak firing temperature on the formation of rear contacts and the BSF were also investigated. It was observed that a higher peak firing temperature typically results in a thicker BSF layer. However, the downside of using a higher temperature was that

the passivation layer is more likely to be damaged due to the tendency of Al spiking. Therefore the champion cell with a conversion efficiency of 18.5% was fired at a trade-off peak temperature of 810 °C. The issue of low fill factor for the entire batch of solar cells produced was also investigated. The fill factor losses were found to be significantly influenced by the non-uniformity in the BSF thickness, which could be a result of a possible redistribution of the thin evaporated Al during the high-temperature firing process.

## §5.5 References Chapter 5

[1] J. Muller, K. Bothe, S. Gatz, H. Plagwitz, G. Schubert, and R. Brendel, "Contact formation and recombination at screen-printed local aluminium-alloyed silicon solar cell base contacts," *Electron Devices, IEEE Transactions on,* vol. 58, p. 3239, 2011.

[2] E. Schneiderlöchner, R. Preu, R. Lüdemann, and S. W. Glunz, "Laser-fired rear contacts for crystalline silicon solar cells," *Progress in Photovoltaics: Research and Applications,* vol. 10, p. 29, 2002.

[3] M. Abbott, P. Cousins, F. Chen, and J. Cotter, "Laser-induced defects in crystalline silicon solar cells," in *Proc*. *31st IEEE Photovoltaic Specialists Conference (PVSC)*, p. 1241, 2005.

[4] A. Fallisch, D. Stuwe, R. Neubauer, D. Wagenmann, R. Keding, J. Nekarda, R. Preu, and D. Biro, "Inkjet structured EWT silicon solar cells with evaporated aluminium metallization and laser-fired contacts," in *Proc*. *35th IEEE Photovoltaic Specialists Conference (PVSC)*, p. 003125, 2010.

[5] A. J. Lennon, R. Y. Utama, M. A. T. Lenio, A. W. Y. Ho-Baillie, N. B. Kuepper, and S. R. Wenham, "Forming openings to semiconductor layers of silicon solar cells by inkjet printing," *Solar Energy Materials and Solar Cells,* vol. 92, p. 1410, 2008.

[6] A. Lennon, A. W. Y. Ho-Baillie, and S. Wenham, "Maskless patterned etching of silicon dioxide by inkjet printing," in *Proc*. *Optoelectronic and Microelectronic Materials and Devices, 2008. COMMAD 2008. Conference on*, p. 170, 2008.

[7] A. J. Lennon, A. W. Y. Ho-Baillie, and S. R. Wenham, "Direct patterned etching of silicon dioxide and silicon nitride dielectric layers by inkjet printing," *Solar Energy Materials and Solar Cells,* vol. 93, pp. 1865, 2009.

[8] F. K. Basu, M. B. Boreland, D. Sarangi, and V. Shanmugam, "Non-acidic isotropic etch-back for silicon wafer solar cells", USA Provisional Patent application, 2013.

[9] S. R. Wenham and M. A. Green, "Self aligning method for forming a selective emitter and metallization in a solar cell", US Patent US6429037 B1, 2002.

[10] K. R. Williams, K. Gupta, and M. Wasilik, "Etch rates for micromachining processing-part ii," *Journal of Microelectromechanical Systems,* vol. 12, p. 761, 2003.

[11] K. R. Williams and R. S. Muller, "Etch rates for micromachining processing," *Journal of Microelectromechanical Systems* vol. 5, p. 256, 1996.

[12] S. Pyungho and S. Jaeyong, "The effect of driving waveforms on droplet formation in a piezoelectric inkjet nozzle," in *Proc*. *11th Electronics Packaging Technology Conference,* p. 158, 2009.

[13] S. Sakai, "Dynamics of piezoelectric inkjet printing systems," presented at the International Conference on Digital Printing Technologies, pp. 15, Vancouver, B.C., Canada, 2000.

[14] A. U. Chen and O. A. Basaran, "A new method for significantly reducing drop radius without reducing nozzle radius in drop-on-demand drop production," *Physics of Fluids,* vol. 14, p. L1, 2002.

[15] H. Dong, W. W. Carr, and J. F. Morris, "An experimental study of drop-on-demand drop formation," *Physics of Fluids,* vol. 18, p. 072102, 2006.

[16] E. O. Kirkendall and A. D. Smigelskas, "Zinc diffusion in alpha brass," Transaction of the American Institute of Mining, Metallurgical, and Petroleum Engineers*,* vol. 171, p. 130, 1947.

[17] J. Cui, J. Colwell, Z. Li, and A. Lennon, "Localised back surface field formation via different dielectric patterning approaches," in *Solar 2012 Conference, Melbourne, Australia, 2012*.

[18] C. Jia, Z. H. J. Tey, D. Zhe Ren, L. Fen, B. Hoex, and A. G. Aberle, "Investigation of screen-printed rear contacts for aluminium local back surface field silicon wafer solar cells," *Photovoltaics, IEEE Journal of,* vol. 3, p. 690, 2013.

[19] E. Urrejola, K. Peter, H. Plagwitz, and G. Schubert, "Silicon diffusion in aluminium for rear passivated solar cells," *Applied Physics Letters,* vol. 98, p. 153508, 2011.

[20] A. G. Aberle, S. R. Wenham, and M. A. Green, "A new method for accurate measurements of the lumped series resistance of solar cells," in *Proc*. *23rd IEEE Photovoltaic Specialists Conference (PVSC)*, p. 133, Louisville, USA, 1993.

[21] Z. Hameiri, K. McIntosh, and G. Xu, "Evaluation of recombination processes using the local ideality factor of carrier lifetime measurements," *Solar Energy Materials and Solar Cells,* vol. 117, p. 251, 2013.

[22] K. R. McIntosh, "*Lumps, humps and bumps: Three detrimental effects in the current-voltage curve of silicon solar cells"*: PhD thesis, University of New South Wales, Sydney, 2001.

# Chapter 6. Summary and outlook

## §6.1 Summary

The work presented in this thesis can be divided into three aspects and, collectively, they describe the problems investigated and resolved during the application of drop-based direct writing technologies in the fabrication of aluminium local back surface field (Al-LBSF) silicon wafer solar cells.

The first aspect investigated was the unexpectedly fast etching of highly doped *n*-type silicon in hydrofluoric acid (HF), which was observed during a critical mask-removal process prior to the direct writing application. As HF is known in the silicon community for its excellent selectivity in etching dielectric films over silicon, it is commonly used to remove masking layers in the fabrication process of advanced silicon wafer solar cells. However, it was found experimentally in this thesis that this selectivity does not necessarily exist in the case of highly doped *n*-type silicon. Consequently the etching of highly doped *n*-type silicon significantly affected the efficiency of the fabricated solar cells. A detailed investigation of the etching of phosphorus-doped silicon in HF was carried out, and showed an unexpectedly high etch rate of ~0.8 nm/min for Si with a surface [P] of $> 1.3\times10^{20}$ $cm^{-3}$. The etch rate rapidly decreased to ~ 0.02 nm/min as the surface [P] reduced to $< 1.3\times10^{20}$ $cm^{-3}$. Hydroxide-mediated hydrolysis of silicon and the carrier concentration dependent effects of heavily doped layers were identified as the most likely underlying mechanisms causing this fast etching behaviour. The proper understanding of the etching behaviour facilitated better control over the steps prior to the direct writing applications in the fabrication of Al-LBSF solar

cells. In addition, the unique etching behaviour can also potentially be used for other industrial applications.

The second aspect of this thesis proposed a solution to a common challenge encountered in the drop-based direct writing technologies, which is to achieve high definitions for directly deposited features on rough hydrophilic surfaces. This challenge is particularly evident for inkjet printing. In this PhD thesis, inkjet and aerosol jet printing technologies were used to pattern the rear dielectric of Al-LBSF solar cells. Typically a silicon surface coated with a dielectric film is very hydrophilic. A spreading diameter of about 5 mm was observed for a 10 pL inkjet droplet when it impacted onto a textured silicon surface coated with a 200 nm thick $SiN_x$ film. A new method was developed to geometrically confine the inkjet printed features on rough hydrophilic surfaces. This method involved spin coating of a sacrificial layer of polyacrylic acid (PAA), followed by patterning of the dielectric layer through the PAA at temperatures above 180 °C. To facilitate physical confinement, it was found that the spin-on sacrificial layer must have a thickness greater than the height of the deposited droplet. Not only does a thick spin-on sacrificial layer enhance wetting, it also modifies the topography of the surface. Using a 4 µm thick spin-on PAA, 200 nm of $SiN_x$ was successfully selectively etched at ~200 °C by inkjet printing of phosphoric acid ($H_3PO_4$). The resulting line width after repeated printing was measured to be ~75 µm and ~30 µm, respectively, with a 10 pL and 1 pL printhead. An *in-situ* heating device was fabricated that further improved the line definition to ~15 µm.

Finally, after having tackled the fundamental issues mentioned above, the problems faced with the actual application of inkjet and aerosol jet printing to selectively open the rear dielectric films of Al-LBSF silicon wafer solar cells were

discussed. Firstly the problem of incompatible physiochemical properties of the fluoride containing inkjet solution with the optimal jetting requirement was addressed. Stable jetting was achieved by implementing a two-peak waveform, with which a batch of Al-LBSF solar cells with inkjet opened dielectric films was produced. A preliminary comparison between inkjet printed and laser ablated dielectric openings was performed, giving champion solar cell efficiencies of 18.0% and 17.6%, respectively, for Al-LBSF solar cells with inkjet and laser opened contacts. In order to increase the dielectric coverage to > 90%, aerosol jet printing was employed to reduce the line width of the opened dielectric layer. The peak firing temperature was also varied to achieve a good compromise between contact formation and rear surface passivation, giving a champion solar cell efficiency of 18.5% for a peak firing temperature of 810 °C.

## §6.2 Outlook

As the work described in this thesis is new, there are ample opportunities for further development. The remainder of this Chapter will provide a brief outlook of the work performed in this thesis.

For a start, since the significant etching of highly doped *n*-type silicon was observed in **Chapter 3**, more work can be done to find out if the etching behaviour also applies to heavily doped *p*-type silicon. However, as the diffusion mechanism of boron in silicon is very different from that of phosphorus in silicon, the resulting doping profile corresponding to a similar sheet resistance value is very different. Therefore the identical analysis method for phosphorus-doped silicon cannot directly be applied to boron-doped silicon. Although the vacancy induced hole creation is absent in boron-doped silicon, a preliminary study showed that an estimate of 28 nm of boron-doped silicon was removed after immersion in 40 °C HF for 50 minutes. The difference in size between boron and silicon atoms is greater than that between phosphorus and silicon atoms. As a consequence, the stress induced in the boron-doped silicon lattice is higher than that in the phosphorus-doped silicon lattice. This might have resulted in the etching of heavily doped *p*-type silicon in HF. Further work is required to investigate this phenomenon in detail.

In addition, the etching behaviour of the heavily doped silicon in HF can be exploited for device fabrication, as mentioned in **Chapter 3**. An invention disclosure has been submitted to NUS that aims to achieve, in a single step, the simultaneous formation of lightly doped emitter at one side of the double-side diffused wafer and total p-n junction removal at the other. This can be done by

immersing the double-side diffused silicon wafers into HF and illuminating one side with UV light. Further experiments are required to realise the idea.

In **Chapter 4**, the geometric confinement of directly deposited features was experimentally demonstrated by selectively etching through 200 nm of $SiN_x$ while maintaining high line definition. However, the method is not limited to subtractive inkjet printing applications. It can also be coupled with additive inkjet printing or aerosol jet printing for other applications. In addition, the chemistry of the sacrificial layer can also be modified to achieve the desired wetting condition and topography. This method of physical confinement can also be used in the fabrication sequence for other advanced solar cells.

The main application of direct writing explored in **Chapter 5** is the selective opening of dielectric films. There are also other potential applications, such as the directing printing of resists and masks, seed layer metallization, and full-height metallization. A unique feature of direct writing is its digital prototyping capability, which enables the immediate physical realization of any digitally designed pattern. This makes direct writing a cheaper, more flexible and less time consuming alternative to photolithography in the formation of resists and masks. The development in achieving nano-sized metal particles also facilitates the production of several metal inks, which are compatible with both the inkjet and the aerosol jet printing technologies. The direct printing of seed layers with such metal inks can be employed prior to the metal plating process to form metal contacts with high aspect ratios. It is also possible to produce full-height metallization with direct printing. However, many technical and fundamental issues have to be tackled before achieving directly printed full-height metallization. One such technical barrier when directly depositing metal inks is

the spreading effect of the ink droplets upon impact on the substrate surface. Using a pneumatic atomizer of an aerosol jet printer, a metal ink with a higher viscosity and concentration of metal nano-particles can be printed in conjunction with a heated substrate holder, to minimise the spreading effect and increase the aspect ratio. However, for inkjet printing the printable metal inks normally have much lower viscosities and concentrations of metal nano-particles. Hence, the spreading effect is more evident and problematic. This can potentially be solved by adding phase changing properties to the metal inks and integrating the corresponding features such as UV illumination and hot-melt compatible print heads to the inkjet printer. Although the addition of such features enables near-instant solidification of the printed droplets, it also brings up a more fundamental limitation of the technology: ink formulation. To achieve full-height metallization, besides satisfying the basic physiochemical properties as mentioned in **Chapter 2**, it is preferable for the metal inks to have high conductivity (i.e., a high concentration of metal nano-particles) and good adhesion (i.e., the presence of bonding agents such as glass frits). If phase changing properties were to be added to the metal inks, it would definitely pose a great challenge for the ink formulation. A considerable amount of research and development is certainly required to tackle this fundamental limitation.

Hence, there is still a lot of room for further research and improvement for direct writing technology and its applications in solar cell fabrication.

# List of publications arising from this thesis

### Journals

**L. Liu**, F. Lin, M. Heinrich, A G. Aberle, B. Hoex, “Unexpectedly high etching rate of highly doped n-type crystalline silicon in hydrofluoric acid”, ECS Journal of Solid State Science and Technology, Vol 2, Issue 9, pp. 380-383, 2013.

**L. Liu**, X. Wang, A. Lennon, B. Hoex, “Geometric confinement of directly deposited features on hydrophilic rough surfaces using a sacrificial layer”, Journal of Materials Science, Vol 49, Issue 12, pp. 4364-4370, 2014.

### Conferences

**L. Liu**, Z. Du, F. Lin, B. Hoex, A.G. Aberle, “Aluminum local back surface field solar cells with inkjet-opened rear dielectric films”, Proc. 38th IEEE Photovoltaic Specialists Conference (PVSC), 002204-002207, 2012.